



*Simulation of stringer stiffened CFRP
panels in consideration of
skin-stringer separation*

Andrea Winzen

Referent: Prof. Dr.- Ing Jörn Harder, Aachen University of Applied Sciences
Korreferent: Dr.- Ing. Richard Degenhardt, German Aerospace Center (DLR)

March 2006

Aachen University of Applied Sciences
Department of Aerospace Technology
Hohenstrafenallee 6
52064 Aachen
Germany

In cooperation with:

German Aerospace Center
Deutsches Zentrum für Luft- und Raumfahrt e.V. (DLR)
Institute of Composite Structures and Adaptive Systems
Lilienthalplatz 7
38108 Braunschweig
Germany

Author: Andrea Winzen

Date of delivery: 30.03.2006

1. Auditor: Prof. Dr.-Ing. Jörn Harder
2. Auditor and industrial supervisor: Dr.-Ing. Richard Degenhardt

Abstract

The first main focus of this work was to improve and investigate the sensitivity to various parameters of previously developed user subroutines for the finite element (FE) tool ABAQUS/Standard (ABAQUS). These subroutines are aimed at the realistic simulation of degradation of an adhesive layer between a skin and stringer in a composite panel. In this work, simple stress based failure criteria were implemented to predict failure.

The influence of numerous parameters on the numerical stability, the accuracy and the time consumption of the nonlinear FE analysis was tested for several versions of different subroutines. These parameters included changes in geometry of the model and the number and location of elements and changes in the subroutine code itself. Different stress based failure criteria were applied and investigated. Also the code for the subroutine USDFLD was improved and extended in order to give a more realistic prediction of element failure in the adhesive layer. Analyses were performed for the Design 1 panel (D1) of the COCOMAT project [5]. The results were compared across a range of aspects including accuracy, time consumption, failure stress and usability.

The other main focus of this work was the investigation of numerous possible influences on the buckling behavior of the D1 panel. Numerical simulation were performed including different geometric imperfections to evaluate the influence of these imperfections on the axial stiffness, the load-carrying capacity, the buckling mode shapes and the collapse point of the panel. These results were compared to the data previously collected during the experimental testing of a panel similar to the COCOMAT panels. The different influences were described and discussed and recommendations were made for the setup, performance and validation of the COCOMAT panels, which will be tested at the DLR in the spring of 2006.

Table of contents

1. Introduction.....	1
1.1 The intention of this work.....	1
1.2 The COCOMAT project.....	1
1.3 The objectives of this work.....	3
1.4 The structure of this work.....	4
2. Literature Review.....	6
2.1 Fiber-reinforced materials.....	6
2.1.1 Stresses and deformation in fiber-reinforced materials.....	6
2.1.2 Simplified stresses and deformations in UD layers.....	9
2.1.3 Derivation of Classical Laminate Theory.....	11
2.2 Adhesive joints.....	17
2.2.1 General overview.....	17
2.2.2 Bonding mechanisms of adhesive joints.....	18
2.2.3 Failure modes of adhesive joints.....	20
2.2.4 Failure criteria of adhesive joints.....	21
2.3 Finite element method.....	23
2.3.1 Introduction and general overview of FEM.....	23
2.3.2 Principal of minimum potential energy.....	24
2.3.3 The displacement method.....	25
2.3.4 Usage and application of FEM.....	27
2.3.4 The Newton-Raphson method.....	29
3. User Subroutines-Simulation of skin-stringer debonding.....	33
3.1 General overview.....	33
3.2 The user subroutine USDFLD.....	34
3.2.1 Data flow of the USDFLD.....	34
3.2.2 Definition of the material properties and FVs.....	35
3.3 The user subroutine UMAT explicit.....	36
3.3.1 Data flow of the UMAT explicit.....	36
3.3.2 Definition of the material properties and SDVs.....	37
3.3.3 Calculation of the stiffness and stresses.....	38
3.4 The user subroutine UMAT implicit.....	38
3.4.1 Data flow of the UMAT implicit.....	38
3.4.2 Problems of numerical stability and their solutions.....	39
3.5 Comparison of the subroutines.....	40
4. Description of the simulation model.....	42
4.1 Description of the panel geometry.....	42
4.2 Introduction of materials as basis for the simulation model.....	45
4.3 Modeling of the panel.....	45
4.4 Numerical results without degradation.....	47
5. Parametric Studies.....	49
5.1 Influence of parameters within the UMAT implicit.....	49
5.1.1 PNEWDT factor.....	49
5.1.2 Stress ratio control.....	52
5.2 Variation of the geometry of the simulation model.....	53
5.2.1 Variation of the thickness of the adhesive layer.....	55

5.2.2	Variation of the number of adhesive elements in the thickness direction.....	57
5.2.3	Variation of the number of adhesive elements in the axial direction.....	59
5.3	Development and application of the USDFLD Tension & Compression.	60
5.3.1	Explanation of the subroutine code of the USDFLD Tension & Compression.....	61
5.3.2	Comparison of the different versions of the USDFLD.....	65
5.3.3	Comparison of different failure criteria in the USDFLD Tension Compression.....	70
5.4	Development and application of the USDFLD Principal Stresses.	71
5.5	Summary of the parametric studies.....	75
6.	Experiment.....	78
6.1	Description of the experiment.....	79
6.2	Measurement technique.....	81
6.3	Description of the experimental results.....	83
6.4	Comparison of experiment and numerical predictions without degradation.....	85
6.5	Conclusions.....	86
7.	Numerical simulations and evaluation of additional aspects.....	88
7.1	Results of eigenvalue buckling analysis introduced as geometrical imperfections.....	88
7.2	Variation of the stringer thickness.....	91
7.3	Results of asymmetrical load introduction introduced as geometrical imperfections.....	94
7.4	Curved lateral edge.....	99
7.5	Evaluation of the strain gages data.....	102
7.6	Comparison of different versions of the USDFLD.....	105
7.7	Summary of the numerical simulations and evaluation of additional aspects.....	107
8.	Summary and Conclusions.....	109
9.	References.....	112
Appendix A: Subroutine codes.....		114
Appendix B: Input files.....		138
Declaration (Erklärung).....		144

Index of figures

Figure 1-1	Main objective of COCOMAT project.....	3
Figure 2-1	Local coordinate system of single fiber layer.....	6
Figure 2-2	Stress state in a volume element.....	7
Figure 2-3	Local coordinate system of a single fiber layer	11
Figure 2-4	Local and global coordinate system of a single UD layer.....	14
Figure 2-5	Definition of lever arms of single layers in coordinate system.....	15
Figure 2-6	Orientation of internal forces and moments.....	15
Figure 2-7	Loading forms of adhesive joints.....	17
Figure 2-8	Adhesion and cohesion demonstrated at a drop of liquid on an inclined plane.....	18
Figure 2-9	Typical single lap joint	18
Figure 2-10	Stress distribution in adhesive joints.....	19
Figure 2-11	Parameters of a single lap joint used in the method of Volkersen....	19
Figure 2-12	Nonlinear load-displacement curve.....	29
Figure 2-13	First iteration in an increment of ABAQUS.....	30
Figure 2-14	Second iteration in an increment of ABAQUS.....	31
Figure 3-1	Data flow of the USDFLD.....	34
Figure 3-2	Declaration of the material properties in the input file.....	35
Figure 3-3	Data flow of the UMAT explicit.....	36
Figure 3-4	Declaration of the material properties in the input file.....	37
Figure 3-5	Declaration of material properties and SDVs.....	38
Figure 3-6	Data flow of the UMAT implicit.....	39
Figure 4-1	Geometry of the panel V15.....	42
Figure 4-2	Panel with applied boundary conditions.....	42
Figure 4-3	Panel geometry and fiber orientation.....	43
Figure 4-4	Definition of the coordinate system.....	43
Figure 4-5	Model of the stringer used on the V15 panel.....	44
Figure 4-6	FE model of the skin-stringer connection.....	46
Figure 4-7	Mesh of the D1 model.....	46
Figure 4-8	Load-shortening graph of panel V15 with different mesh densities ...	47
Figure 4-9	Load-shortening graph of shells without stringers.....	48
Figure 4-10	Load-shortening graph of the D1 panel without degradation.....	48
Figure 5-1	Load-shortening curve with different PNEWDT factors.....	50
Figure 5-2	Load-shortening curves with different stress ratios.....	52
Figure 5-3	Build up of the stringer model.....	54
Figure 5-4	Load-shortening curves of the D1 panel with and without modeling mistakes.....	55
Figure 5-5	Load-shortening curves for different thicknesses of the adhesive.....	56
Figure 5-6	Different build ups of the adhesive layers.....	57
Figure 5-7	Load-shortening curves for different number of adhesive elements in the thickness direction	58
Figure 5-8	Load-shortening graph of different numbers of adhesive elements in the axial direction.....	59
Figure 5-9	Comparison of different failure stresses.....	61
Figure 5-10	Comparison of different versions of the USDFLD for SMAX=8.3MPa.....	65
Figure 5-11	Comparison of different versions of the USDFLD.....	67
Figure 5-12	Final buckling shapes of the three version of the USDFLD.....	68
Figure 5-13	Failure prediction for the last increment for the original USDFLD...	68

Figure 5-14	Failure prediction for the last increment for USDFLD Tension & Compression.....	69
Figure 5-15	Comparison of different failure criteria for the USDFLD Tension & Compression.....	70
Figure 5-16	Example: Stresses in different coordinate systems for a plane stress state.....	72
Figure 5-17	Illustration of principal stresses in 3D stress state.....	73
Figure 5-18	Load-shortening graph of all different versions of USDFLD.....	74
Figure 6-1	Phases of modeling and simulation.....	78
Figure 6-2	Basic size of the tested panel P23	79
Figure 6-3	Panel in the buckling facility.....	80
Figure 6-4	Undeformed reference state.....	82
Figure 6-5	Final deformation state.....	82
Figure 6-6	Experimental deformation patterns at various values of axial compression [mm], view facing the stringer side.....	83
Figure 6-7	Load-shortening curve of the experimental testing of panel P23.....	84
Figure 6-8	Comparison of experimental and simulation data.....	85
Figure 6-9	Experimental and numerical deformation patterns at different values of axial compression [mm], viewed facing the stringer side... ..	86
Figure 7-1	Buckling mode shapes of the original calculation and the first eigenmode.....	89
Figure 7-2	Load-shortening curve of the P23 panel with and without skin imperfections.....	90
Figure 7-3	Panel geometry and stringer numbering.....	91
Figure 7-4	Load-shortening curves of models with different stringer widths.....	92
Figure 7-5	Buckling modes of the three modified panels and the experiment....	93
Figure 7-6	Panel with two concentrated loads introduced on nodes on the lateral edges.....	95
Figure 7-7	Displacement in the 1-direction under asymmetric loading of lateral edges.....	95
Figure 7-8	Buckling shapes of the second increment with introduced imperfection.....	97
Figure 7-9	Load-shortening graph of different imperfection scale factors.....	97
Figure 7-10	Buckling shapes of nominal panel, panels with different scaling factors and experiment.....	98
Figure 7-11	Panel with imperfection on left lateral edge.....	99
Figure 7-12	Load-shortening graph with imperfection introduced on lateral edge.....	100
Figure 7-13	Buckling shapes of the nominal panel, the modified panel and the tested panel.....	101
Figure 7-14	View of the strain gages from the skin side.....	102
Figure 7-15	Strain gage and simulated strain data of H0 to H3.....	103
Figure 7-16	Strain gage and simulated strain data for H22 to H25.....	104
Figure 7-17	Load-shortening graph of different versions of the USDFLD in comparison to experimental results.....	105
Figure 7-18	Final buckling shapes of different versions of USDFLD and experiment.....	106

Index of tables

Table 1-1	Universities participating in COCOMAT.....	1
Table 1-2	Research establishments participating in COCOMAT.....	2
Table 1-3	Aircraft companies participating in COCOMAT.....	2
Table 4-1	Geometric data of the COCOMAT panel.....	44
Table 4-2	Material of the adhesive layer-Redux 312.....	45
Table 4-3	Material of the plates: Prepreg IM7/8552 (Carbon/Epoxy).....	45
Table 5-1	Time consumption for the analysis of the D1 panel for different PNEWDT factors.....	51
Table 5-2	Time consumption for the analysis of the D1 panel for different stress ratios.....	53
Table 5-3	Variation of the beam length.....	54
Table 5-4	Computation time for different number of elements in the axial direction.....	60
Table 5-5	Time consumption of USDFLD Tension & Compression for different failure criteria.....	71
Table 5-6	Comparison of different versions of USDFLD.....	75
Table 6-1	Technical data of the Aramis system.....	81
Table 7-1	Position of the strain gages	103

Index of symbols

A	Surface
B	Flexural or bending stiffness matrix
c	Adhesive length (Section 2.2)
c	Damping factor (Section 2.3.5)
c_a	Displacement correction
D	Elasticity matrix (Section 2.3.3)
D	Extensional or membrane stiffness matrix (Section 2.1)
E	Young's modulus
F	Force
F_v	Viscous forces
G	Shear modulus
h	Hour
I_a	Structural inertial force
K	Coupling stiffness matrix
K_0	Tangential stiffness
l	Length
M^*	Artificial mass matrix
m	Vector of moment resultants
min	Minute
N	Matrix of shape functions
n	Vector of force resultants
P	Load, external force
Q	Displacement vector (Section 2.2.3)
Q	Elastic constant for orthotropic material
R_a	Residual force
S	Stress
s	Second
t	Thickness (Section 2.1)
t	Time (Section 2.3.5)
U	Vector of displacement
u, v, w	Local coordinates
u, v, w	Displacements (Section 2.1.1)
v	Vector of nodal velocity
x, y, z	Global coordinates
W	Work
z	Distance between midplane of a layer and parent of coordinate system (Section 2.1.3)

Greek letters

α	Ply angle
β	Correction factor
ε	Strain
κ	Bending
ν	Poisson's ratio
\mathbf{v}	Vector of nodal velocity
ρ	Density
σ	Normal stress
τ	Shear stress
φ	Portion of the fiber
Δ	Increment
Π	Strain energy
Φ	Vector of nodal displacements

Acronyms and abbreviations

BL	Buckling load
CLT	Classical laminate theory
CFRP	Carbon fiber reinforced polymer
COCOMAT	Improved M ATerial Exploitation at Safe Design of C OMposite Airframe Structures by Accurate Simulation of C OLLapse
Damage	Larger value of current stress and maximum stress up to the increment as the possible damage value
DF	Damping factor
DLR	Deutsches Zentrum für Luft-und Raumfahrt
DOF	Degree of freedom
D1	Design 1
EU	European Union
FE	Finite element
FV	Field variables
IDF	Failure index
IP	Integration point
LL	Limit load
MPC	Multiple point constraint
OD	Onset of degradation
POSSICROSS	P OStbuckling S IMulation for Design of Fibre C OMposite Stiffened Fuselage Structures
Prepreg	Pre-impregnated
SDV	Solution dependent state variables
S	Stress of the current analyzed increment
SMAX	Maximum stress up to the analyzed increment

Acronyms and abbreviations

UD	Uni-directional
UL	Ultimate load
UMAT	User material
USDFLD	User defined field
2D	Two dimensional
3D	Three dimensional
av.	Average
coord.	Coordinate
el.	Elastic
incr.	Increment
mat.	Material
max.	Maximum
min.	Minimum
thick.	Thickness

1. Introduction

1.1 The intention of this work

The main topic of this thesis was perform out numerical simulation of thin-walled stringer stiffened CFRP-panels that are primarily limited by their buckling and postbuckling behavior. Nonlinear analyses were carried out using the simulation tool ABAQUS/Standard. User subroutines were included to simulate the property degradation within the adhesive that connects the skin and the stringer of the panel. In this work, further investigation of the user subroutines was performed as well as subsequent development of the routines themselves in order to investigate the influence of different failure criteria on the debonding of skin and stringer. The higher accuracy of the simulation of collapse is the first step towards composite aerospace structures where some degradation is permitted. Extensive experimental data, which is essential to validate the numerical results, was compared to the numerical analyses. Numerous simulations were performed in order to check the sensitivity of certain parameters and to receive similar results to the experimental data. The simulations also aimed at receiving an asymmetric buckling shape that was shown by the experiment. These analyses took geometric imperfection of the skin, the stringers and the lateral edges into account. Also single buckling modes as well as superimposed buckling modes from an eigenvalue analysis were utilized as “artificial” imperfections in the nonlinear analysis. The influence of imperfections due to unsymmetrical loading on the buckling behavior of the panel was also simulated. This work contributes directly to the project COCOMAT that is described in the following section.

1.2 The COCOMAT project

The European aircraft industry demands a reduction of the development and operating costs by 20% to 50% in the short and long term, respectively. The COCOMAT project (*Improved **MAT**erial Exploitation at Safe Design of **CO**mposite Airframe Structures by Accurate Simulation of **CO**llapse*), a four year project which began in January 2004, is supported by the European Commission and contributes to this aim by a reduction of structural weight at safe design. This means that the project aims at allowing structural weight reduction by exploiting considerable reserves in primary fiber composite fuselage structures through accurate and reliable simulations of postbuckling and collapse.

The COCOMAT project is a Specific Targeted Research Project within the 6th EU Framework Programme and is partially financed by the EU. There are partners from different countries in the European Union as well as from Switzerland, Israel and Australia working on this project, mainly universities (Table 1-1), research establishments (Table 1-2) and aircraft companies (Table 1-3).

University	Country
Karlsruhe University (UKA)	Germany
Politecnico di Milano (POLIMI)	Italy
Riga Technical University (RTU)	Latvia
RWTH Aachen	Germany
Israel Institute of Technology (TECHNION)	Israel

Table 1-1 Universities participating in COCOMAT

Research establishment	Country
Cooperative Research Centre for Advanced Composite Structures (CRC-ACS)	Australia
German Aerospace Center (DLR)	Germany
Swedish Defence Research Agency (FOI)	Sweden

Table 1-2 Research establishments participating in COCOMAT

Company	Country
Agusta	Italy
Gamesa Aeronautica	Spain
Hellenic Aerospace Industry (HAI)	Greece
Israel Aircraft Industries Ltd. (IAI)	Israel
PLZ Swidnik S. A.	Poland
Samtech S. A.	Belgium
SMR S. A.	Switzerland

Table 1-3 Aircraft companies participating in COCOMAT

COCOMAT is based upon the results of the POSICOSS project (January 2000 to September 2004). POSICOSS stands for *Improved **PO**stbuckling **SI**mulation for Design of Fiber **CO**mposite **St**iffened Fuselage Structures*. As with the COCOMAT project, this was also coordinated by the DLR's Institute of Composite Structures and Adaptive Systems, as the former Institute of Structural Mechanics. During the POSICOSS project improved fast and reliable procedures for buckling and postbuckling analysis of fiber composite stiffened panels of future fuselage structures were developed. Experimental data bases were created for the purpose of validation and design guidelines were derived.

The COCOMAT project extends the POSICOSS results by including a detailed simulation of collapse. In the project, collapse is defined as the point on the load-shortening curve where a sharp decrease occurs. Therefore, knowledge about degradation due to static and low cycle loading in the postbuckling range is required. It is already well-known that thin-walled structures that are made of carbon fiber-reinforced plastics are able to tolerate repeated buckling without changes in their buckling behavior, but in the COCOMAT project it is investigated how far in the post buckling regime loading one can go without doing severe damage to the structure. The second question that is worked on in the project is how this can be predicted by fast and precise simulation procedures.

COCOMAT strives to accomplish the step from the current (Figure 1-1a) to a future design scenario (Figure 1-1b) of typical stringer stiffened composite panels. The simplified load-shortening curve consists of three different regions. The first region (I) is shown in green and covers loads that are allowed under operating flight conditions and extends up to the "limit load" (LL). Limit loads are defined as the maximum loads that a structure must be able to withstand without permanent (plastic) deformation. Region II (yellow) is the safety region and bounded above by the so called "ultimate load" (UL). Ultimate loads are the loads that a structure must be able to withstand for three seconds without the total failure of the structure. Region III comprises the disallowed area that extends up to collapse. In aircraft design there is, in general, a safety factor of 1.5 between the limit load and the ultimate load. This means that the ultimate load amounts to 150% of the limit load. As shown in Figure 1-1a there still is a great unexploited structural reserve capacity between the current ultimate loads and collapse. The right graph of Figure 1-1 shows the future design scenario which is the long term goal of the COCOMAT project. The onset of degradation is shifted from the not allowed

region III to the safety region II due to reliable simulation of collapse, but it still has to be guaranteed that in no case the onset of degradation is allowed to occur below limit loads. Another difference between the scenarios is that the ultimate load is moved towards collapse as close as possible. This extension requires an accurate and reliable simulation of collapse. Therefore it is necessary to take into account degradation under static and low cycle loading as well as geometrical nonlinearity.

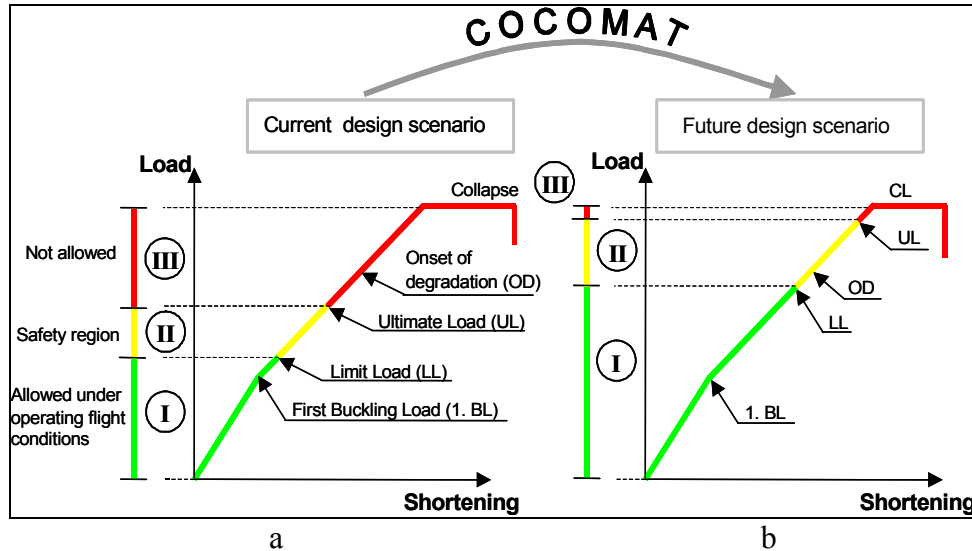


Figure 1-1 Main objective of COCOMAT project

An economic design process of new airplane design should be possible with new computation tools. These tools include fast tools for the design as well as the necessary slow and accurate tools that are required for the final certification. Therefore the goal of COCOMAT is to improve existing slow and fast simulation tools as well as to create design guidelines for stiffened panels that take material degradation and the separation of skin and stringer into account. The results of the project will comprise an extended data base on material properties and on collapse of undamaged and predamaged statically and cyclically loaded structures, as well as degradation models, improved slow and fast tools and design guidelines.

1.3 The objectives of this work

The goals of this work can be divided into two main sections. In order to form a base for these two tasks, a comprehensive literature review on all relevant topics for an investigation of degradation for axially compressed CFRP panels was performed. Furthermore the FE tools ABAQUS/Standard (ABAQUS) and MSC.Patran (Patran) were studied as the software tools used in this work.

The first main goal was to analyze and modify previously developed user subroutines to simulate the degradation of the adhesive layer that connects the skin and the stringers. Within this goal, parametric studies were performed to get an overview of the influence of different parameters on the analysis performance and results of previously developed subroutines. The next step was to change the previously developed degradation subroutines. This was done with regard to the comparison of the stress values. The subroutines were adapted for different failure criteria. As a first step, this work aimed at the implementation of typical failure criteria, for example the von Mises stress and the principal stresses into the subroutines. Also normal and shear stresses were used for the prediction of failure. These criteria were included

to evaluate the influence of the different criteria. It was not yet the main goal to include the failure criterion that was assumed to give the most realistic prediction of adhesive failure. This criterion will probably be investigated in future works. The changes in the subroutines were programmed in FORTRAN.

The second main goal of this work was to compare the experimental data of a test performed on a panel similar to the panels used within the COCOMAT project to the simulation performed including the degradation subroutines in ABAQUS. Numerous analyses were performed to check the sensitivity of certain parameters and to receive similar results in the experiment and the simulations. Geometric imperfections as imperfections of the skin and the stringer were simulated. Eigenvalue analyses were performed to utilize single buckling modes and superimposed buckling modes as artificial imperfections in the nonlinear analysis. Imperfections due to asymmetrical loading of the panel were also simulated. The experimental strain gage data was compared to simulation data and different versions of the USDFLD were compared to the experimental results.

Finally, recommendations for the further testing and verification were made with regard to the upcoming tests of the COCOMAT panels.

1.4 The structure of this work

In the first chapter, a brief overview of the work is given. The main topics of the thesis are introduced and the structure of the work is summarized. Furthermore, the COCOMAT project in which the work is part of is presented. The work was developed based on the chronological progression in the handling of the different work tasks.

The second chapter gives a literature review of the main topics related to the objective of the thesis. This review includes a brief overview of fiber-reinforced composites and Classical Laminate Theory. A description of adhesive joints is also given and the concept of the finite element method is derived from the principle of minimum energy and finally the concept of nonlinear FE analysis is introduced in order to give a better understanding of this analysis method.

In Chapter 3, the previously developed subroutines USDFLD, UMAT explicit and UMAT implicit are introduced. The chapter describes the data flow of the different subroutines and the definition of the variables used. A brief comparison of the usability and accuracy of the subroutines is also given based on the results in [17].

In the fourth chapter, a short description of the used model of the panel is given. This chapter includes a brief description of geometric parameters of the panel and the materials used to simulate the behavior of the panel materials, for example the adhesive and the fiber. The FE-model, including the elements and the mesh, is also described.

Within the fifth chapter, parametric studies investigating the user subroutines were performed to gain a better understanding of numerous parameters that influence the results and numerical stability of the calculations. These parameters include the PNEWDT factor, which is used to reduce the increment size in the case that different conditions are satisfied. Also the stress ratio steering the increment size for the UMAT implicit advanced and the comparison stress value for the USDFLD were varied in course of the parametric studies. Changes in the simulation model itself, for example the variation of the number of elements in the adhesive

and the thickness of the adhesive itself, were also investigated. Finally, two new versions of the USDFLD were developed that were based on different failure criteria and additionally were able to distinguish between element failure due to compression or tension. One version took the normal stress components as relevant stresses for the prediction of failure into account while the other version used the principal stresses. Since the structure of this work was based on the chronological development of the routines, the version that uses the normal stresses for the prediction of failure was included although there was no realistic physical context for this attempt. Still, the code of the USDFLD that used the principal stresses was based on the conclusions made from this version.

Chapter 6 describes the experimental testing of a panel similar to the panels used in the COCOMAT project performed at the DLR. A brief overview of the measurement technique used is also given. Finally, the results of the experimental testing are compared to the simulation results and several conclusions are made from this comparison.

Another main topic of this work is given in Chapter 7. In this chapter, various possible influences on the model were investigated, for example geometrical imperfection in the skin and the stringer thicknesses. Eigenvalue buckling analyses were performed and the influence of asymmetrical loading as a representation of geometrical imperfection was also investigated. These analyses were performed in order to evaluate the influence of the described factors on the buckling behavior of the panel. Also the measurement data of the strain gages were evaluated in order to detect possible source of the buckling behavior of the panel and different versions of the subroutine USDFLD were compared to the experimental data.

Chapter 8 gives the summary and conclusion of this work with regard to the upcoming experimental testing of the final COCOMAT panels at the DLR in spring 2006.

In the ninth chapter, the table of reference is given. An overview of the different user subroutines and the input files is included in Appendices A and B.

2. Literature Review

In this chapter, a literature review on three different topics is given. Firstly, the principals of fiber-reinforced composite materials are introduced as described in [22], [2] [9] and [11] because the skin and stringer of the panels investigated in this work are modeled with this material. Secondly, a section of adhesive joints gives an overview of different mechanical connections and adhesive failure criteria. Finally, the finite element method (FEM) is derived from the minimum of potential energy and an introduction is given to the deformation method [16]. Furthermore, the application and usage of FE-tools is explained and the Newton-Raphson method is described as given in [1] as method for nonlinear analysis.

2.1 Fiber-reinforced materials

Composite materials are usually made of two different materials. The characteristics of the single material differ very much from the combination of the two materials, which is constructed by embedding one material, the fiber, into the other material, the matrix. Loads are normally conducted in the composite by tension and compression in the direction of the fiber. Therefore it is possible to adjust the design of the composite to the load case by changing the direction of the fiber, as well as the number of layers used in the composite and the thickness of the single layers.

2.1.1 Stresses and deformations in fiber-reinforced materials

When discussing the mechanics of fiber-reinforced material it is normal to use an orthogonal coordinate system which has the 1-axis aligned with the fiber direction. The 2-axis is also in the plane and therefore perpendicular to the fibers and the 3-axis is perpendicular to the plane of the layer. This coordinate system is shown in Figure 2-1.

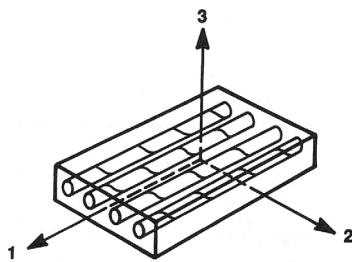


Figure 2-1 Local coordinate system of single fiber layer [2]

Materials with the same properties in all directions are called isotropic. Therefore Hookes law of elasticity given in Equation 2-1 does not depend on the direction of the main axis. The law characterizes the elastic region of the load-carrying capacity.

$$\sigma = E \cdot \varepsilon \quad (2-1)$$

where σ is the stress, E is the Young's modulus and ε represents the strain. This is the simplest form of linear elasticity and the strain-stress relationship for an isotropic material with three planes of symmetry is given by

$$\begin{bmatrix} \varepsilon_x \\ \varepsilon_y \\ \varepsilon_z \\ \gamma_{xy} \\ \gamma_{yz} \\ \gamma_{xz} \end{bmatrix} = \begin{bmatrix} \frac{1}{E} & -\frac{\nu}{E} & -\frac{\nu}{E} & 0 & 0 & 0 \\ -\frac{\nu}{E} & \frac{1}{E} & -\frac{\nu}{E} & 0 & 0 & 0 \\ -\frac{\nu}{E} & -\frac{\nu}{E} & \frac{1}{E} & 0 & 0 & 0 \\ 0 & 0 & 0 & \frac{1}{G} & 0 & 0 \\ 0 & 0 & 0 & 0 & \frac{1}{G} & 0 \\ 0 & 0 & 0 & 0 & 0 & \frac{1}{G} \end{bmatrix} \cdot \begin{bmatrix} \sigma_x \\ \sigma_y \\ \sigma_z \\ \tau_{xy} \\ \tau_{yz} \\ \tau_{xz} \end{bmatrix} \quad (2-2)$$

For the isotropic case, elastic properties are completely defined by the Young's modulus, E , and the Poisson's ratio, ν , because the shear modulus, G , can be expressed in terms of E and ν :

$$G = \frac{E}{2 \cdot (1 + \nu)} \quad (2-3)$$

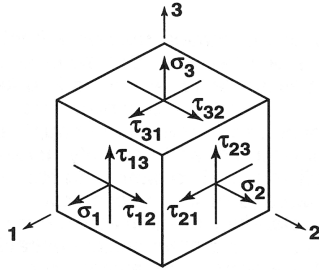


Figure 2-2 Stress state in a volume element [2]

Figure 2-2 illustrates a small element of smeared fiber-reinforced material. The normal stress acting on the element face with its outward normal in the 1-direction is called σ_1 . The shear stress that is acting in the 2-direction on the same face is as denoted τ_{12} and the other shear stress on that face in the 3-direction is denoted as τ_{13} . In Equation 2-4 the displacements u , v and w correspond to the coordinates 1, 2 and 3 or x , y , and z . The displacements are used to calculate the normal strains and the shear strains in the different direction.

$$\varepsilon_x = \varepsilon_1 = \frac{\partial u}{\partial x}$$

$$\varepsilon_y = \varepsilon_2 = \frac{\partial v}{\partial y}$$

$$\varepsilon_z = \varepsilon_3 = \frac{\partial w}{\partial z} \quad (2-4)$$

$$\gamma_{xy} = \gamma_{12} = \frac{\partial u}{\partial y} + \frac{\partial v}{\partial x}$$

$$\gamma_{xz} = \gamma_{13} = \frac{\partial w}{\partial x} + \frac{\partial u}{\partial z}$$

$$\gamma_{yz} = \gamma_{23} = \frac{\partial v}{\partial z} + \frac{\partial w}{\partial y}$$

There is a dependence between the normal strain ε and the shear strain γ . A useful transition can be made between ε and γ by Equation 2.4a. This equation shows the transition for the x-y plane. The transitions for the other planes can be done analogously.

$$\varepsilon_{xy} = \frac{1}{2} \gamma_{xy} \quad (2-4a)$$

Although we assume the fiber reinforcement to be smeared over the volume of the material and that therefore the two-material fiber system is replaced by one single homogenous material, the single material does not have the same properties in all directions. The maximum value of the Young's modulus E_1 of a fiber layer occurs when the fiber is aligned with 0° to the principal axis. The material is stronger and stiffer in the 1-direction than in the perpendicular 2- and 3-directions, although the properties in 2- and 3-directions are not necessarily equal to each other. When the angle between the direction of the fiber and the principal axis is increased, the stiffness decreases rapidly until it reaches its minimum at an angle of 90° . The shear modulus G reacts differently to the change of angle and it reaches its maximum at an angle of 45° . A material which's elasticity properties depend on the direction but do not have coupling between the normal strains and the shear strains is called orthotropic. Since the material behavior depends on the direction, orthotropic material behavior always refers to a defined coordinate system. Out of this coordinate system, the material behavior is anisotropic. Orthotropic materials are orthotropic in the axis of symmetry.

In an orthotropic material, linear elasticity is mostly defined by giving the "engineering constants", namely the three E-moduli E_1, E_2, E_3 , the three Poisson's ratios $\nu_{12}, \nu_{13}, \nu_{23}$ and the shear moduli G_{12}, G_{13}, G_{23} associated with the material's principal directions. The indices of the Poisson's ratios can be interpreted physically, where ν_{12} characterizes the transverse strain in the 1-direction, when the material is stressed in the 2-direction. The zero entries in the upper right and lower left portions of both, the compliance and stiffness matrices characterize orthotropic behavior. If a material is orthotropic and the stress-strain relations are written in the principal coordinate material system, the compliance and the stiffness matrices will always have these zero entries.

$$\begin{bmatrix} \varepsilon_1 \\ \varepsilon_2 \\ \varepsilon_3 \\ \gamma_{12} \\ \gamma_{13} \\ \gamma_{23} \end{bmatrix} = \begin{bmatrix} \frac{1}{E_1} & -\frac{\nu_{12}}{E_2} & -\frac{\nu_{13}}{E_3} & 0 & 0 & 0 \\ -\frac{\nu_{21}}{E_1} & \frac{1}{E_2} & -\frac{\nu_{23}}{E_3} & 0 & 0 & 0 \\ -\frac{\nu_{31}}{E_1} & -\frac{\nu_{32}}{E_2} & \frac{1}{E_3} & 0 & 0 & 0 \\ 0 & 0 & 0 & \frac{1}{G_{21}} & 0 & 0 \\ 0 & 0 & 0 & 0 & \frac{1}{G_{31}} & 0 \\ 0 & 0 & 0 & 0 & 0 & \frac{1}{G_{32}} \end{bmatrix} \cdot \begin{bmatrix} \sigma_1 \\ \sigma_2 \\ \sigma_3 \\ \tau_{12} \\ \tau_{13} \\ \tau_{23} \end{bmatrix} \quad (2-5)$$

A special subclass of orthotropy is transverse isotropy. It is characterized by a plane of isotropy at every point in the material. When assuming the 2-3 plane to be the plane of isotropy at every point, transverse isotropy requires that $E_1 = E_{\parallel}$, $E_2 = E_3 = E_{\perp}$, $\nu_{12} = \nu_{13} = \nu_{\perp\parallel}$, $\nu_{21} = \nu_{31} = \nu_{\perp\parallel}$, $\nu_{23} = \nu_{32} = \nu_{\perp\perp}$ and $G_{12} = G_{13} = G_{\perp\parallel}$.

$$\begin{bmatrix} \varepsilon_1 \\ \varepsilon_2 \\ \varepsilon_3 \\ \gamma_{12} \\ \gamma_{13} \\ \gamma_{23} \end{bmatrix} = \begin{bmatrix} \frac{1}{E_{\parallel}} & -\frac{\nu_{\perp\parallel}}{E_{\perp}} & -\frac{\nu_{\perp\perp}}{E_{\perp}} & 0 & 0 & 0 \\ -\frac{\nu_{\perp\parallel}}{E_{\parallel}} & \frac{1}{E_{\perp}} & -\frac{\nu_{\perp\perp}}{E_{\perp}} & 0 & 0 & 0 \\ -\frac{\nu_{\perp\parallel}}{E_{\parallel}} & -\frac{\nu_{\perp\perp}}{E_{\perp}} & \frac{1}{E_{\perp}} & 0 & 0 & 0 \\ 0 & 0 & 0 & \frac{1}{G_{\perp\parallel}} & 0 & 0 \\ 0 & 0 & 0 & 0 & \frac{1}{G_{\perp\parallel}} & 0 \\ 0 & 0 & 0 & 0 & 0 & \frac{1}{G_{\perp\perp}} \end{bmatrix} \cdot \begin{bmatrix} \sigma_1 \\ \sigma_2 \\ \sigma_3 \\ \tau_{12} \\ \tau_{13} \\ \tau_{23} \end{bmatrix} \quad (2-6)$$

For a transversely isotropic material, there are five independent material properties, E_{\parallel} , E_{\perp} , $\nu_{\perp\parallel}$, $\nu_{\perp\perp}$ and $G_{\perp\parallel}$ as $G_{\perp\perp} = \frac{E_{\perp}}{2(1+\nu_{\perp\perp})}$ and as a result of applying the Maxwell-Betti Reciprocal

Theorem as described in [9] that states that $\frac{E_{\parallel}}{\nu_{\perp\parallel}} = \frac{E_{\perp}}{\nu_{\perp\parallel}}$.

2.1.2 Simplified stresses and deformations for UD layers

The equations outlined so far in this chapter were derived for a full three dimensional case as shown in Figure 2-2. A composite consists of multiple single layers that are relatively thin. The derivation process can be simplified by focusing on one single layer when additionally the loading is in the plane of the layer.

Under plane stress conditions, such as in a shell element, the variables σ_3 , τ_{13} and τ_{23} are considered to be zero, as no through-thickness stresses are introduced for the thin composite layer. This simplified plane stress condition is accurate for UD layers. The material law is derived by deleting the rows and columns of Equation 2-6, which are set to zero as depicted in Equation 2-8.

$$\underline{\underline{\varepsilon}} = \underline{\underline{S}} \cdot \underline{\underline{\sigma}} \quad (2.7)$$

$\underline{\underline{S}}$ is the so called reduced compliance matrix.

$$\begin{bmatrix} \varepsilon_1 \\ \varepsilon_2 \\ \gamma_{12} \end{bmatrix} = \begin{bmatrix} \frac{1}{E_{\parallel}} & -\frac{\nu_{\parallel\perp}}{E_{\perp}} & 0 \\ -\frac{\nu_{\perp\parallel}}{E_{\parallel}} & \frac{1}{E_{\perp}} & 0 \\ 0 & 0 & \frac{1}{G_{\perp\parallel}} \end{bmatrix} \cdot \begin{bmatrix} \sigma_1 \\ \sigma_2 \\ \tau_{12} \end{bmatrix} \quad (2.8)$$

The assumption of a plane strain condition would be incorrect. A tensile normal stress σ_1 causes extension of the element in the 1-direction and, due to Poisson effects, contraction in the 2- and 3-direction, therefore $\varepsilon_3 \neq 0$.

$$\varepsilon_3 = S_{13} \cdot \sigma_1 + S_{23} \cdot \sigma_2 \quad (2-9)$$

Another important assumption is that in a plane stress state there can be no shear strains in the 2-3 and 1-3 planes. This means that

$$\gamma_{13} = \gamma_{23} = 0 \quad (2-10)$$

Analogous to the strain-stress equations, the stress-strain equations are given below.

$$\underline{\underline{\sigma}} = \underline{\underline{Q}} \cdot \underline{\underline{\varepsilon}} \quad (2-11)$$

$\underline{\underline{Q}}$ is called the stiffness matrix.

$$\begin{bmatrix} \sigma_1 \\ \sigma_2 \\ \tau_{12} \end{bmatrix} = \begin{bmatrix} \frac{E_{\parallel}}{1 - \nu_{\perp\parallel} \cdot \nu_{\parallel\perp}} & \frac{E_{\parallel} \cdot \nu_{\parallel\perp}}{1 - \nu_{\perp\parallel} \cdot \nu_{\parallel\perp}} & 0 \\ \frac{E_{\perp} \cdot \nu_{\perp\parallel}}{1 - \nu_{\perp\parallel} \cdot \nu_{\parallel\perp}} & \frac{E_{\perp}}{1 - \nu_{\perp\parallel} \cdot \nu_{\parallel\perp}} & 0 \\ 0 & 0 & G_{\perp\parallel} \end{bmatrix} \cdot \begin{bmatrix} \varepsilon_1 \\ \varepsilon_2 \\ \gamma_{12} \end{bmatrix} \quad (2-12)$$

2.1.3 Derivation of Classical Laminate Theory

Classical Laminate Theory is required in order to apply the stiffness of a single layer to an entire composite. The theory is based on different assumptions:

- In composites the single layers are very thin, with one geometric dimension that is an order of magnitude less than the other two dimensions. When the loading is also applied in the plane of the composite layer, all stress components perpendicular to the plane of the structure can be set to zero. In the context of fiber-reinforced materials the stress components σ_3 , τ_{13} and τ_{23} can be set to zero.
- The state of stress is in-plane.
- Every single layer is considered to be homogenous. This means that the material has the same properties at every point. This includes a constant stiffness and flexibility.
- The material behavior is assumed to be linear elastic.
- The layers are connected rigidly. The displacements and the strains have a consistent distribution through the layer's thickness.
- In the Kirchhoff-Hypothesis for plates the through-thickness extensional strain ϵ_3 is predicted to be zero. This is an inconsistency because in Equation 2-9 it was proved that ϵ_3 is not equal to zero.
- Inter-laminate stresses are neglected.

The UD layer:

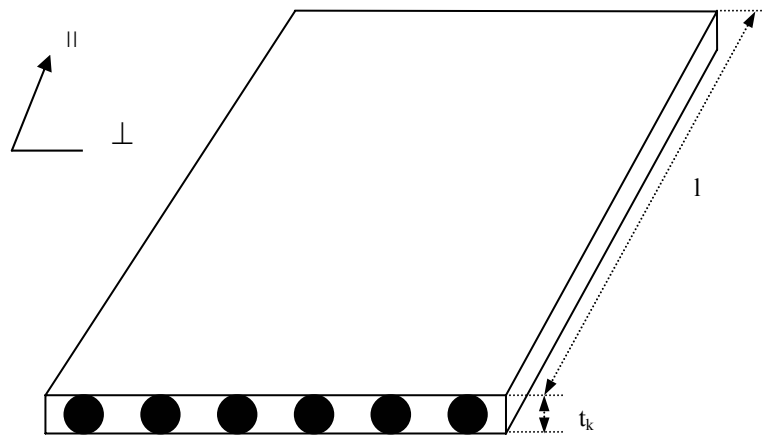


Figure 2-3 Local coordinate system of a single fiber layer [20]

Figure 2-3 shows a UD layer. UD layers are layers in which all fibers lay parallel with the same angle to the global coordinate system. Depending on the orientation of the load that is applied to the layer this might be seen as a parallel connection in the case that the load is parallel to the fiber or as series connection when the load is applied orthogonal to the fiber. In the following derivation, the index f represents the fiber and the index m represents the matrix.

Young's modulus parallel to the fiber $E_{||}$:

$$\sum F_{||} = F_f + F_m$$

$$\Delta l_{||} = \Delta l_m$$

$$\begin{aligned}
 \frac{\Delta l_f}{l_0} &= \frac{\Delta l_m}{l_0} \rightarrow \varepsilon_f = \varepsilon_m \\
 \sigma_f &= E_{f\parallel} \cdot \varepsilon_f \\
 \sigma_m &= E_m \cdot \varepsilon_m \\
 F_{\parallel} &= \sigma_f \cdot A_f + \sigma_m \cdot A_m \\
 E_{\parallel} \cdot A_{total} &= E_{f\parallel} \cdot A_f + E_m \cdot A_m \\
 E_{\parallel} &= \frac{E_{f\parallel} \cdot A_f + E_m \cdot A_m}{A_{total}}
 \end{aligned} \tag{2-13}$$

Introducing the portion of the fiber φ :

$$\varphi = \frac{V_f}{V_{total}} = \frac{A_f \cdot l_0}{A_m \cdot l_0} \tag{2-14}$$

$$E_{\parallel} = E_{f\parallel} \cdot \varphi + E_m (1 - \varphi) \tag{2-15}$$

This equation is only correct under the assumption that the Poisson's ratios of the fiber and the matrix are the same.

Young's modulus perpendicular to the fiber E_{\perp} :

$$\begin{aligned}
 F_{\perp} &= F_f = F_m \\
 \Delta l &= \Delta l_f + \Delta l_m \\
 \sigma_f &= E_{\perp} \cdot \varepsilon_f \\
 \sigma_m &= E_m \cdot \varepsilon_m \\
 \Delta l &= \frac{\sigma_f \cdot l_f}{E_{f\perp}} + \frac{\sigma_m \cdot l_m}{E_m} = \frac{F_{\perp}}{A} \cdot \frac{l_f}{E_{f\perp}} + \frac{F_{\perp}}{A} \cdot \frac{l_m}{E_m} \\
 \sigma_{\perp} &= E_{\perp} \cdot \varepsilon_{\perp} = E_{\perp} \cdot \frac{\Delta l}{l_0} \\
 \Delta l &= \frac{\sigma_{\perp} \cdot l_0}{E_{\perp}} = \frac{F_{\perp}}{A} \cdot \frac{l_0}{E_{\perp}} \\
 \frac{l_0}{E_{\perp}} &= \frac{l_f}{E_{f\perp}} + \frac{l_m}{E_m} \\
 \frac{1}{E_{\perp}} &= \frac{1}{E_{f\perp}} \cdot \frac{l_f}{l_0} + \frac{1}{E_m} \cdot \frac{l_m}{l_0} \\
 \text{with: } \frac{l_m}{l_0} &= \frac{l_0 - l_f}{l_0} \\
 E_{\perp} &= E_m \frac{1}{\left(1 - \frac{l_f}{l_0}\right) + \frac{E_m}{E_{f\perp}} \cdot \frac{l_f}{l_0}}
 \end{aligned} \tag{2-16}$$

In this equation, the value of E_{\perp} is overestimated because the considered cross section includes the maximum portion of the fiber. In other cross sections, the portion of the fiber might be considerably smaller. In order to approximate the Young's modulus, the portion of the fiber is included into the calculation as shown in Equation 2-16a.

$$E_{\perp} = E_m \cdot \frac{1}{(1-\varphi) + \frac{E_m}{E_{f\perp}} \cdot \varphi} \quad (2-16a)$$

It has to be mentioned that this equation still is an approximation because different effects, for example the hindering effect of the stiff fiber to the matrix material is not taken into consideration.

To be able to derive the other equations for an UD layer there are several other equations needed for the thickness of the layer t and the Poisson's ratios. The following equations are taken from [11].

$$t = \frac{G_A}{\rho_f \cdot \varphi} \quad (2-17)$$

where G_A represents the weight of the composite in reference to the area.

$$\begin{aligned} \nu_{\perp\parallel} &= \nu_f \cdot \varphi + \nu_m (1 - \varphi) \\ \nu_{\parallel\perp} &= \nu_{\perp\parallel} \frac{E_{\perp}}{E_{\parallel}} \end{aligned} \quad (2-18)$$

$$\begin{aligned} D_{\parallel}^* &= E_{f\parallel} \cdot \frac{G_A}{\rho_f} + E_m \left(t - \frac{G_A}{\rho_f} \right) \\ D_{\perp}^* &\approx \frac{E_m \cdot t}{(1-\varphi)^{1.35}} \end{aligned} \quad (2-18a)$$

The extensional rigidity is given by:

$$\begin{aligned} D_{\parallel} &= \frac{D_{\parallel}^*}{1 - \nu_{\perp\parallel} \cdot \nu_{\parallel\perp}} \\ D_{\perp} &= \frac{D_{\perp}^*}{1 - \nu_{\perp\parallel} \cdot \nu_{\parallel\perp}} \\ D_{\parallel\perp} &= \nu_{\parallel\perp} \cdot D_{\perp} \end{aligned} \quad (2-19)$$

With the shear rigidity for fibers:

$$D_{\#} = \frac{(1 + 0.6\sqrt{\varphi}) \cdot G_m \cdot t}{(1 - \varphi)^{1.35}} \quad (2-20)$$

For fibers with high orthotropy or a portion of fiber greater than 60% the following equation should be used:

$$D_{\#} = \frac{(1 + 0.6\sqrt{\varphi}) \cdot G_m \cdot t}{\varphi \cdot \frac{G_m}{G_f} + (1 - \varphi)^{1.25}} \quad (2-21)$$

The composite:

A composite is composed of a number of single layers with different fiber orientations defined with respect to the global coordinate system. It is possible to calculate the stiffness of a composite by adding the stiffnesses of the single layers if, and only if, the layers of the composite have been previously transformed into the global coordinate system.

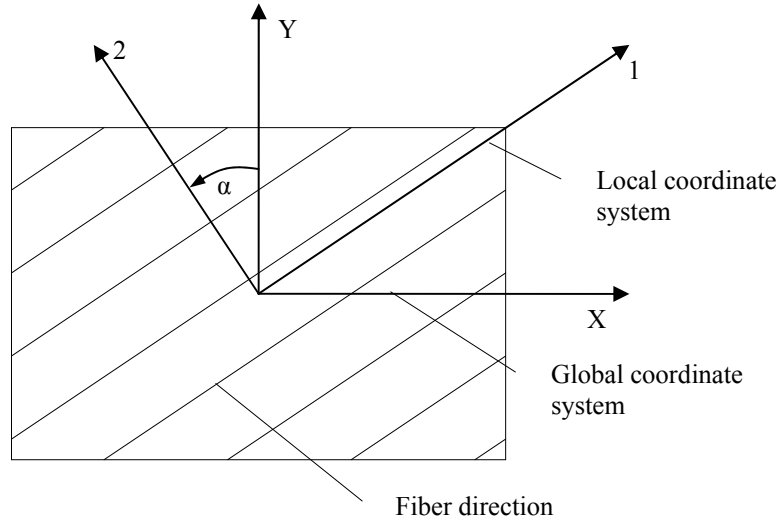


Figure 2-4 Local and global coordinate system of a single UD layer

Figure 2-4 shows the relation between local and global coordinate systems. The local coordinate system is shown with its 1-axis into the direction of the fiber. The global coordinate is rotated around the Z-axis by the angle α . The necessary transformation of internal forces from the local to the global coordinate system is performed by the following transformation relations.

$$\begin{aligned} D_{1k} &= D_{\perp\parallel k} + 2 \cdot D_{\#k} \\ D_{2k} &= D_{\parallel k} + D_{\perp\parallel k} - 2 \cdot D_{1k} \\ D_{11k} &= D_{\parallel k} \cdot \cos^4(\alpha_k) + D_{\perp k} \cdot \sin^4(\alpha_k) + 0.5 \cdot D_{1k} \cdot \sin^2(2 \cdot \alpha_k) \\ D_{22k} &= D_{\perp k} \cdot \cos^4(\alpha_k) + D_{\parallel k} \cdot \sin^4(\alpha_k) + 0.5 \cdot D_{1k} \cdot \sin^2(2 \cdot \alpha_k) \\ D_{66k} &= D_{\#k} + 0.25 \cdot D_{2k} \cdot \sin^2(2 \cdot \alpha_k) \end{aligned} \quad (2-21)$$

$$D_{12k} = D_{\perp\parallel k} + 0.25 \cdot D_{2k} \cdot \sin^2(2 \cdot \alpha_k)$$

$$D_{16k} = -0.5 \cdot (D_{2k} \cdot \sin^2(\alpha_k) - (D_{\parallel k} - D_{1k})) \cdot \sin(2 \cdot \alpha_k)$$

$$D_{26k} = -0.5 \cdot ((D_{\perp k} - D_{1k}) - D_{2k} \cdot \sin^2(\alpha_k)) \cdot \sin(2 \cdot \alpha_k)$$

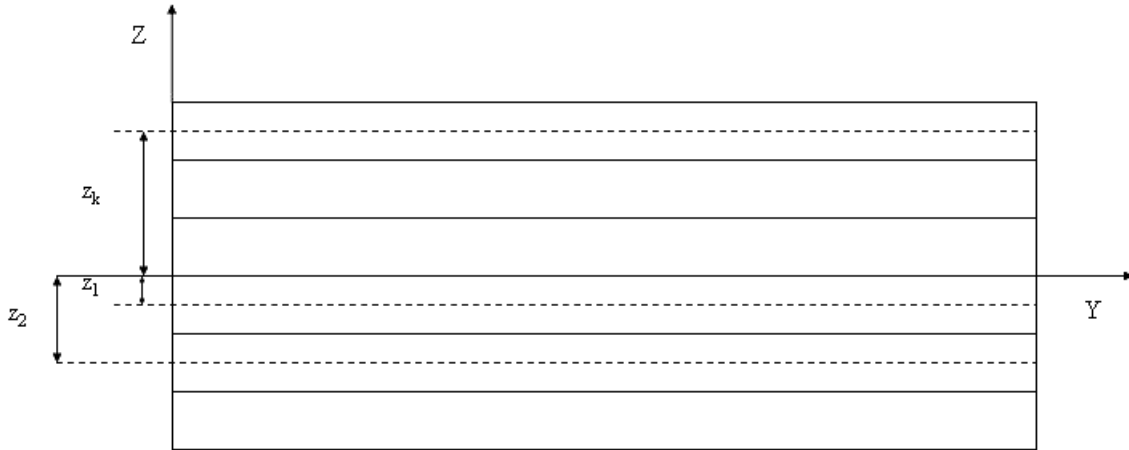


Figure 2-5 Definition of lever arms of single layers in coordinate system

As can be concluded from Figure 2-5, the bending rigidity of the composite depends on the lever arm of the single layers z_k where k represents the corresponding layer. With the equations for the extensional rigidity D_{ij} it is possible to calculate the bending rigidity B_{ij} as shown in Equation 2-22.

$$B_{ij} = \sum_{k=1}^n D_{ij,k} \left(\frac{t_k^2}{12} + z_k^2 \right) \quad (2-22)$$

In the case of laminates which do not have a symmetric design configuration, the coupling rigidity K_{ij} is calculated by:

$$K_{ij} = \sum_{k=1}^n D_{ijk} \cdot z_k \quad (2-23)$$

In Figure 2-6 the orientations of the internal forces and moments are shown.

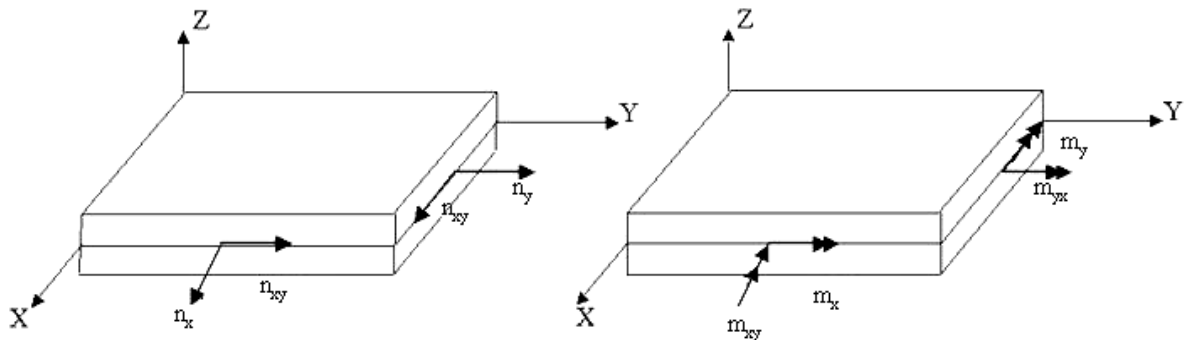


Figure 2-6 Orientation of internal forces and moments

The internal forces and moments are derived from the stress relations. The three force resultants and the three moment resultants are the result of integrating the stresses through the thickness of the laminate. The stress resultants in the x and y-direction, n_x and n_y , which are called the normal force resultants, the shear force resultant, n_{xy} , as well as the bending moment resultants, m_x and m_y , and the twisting moment resultant, m_{xy} , are defined in the following equations.

$$\begin{aligned}
 n_x &= \int_{z_0}^{z_n} \sigma_x dz & m_x &= \int_{z_0}^{z_n} \sigma_x \cdot z dz \\
 n_y &= \int_{z_0}^{z_n} \sigma_y dz & m_y &= \int_{z_0}^{z_n} \sigma_y \cdot z dz \\
 n_{xy} &= \int_{z_0}^{z_n} \tau_{xy} dz & m_{xy} &= \int_{z_0}^{z_n} \tau_{xy} \cdot z dz
 \end{aligned} \tag{2-24}$$

The definition of the force and moment resultants involves the stresses σ_x , σ_y and τ_{xy} . It is possible to form one matrix relation between the six stress resultants and the six reference surface deformations. The combined matrix is known as the laminate stiffness matrix and in the following equation:

$$\begin{bmatrix} n_x \\ n_y \\ n_{xy} \\ m_x \\ m_y \\ m_{xy} \end{bmatrix} = \begin{bmatrix} D_{11} & D_{12} & D_{16} & K_{11} & K_{12} & K_{16} \\ D_{21} & D_{22} & D_{26} & K_{21} & K_{22} & K_{26} \\ D_{61} & D_{62} & D_{66} & K_{61} & K_{62} & K_{66} \\ K_{11} & K_{12} & K_{16} & B_{11} & B_{12} & B_{16} \\ K_{21} & K_{22} & K_{26} & B_{21} & B_{22} & B_{26} \\ K_{61} & K_{62} & K_{66} & B_{61} & B_{62} & B_{66} \end{bmatrix} \cdot \begin{bmatrix} \varepsilon_x^0 \\ \varepsilon_y^0 \\ \varepsilon_{xy}^0 \\ \kappa_x \\ \kappa_y \\ \kappa_{xy} \end{bmatrix} \tag{2-25}$$

Where:

<u>D</u>	Extensional or membrane stiffness matrix	[N/mm]
<u>K</u>	Coupling stiffness matrix	[N]
<u>B</u>	Flexural or bending stiffness matrix	[Nm]

κ is the so called bending, which is defined as the reciprocal value of the bend radius as stated in Equation 2-26.

$$\kappa = \frac{1}{\rho} \approx w'' \tag{2-26}$$

The global strains of the layers can be calculated by:

$$\begin{aligned}
 \varepsilon_{x,k} &= \varepsilon_x^0 + \kappa_x \cdot z_k \\
 \varepsilon_{y,k} &= \varepsilon_y^0 + \kappa_y \cdot z_k \\
 \varepsilon_{xy,k} &= \varepsilon_{xy}^0 + \kappa_{xy} \cdot z_k
 \end{aligned} \tag{2-27}$$

2.2 Adhesive Joints

2.2.1 General overview

In the COCOMAT project the stringer is connected to the skin of the panel by an adhesive layer. Therefore it is necessary to understand the function and characteristics of this kind of bonding more thoroughly. In order to achieve a better understanding of this connection, an overview is given in the following section.

The purpose of an adhesive joint is to connect two similar or different metallic or non-metallic surfaces due to surface adhesion. Adhesive joints are not to be separated without the destruction of the adhesive or the connected parts. This means that they belong to the group of inseparable connections. Today adhesive joints are the standard joining method in the field of composite structures.

In comparison to mechanical fasteners, adhesively bonded joints have many advantages especially when composite layers are to be connected. The main advantage is that there is no need to damage the adhered materials by drilling holes as is necessary for rivets or screws. This would be problematic for composite structures because this kind of structure is not able to decrease stress peaks by yielding as is possible in metallic materials. Since it is not necessary to damage the structure as for the use of mechanical fasteners, a reduction of the weight is possible. Another advantage is that adhesives resist corrosion, and in particular corrosion due to the direct contact of the two joined materials. Adhesives also have some disadvantages as well, for example a high tendency to creep under long term loads. It is also difficult to predict the quality of an adhesive joint without destructive testing.

The strength of adhesive joints depends on different factors, for example the ductility of the material and the geometrical form of the connection. Normally adhesive joints are to be designed in such a way that the only forms of loading are shear or tension/compression as shown in Figure 2-7 a and b. The load capacity is heavily dependent on the geometry of the joint. This means that it is important to distinguish whether the design is symmetric and also whether the load path is symmetric or non-symmetric. It is known that adhesively bonded joints are weak in peel stress (Figure 2-7 c). Since composites are also weak in inter-laminar tension, it is also important to minimize the influence of these loads in the design.

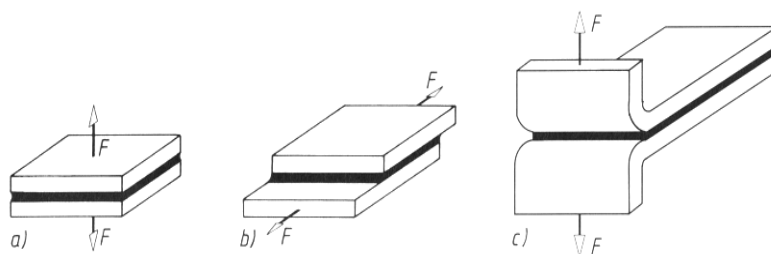


Figure 2-7 Loading forms of adhesive joints [19]

As was mentioned earlier, it is hard to predict the quality of an adhesive joint without destructive testing. Therefore, adhesive joints have to be manufactured very precisely; the surfaces that are to be bonded together have to be prepared carefully.

2.2.2 Bonding mechanisms of adhesive joints

The strength of every adhesive bonding depends on the physical properties of the materials that are to be joined together and of the adhesive itself. The attraction power of the boundary surfaces of two substances is called adhesion. It consists mainly of intermolecular gravity, or the so called “Van der Waals forces”. The forces in between the molecules of one substance are called cohesion. Adhesion is composed of intermolecular gravity and additionally a mechanical locking of polymeric molecules. The Van der Waals forces have a range of only 3 nm. This is smaller than the best surface roughness manufactured by professional means. Therefore the adhesive has to infiltrate the surface structure. The mechanism of adhesion and cohesion are shown in Figure 2-8.

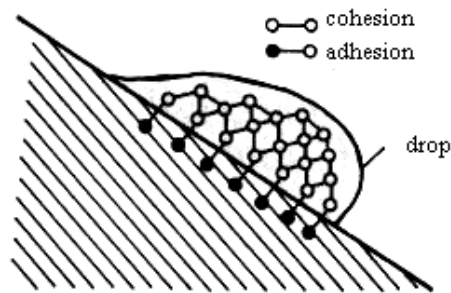


Figure 2-8 Adhesion and cohesion demonstrated at a drop of liquid on an inclined plane [19]

The Young's modulus of the adhesive layer is hard to determine because the adhesive does not necessarily follow the isotropic material law. Therefore it is not possible to calculate the Young's modulus although it is possible to measure the shear modulus. In this work, the adhesive was assumed to have isotropic material behavior as a first approximation. In contrast to metallic materials it is important to mention that in composite structures the shear strength of the adherend is in the same range as the strength of the adhesive layer.

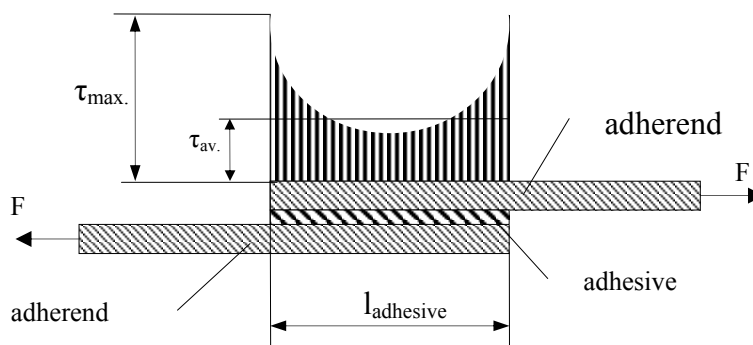


Figure 2-9 Typical single lap joint [17]

The lap shear strength is determined by tests with single lap joints as shown in Figure 2-9. The strength of the adhesive layer is calculated with Equation (2-27) that describes the relation between the collapse shear load and the adhesive area. For quick loading it can be calculated by Equation 2-27 as described in [19].

$$\tau_{av} = \frac{F}{A_{Adhesive}} \quad (2-27)$$

where $A_{Adhesive}$ is the area of the adhesive layer. It is defined as the footprint of the adherends connected to each other by the adhesive layer. F is the load that is applied parallel to the adhesive layer. This is only a simplified approximation because in reality the collapse of the adhesive is caused by the stress peaks at the edges. Therefore the stress peaks have to be minimized to avoid an early collapse of the joint. There are different construction approaches to keep the stress peaks as small as possible. Some examples are given in Figure 2-10, where different variations of the stress distribution are displayed. It is shown that the adhesive length as well as the geometry of the joint affects the distribution of the stresses.

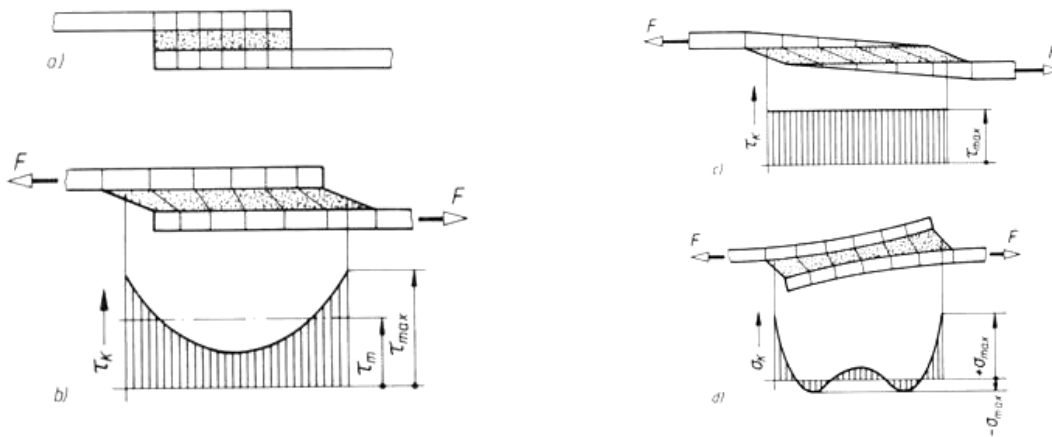


Figure 2-10 Stress distribution in adhesive joints [19]

The distribution of the shear stress along the length of the adhesive for the one dimensional state can be calculated analytically with the method of Volkersen [24].

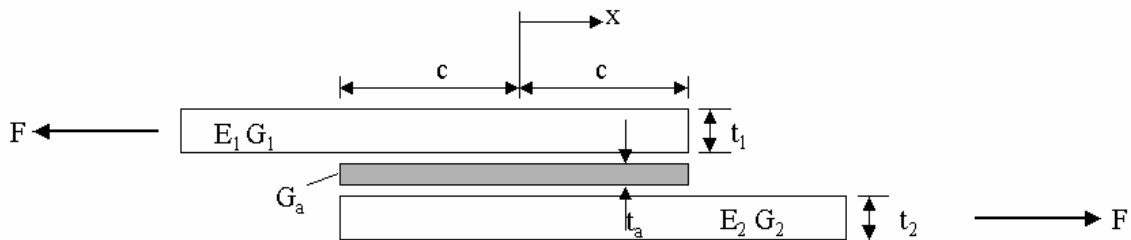


Figure 2-11 Parameters of a single lap joint used in the method of Volkersen

With the variables given in Figure 2-11 and with equilibrium of forces on the element, it is possible to derive an approximation formula to calculate the distribution of the stress over the length for the adhesive layer for the one dimensional case:

$$\tau(x) = A \cdot \sinh(\beta \cdot x) + B \cdot \cosh(\beta \cdot x) \quad (2-28)$$

This method applies the simplification that no moments are carried forward. The overlap length is set to $2c$. The coefficients A and B are derived from the boundary conditions. Finally τ_{av} is calculated with Equation (2-27).

$$A = \frac{\beta \cdot c \cdot \tau_{av}}{\cosh(\beta \cdot c)} \frac{1 - \frac{E_2 \cdot t_2}{E_1 \cdot t_1}}{1 + \frac{E_2 \cdot t_2}{E_1 \cdot t_1}} \quad (2-29)$$

$$B = \frac{\beta \cdot c \cdot \tau_{av}}{\sinh(\beta \cdot c)} \quad (2-30)$$

Where

$$\beta^2 = \frac{\frac{G_a}{t_a} \left(\frac{1}{E_1 \cdot t_1} + \frac{1}{E_2 \cdot t_2} \right)}{1 + \frac{G_a}{t_a} \left(\frac{t_1}{3 \cdot G_1} + \frac{t_2}{3 \cdot G_2} \right)} \quad (2-31)$$

These assumptions are only correct if the two laminated plates that are to be connected are modeled as UD layers. In this case it can be assumed that the tensile modulus of the fiber material can be used as E_1 of the isotropic material in the load direction. If the assumption is not fully satisfied then the engineering constants of the adherends have to be determined with CLT or the equation has to be modified so that orthotropic material constants are taken into account.

Another important characteristic value for the analysis of adhesive joints is the tensile strength. It is usually measured with a test block in the form of a single lap joint. The tensile strength is not constant, neither timewise nor regional, but depends on a variety of factors for example the adhesive used, the temperature, geometry of the adhesive joint, the roughness of the surfaces and the material of the parts which are to be bonded together. Time also plays an important role because in many adhesives the tensile strength decreases when the loading time increases.

The peel stress is another important parameter of adhesive joints. It is very unfavorable for adhesive joints in terms of strength and it should be avoided in any way because even small peel loads can still cause high stress peaks. These stress peaks initiate the breakage of the adherend and the adhesive layer. The peel strength is usually determined in tests in which loads are applied perpendicular to the adhesive layer.

2.2.3 Failure modes of adhesive joints

For adhesively bonded joints there are four main failure modes. They are categorized by the location of their occurrence.

- Adhesive failure:

This failure mode occurs when the adhesive fails to bond with the material to be adhered. This kind of failure mode depends on the adhesion of the materials to each other. Therefore it only appears on the interface. A pure adhesive failure only occurs when the break appears at the phase boundary. This means that the adherends do not show any remnants of the adhesive layers and the adhesive is entirely free of remaining parts of the adherends.

- Adherend failure:
Adherend failure is the failure mode when the adherends themselves fail. This occurs very often with fiber parts because as was mentioned earlier in this chapter, the strength of the adherends and the adhesives are usually around the same order of magnitude.
- Cohesive failure:
This means that the crack appears in the adhesive layer and the surfaces of the adherends are covered with the remainder of the adhesive. It is therefore a structural failure of the adhesive.
- Mixed mode:
In this case the breakage pattern does not look as obvious as it does in the first three failure modes. This is because it is a mixture of the three failure modes already described. The mixed mode is characterized by the adherend surfaces which are partly covered by adhesive material and partly clean.

The focus of this work is not the investigation of the failure mode. The central point is the analysis of the first appearance of failure in the adhesive when the maximum allowable stress in the adhesive is exceeded. This means that the investigated failure mode is most likely to be a kind of cohesive failure.

2.2.4 Failure criteria of the adhesive

In this work there are three different stresses analyzed to predict the failure of the adhesive layer, namely the von Mises yield stress, the normal stress and the shear stress.

The von Mises yield criterion, which is stated in Equation 2-32 [4] is important because the normal and shear stresses are already included in the calculation. The von Mises stress is a so called comparison stress, which is usually used when there are different kinds of stresses, meaning normal stresses and shear stresses in a structure. The comparison stress is compared to the maximum allowable compressive stress or maximum allowable tensile stress. If the ratio exceeds one, failure occurs.

$$\sqrt{\frac{(\sigma_1 - \sigma_2)^2 + (\sigma_2 - \sigma_3)^2 + (\sigma_3 - \sigma_1)^2}{2}} / \sigma_y \leq 1 \quad (2-32)$$

In this equation σ_y represents the maximum allowable compressive stress. In some simulations the maximum allowable compressive stress is replaced by the maximum allowable tensile stress of the adhesive which is lower than the maximum compressive stress. The hypothesis of von Mises compares the required work for the alteration of shape caused by shearing strains at the onset of creeping for the multiple axial stress state to the uniaxial stress state and derives a comparison stress. It is important to mention that as the volume is constant, the strain of the material is characterized by the energy that is required to change the shape. As was shown by experiments the hypothesis is most accurate for ductile materials and is less accurate for brittle materials. The von Mises yield stress is implemented in ABAQUS and is calculated by using the principal normal stresses of a three axis stress state. In the programmed subroutines, the von Mises stress is calculated from a stress state which is not given by the principal stresses. The formula for the three dimensional stress state is

$$\sigma_v = \sqrt{\sigma_x^2 + \sigma_y^2 + \sigma_z^2 - (\sigma_x \cdot \sigma_y + \sigma_x \cdot \sigma_z + \sigma_y \cdot \sigma_z) + 3 \cdot (\tau_{xy}^2 + \tau_{xz}^2 + \tau_{yz}^2)} \quad (2-33)$$

Additionally to the simulations that use the von Mises yield stress, simulations are performed that take the maximum normal stresses into account as failure criteria. In these cases the actual stress is compared to the maximum allowable normal stress. The failure criterion is exceeded when

$$\frac{\sigma_{current}}{\sigma_{allowable}} \geq 1 \quad (2-34)$$

The stress $\sigma_{allowable}$ theoretically still is an allowable stress. Therefore it is considered to be permitted in the material. In reality the entire aspect of failure is a flowing transition, no absolute judgment can be made.

2.3 Finite Element Method

2.3.1 Introduction and general description of FEM

The basic idea of the finite element method (FEM) is to find the solution of a complicated problem by replacing this problem with a simpler one. Since the complex problem is replaced with a simpler one, the solution derived is only an approximate solution, not the exact solution.

The FEM was developed originally for the analysis of aircraft structures [16] but because the nature of its theory is very general, it is possible to apply this method to a wide variety of boundary value problems. A boundary value problem can be described as a problem in which a solution is sought in the domain of a body subject to the satisfaction of prescribed boundary conditions on the dependent variables or their derivatives.

In the FEM, the actual continuum is divided into smaller subdivisions called finite elements. These finite elements are interconnected at specified joints, which are called nodes. These nodes lay on the boundaries of the elements where adjacent elements are connected. The problem is that the actual variation of the field variables, for example displacement or stress of the continuum, is not known. Therefore it is assumed that the variation of the field variable inside one finite element can be approximated by a simple function. These approximating functions are defined according to the values of the field variables at the nodes. When field equations, for example equilibrium equations, are formulated for the entire continuum, the new unknowns are nodal values of the field variable. The field equations are usually given in the form of matrix equations. By solving these equations, the nodal values of the field variable are calculated. When these nodal values are known, the approximating functions define the field variables throughout the assemblage of elements. It is possible to solve a general continuum problem by the finite element method by following a step-by-step procedure, which is stated for static structural problems as follows:

1. Discretization of the structure:

The structure is divided into smaller substructures, the elements. The structure needs to be modeled with suitable elements. It needs to be decided which element type and size is to be taken as well as the number and arrangement of elements.

2. Selection of interpolation model:

It is necessary to assume a suitable solution within one element to approximate the unknown solution because the displacement solution of a complex structure under a specified load cannot be predicted as exactly as required. The assumed solution has to satisfy convergence requirements but should be as simple as possible.

3. Derivation of the element stiffness matrices and the load vectors:

It is possible to derive the stiffness matrix and the load vector for one element by using the assumed displacement model. This can be done by the principle of minimum potential energy as described in Section 2.3.2.

4. Assemblage of element equations in order to obtain the overall equilibrium equations:

The overall equilibrium equations have to be formulated as

$$\tilde{K} \cdot \tilde{\Phi} = \tilde{P} \quad (2-35)$$

where \tilde{K} represents the global stiffness matrix, $\tilde{\Phi}$ is called the vector of nodal displacements and \tilde{P} is the nodal forces vector of the entire structure.

5. Solution for the unknown nodal displacements

The overall equilibrium equations, which are stated above, are modified in order to satisfy the applied boundary conditions. The equations can be expressed as:

$$K \cdot \Phi = P \quad (2-36)$$

where K , Φ and P represent the same values as they did in the former equations but after the incorporation of the boundary conditions. For linear problems, this equation can be solved easily for the vector Φ . In the case of nonlinear problems, the solution has to be obtained in a sequence of iterations where each iteration involves a modification of the stiffness matrix and/or the load vector. This is described more thoroughly in Section 2.3.5.

6. Computation of element stresses and strains

When the nodal displacement Φ is known, it is possible to compute the element stresses and strains by using the equations of solid or structural mechanics.

The terminology used above has to be modified if the concept is extended to other fields. The more general terms are continuum instead of structure, field variable instead of displacement and characteristic matrix in place of stiffness matrix.

The finite element method has been most extensively used in the field of solid and structural mechanics. In the following section, the displacement method, which is based on the principle of minimum potential energy, is used to derive the finite element equations.

2.3.2 Principal of minimum potential energy [16]

The potential energy of an elastic body Π_p is defined as

$$\Pi_p = \Pi - W_p \quad (2-37)$$

where Π is the strain energy and W_p represents the work done on the body by the external forces. Although there are numerous possible displacement states, where u , v and w are the displacements in the different axes of the coordinate system, which satisfy given kinematic or displacement boundary condition as well as compatibility, the state that satisfies the equilibrium equations makes the potential energy a minimum. The strain energy of a linear elastic body can be defined as

$$\Pi = \frac{1}{2} \int_V \boldsymbol{\varepsilon}^T \cdot \boldsymbol{\sigma} dV \quad (2-38)$$

where $\boldsymbol{\sigma}$ is the vector of stresses, $\boldsymbol{\varepsilon}$ is the strain vector and V the volume of the body. The relations between the stresses and the strains are given by the elasticity matrix D . Therefore the strain energy in the presence of initial strains $\boldsymbol{\varepsilon}_0$ can be stated as:

$$\Pi = \frac{1}{2} \int_V \boldsymbol{\varepsilon}^T D \boldsymbol{\varepsilon} dV - \int_V \boldsymbol{\varepsilon}^T D \boldsymbol{\varepsilon}_0 dV \quad (2-39)$$

With the work of the external forces:

$$W_p = \int_V \boldsymbol{\phi}^T U dV + \int_A \boldsymbol{\Phi}^T U dA \quad (2-40)$$

where Φ is the vector of tractions, ϕ is the vector of known body forces, U is the displacement vector and A is the surface of the body. With this equation the potential energy of a body can be expressed as:

$$\Pi_p = \frac{1}{2} \int_V \varepsilon^T D(\varepsilon - 2\varepsilon_0) dV - \int_V \phi^T U dV - \int_A \Phi^T dA \quad (2-41)$$

2.3.3 The displacement method [16]

The primary goal of a stress analysis is to describe the distribution of displacements and stresses under a state of loading and boundary conditions. All analytical solutions of this kind of problem have to satisfy several basic equations of solid mechanics, the equilibrium equations, the stress-strain relations and the strain-displacement relations. Additionally the continuity of strains and displacement has to be satisfied by the so called compatibility equations and the boundary conditions have to be taken into account as well.

When the principal of minimum potential energy is used to derive the finite element equation, a simple form of variation for the displacement field within each element is assumed and conditions that minimize the functional I , which is the same as the potential energy Π_p , are derived. The resulting equations are the approximate equilibrium equations, with the compatibility conditions satisfied as well. This method is called the displacement or stiffness method of finite element analysis. It is explained in more detail in the following section.

The nodal degrees of freedom are treated as unknowns. Therefore the potential energy Π_p is expressed in terms of nodal degrees of freedom. The steps that are necessary to derive the equilibrium equations are given below:

1. The body is divided into E finite elements
2. The displacement is approximated within an element e and is assumed as $U = N \cdot Q^{(e)}$ where $Q^{(e)}$ is the vector of nodal displacement degrees of freedom of the element e and N is the matrix of shape functions.
3. The characteristic stiffness matrices and the characteristic load vectors have to be derived with the usage of the principal of minimum potential energy. The potential energy functional of the entire body Π_p can be written as

$$\Pi_p = \sum_{e=1}^E \Pi_p^{(e)} \quad (2-42)$$

In this equation, $\Pi_p^{(e)}$ represents the potential energy of every element e . The potential energy of one element is given by applying Equation 2-41 and integrating over the volume $V^{(e)}$ and the surface $A^{(e)}$ of the element instead of the entire body.

$$\Pi_p = \frac{1}{2} \int_{V^{(e)}} \varepsilon^T D(\varepsilon - 2\varepsilon_0) dV - \int_{V^{(e)}} \phi^T U dV - \int_{A^{(e)}} \Phi^T dA \quad (2-43)$$

The vector of strains ε can be expressed in terms of the vector of nodal displacement $Q^{(e)}$ with $\varepsilon = B \cdot Q^{(e)}$ where the matrix B , which includes the partial derivatives, is the matrix

that leads to Equation 2-4 when multiplied with the displacement vector $Q^{(e)}$. With this relationship, the stresses can also be expressed as

$$\sigma = D(\varepsilon - \varepsilon_0) = DBQ^{(e)} - D\varepsilon_0 \quad (2-44)$$

From this, the potential energy of one element can be written as:

$$\Pi_p^{(e)} = \frac{1}{2} \int_{V^{(e)}} Q^{(e)T} B^T DBQ^{(e)} dV - \int_{V^{(e)}} Q^{(e)T} B^T D\varepsilon_0 dV - \int_{A^{(e)}} Q^{(e)T} N^T \Phi dA - \int_{V^{(e)}} Q^{(e)T} N^T \phi dV \quad (2-45)$$

In general, there will be some external concentrated forces acting at the nodes. Including the vector of nodal forces \tilde{P}_c , which is acting in the same directions as the nodal displacement vector \tilde{Q} , the total potential energy of the structure is:

$$\Pi_p = \sum_{e=1}^e \Pi_p^{(e)} - \tilde{Q}^T \cdot \tilde{P}_c \quad (2-46)$$

The summation of this equation implies the expansion of the element matrices to structure size followed by the summation of overlapping terms. The total potential energy of the structure is given by Equation 2-47. It expresses the energy in terms of the nodal degrees of freedom.

$$\Pi_p = \frac{1}{2} \tilde{Q}^T \left[\sum_{e=1}^E \int_{V^{(e)}} B^T DB dV \right] \tilde{Q} - \tilde{Q}^T \sum_{e=1}^E \left(\int_{V^{(e)}} B^T D\varepsilon_0 dV + \int_{A^{(e)}} N^T \Phi dA + \int_{V^{(e)}} N^T \phi dV \right) - \tilde{Q}^T \tilde{P}_c \quad 2-47$$

To find the static equilibrium configuration of the structure, it is necessary to solve the conditions for the minimization of the potential energy, which can be expressed by

$$\frac{\partial \Pi_p}{\partial \tilde{Q}} = 0.$$

The equation can then be written as:

$$\sum_{e=1}^E \int_{V^{(e)}} B^T DB dV \cdot \tilde{Q} = \tilde{P}_c + \sum_{e=1}^E \left(\int_{V^{(e)}} B^T D\varepsilon_0 dV + \int_{A^{(e)}} N^T \Phi dA + \int_{V^{(e)}} N^T \phi dV \right) \quad (2-48)$$

$$\sum_{e=1}^E K^{(e)} \cdot \tilde{Q} = \tilde{P}_c + \sum_{e=1}^E (P_i^{(e)} + P_s^{(e)} + P_b^{(e)}) = \tilde{P} \quad (2-49)$$

where $K^{(e)}$ represents the element stiffness matrix, $P_i^{(e)}$ is the element load vector due to initial strain, $P_s^{(e)}$ is the element vector due to surface forces and $P_b^{(e)}$ represents the element load due to body forces.

4. The desired equilibrium equation of the overall structure can now be expressed as

$$\tilde{K} \cdot \tilde{Q} = \tilde{P} \quad (2-50)$$

where \tilde{K} is the global stiffness matrix and \tilde{P} represents the global nodal load vector.

5. The required solutions for element stresses and nodal displacement can be found by solving Equation 2-50. As described in Section 2.3.2 when solving this equation, the boundary conditions have to be integrated into the calculation.

2.3.4 Usage and application of the FEM

The usage and application of the FEM typically occurs in three stages:

Pre-processing:

In pre-processing, the overall geometry of the model is created. The material properties are assigned to the different sections of the model as well as the boundary conditions and the applied load. Additionally, the finite element mesh is created, which gives the nodes and elements of the model. For complex models, automatic mesh generation is used for efficient discretization. When creating an input file with Patran, it is necessary to idealize the structure and the load case in order to create a simple model. After the geometry is fixed and generated, the mesh is created by choosing appropriate elements for the given problem. Elements are distinguished by different characteristics, for example their shape and the number of dimensions. The creation of a loading condition and the determination of the output variables are also part of pre-processing.

The software to create the nodes and the elements for the models that were used in this work was MSC.Patran (Patran). Prior to analysis, the program writes out a so called ABAQUA input file which includes all of the pre-processing input data described earlier. Although it was possible to create the complete input file with Patran and to run the whole solving process with Patran, in this work Patran was used only to create the nodes, elements and groups of the model. While the nodes, elements and groups of a model were written into an input file, the loads, boundary conditions as well as the material properties and the applied loads were entered directly into the input file.

Analysis:

This process is also called solving. In this step, the actual calculation of the problem takes place. This means that the unknown variables are computed. Most of the analyses were performed by the FEM software ABAQUS/Standard version 6.5-1 (ABAQUS). For several jobs the ABAQUS/Standard version 6.4-5 was used. These tools can be used for a wide range of problems, for example linear and nonlinear problems, static and dynamic as well as thermodynamic behavior. In this work, they were used to perform nonlinear analyses. ABAQUS uses the Newton-Raphson method to solve nonlinear problems. This method is explained more thoroughly in Section 2.3.5. The analyses were displacement-controlled and it was assumed that the behavior of the materials used was linear elastic up to the point of failure.

Post-processing:

Post-processing includes visualization of the results that were calculated by the solver. This process includes for example the visualization of deformed and undeformed shapes, stresses, strains and the other variables requested in the output data. For post-processing the ABAQUS/Viewer software was used. This allows the user to evaluate the calculated results. As mentioned earlier it was possible to visualize the stresses, strains and displacements and numerous other variables.

Modeling of composites in ABAQUS:

In ABAQUS, there are three different methods available for the modeling of composite structures.

a. Microscopic modeling:

In this method the fiber and the matrix are modeled separately. This means that they are seen as independent deformable continua.

b. Discrete reinforcement modeling:

The fibers are modeled with discrete elements for example bars and the matrix is modeled as a continuum.

c. Macroscopic modeling:

Here the composite is modeled as a single material that might be orthotropic or anisotropic with regard to its material behavior.

In this work, only the third approach, macroscopic modeling, was used to investigate the structural performance of the composites. There were different elements used in order to simulate the structural behavior. For the modeling of the composite, the S4R element of ABAQUS was used in this work. The S4R is a shell element with four nodes and one integration point. The nodes are located on the corners of each element. Therefore these elements use linear interpolation in each direction. The R represents “reduced integration”. ABAQUS uses numerical techniques to integrate various quantities over the volume of each element. The material response is evaluated by ABAQUS at each integration point of each element. The choice of full or reduced integration can have significant effect on the accuracy of the element for the given problem. For these shell elements the classical laminate theory, which was described in Section 2-1, is valid.

The composite layers were created with the “*SHELL SECTION” command. The fiber orientation was specified with respect to the global coordinate system. The fiber orientation was defined in accordance to the conventions declared in [1]. For the shell elements used, no through-thickness stresses were calculated. This reduced the computational time for the analysis but no peel stresses or out-of-plane stresses could be calculated within the composite.

The other type of element used in this work was the solid element C3D8. Solid elements are capable of reproducing the stress states in all directions. The C3D8 element has eight nodes, which are located at the corners of the element. They also have eight integration points as well as linear integration.

Nonlinear analysis in ABAQUS [1]:

In a finite element analysis it is possible to distinguish three types of nonlinearity.

- Geometric nonlinearity:

This form of nonlinearity plays an important role when an analysis is considered to have large displacements or rotations, large strains or structural instabilities. The principal goal is the prediction of the equilibrium configuration that the body will adopt under a particular loading.

- Boundary nonlinearity:

The reasons for this form of nonlinearity are mainly contact problems.

- Material nonlinearity:

This form of nonlinearity depends on the material behavior. In ABAQUS, there are numerous models offered to simulate nonlinear material behavior. They are mostly history dependent, which means that the response of the material depends on what happened to it at previous times

Normally these nonlinearities act simultaneously. In the actual analysis it is possible to include only certain types of nonlinearity based on the predominate effects.

2.3.5 The Newton-Raphson method

Classic Newton-Raphson method:

As mentioned earlier in this section, ABAQUS uses the Newton-Raphson method to solve nonlinear problems iteratively. Figure 2-12 shows an example of a nonlinear load-displacement curve.

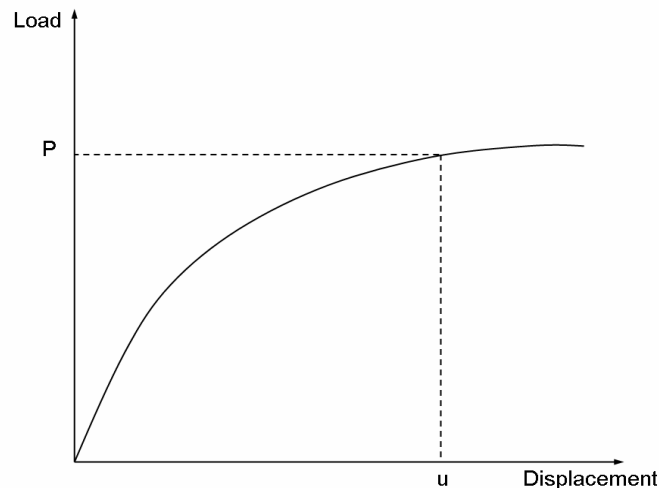


Figure 2-12 Nonlinear load-displacement curve [1]

The goal of a nonlinear analysis is to determine the response shown in Figure 2-12. In contrast to linear analyses, in nonlinear analyses it is not possible to calculate the solution by solving a single system of linear equations. Basically, the simulation consists of one or more steps. A step consists of an analysis procedure option, loading options and output request options. In nonlinear analyses each step is broken into increments. This makes it possible to follow the nonlinear solution path. Within the increment, an iteration is an attempt to find an equilibrium solution. If the model is not in equilibrium at the end of the iteration, ABAQUS tries another iteration, so that at the end of each increment the structure is in approximate equilibrium. If the iteration process continually diverges, so that subsequent iterations move further away from the equilibrium state, the iteration process is terminated by ABAQUS/Standard automatically. In this case ABAQUS restarts the increment with a reduced increment size. This procedure is called “cut-back”.

When a body is in equilibrium, the external forces P and the internal forces I must balance each other:

$$P - I = 0 \quad (2-51)$$

The internal forces are caused by the stresses in the element, which are attached to the corresponding nodes. P is the external load. The nonlinear response to this load increment is shown in Figure 2-13.

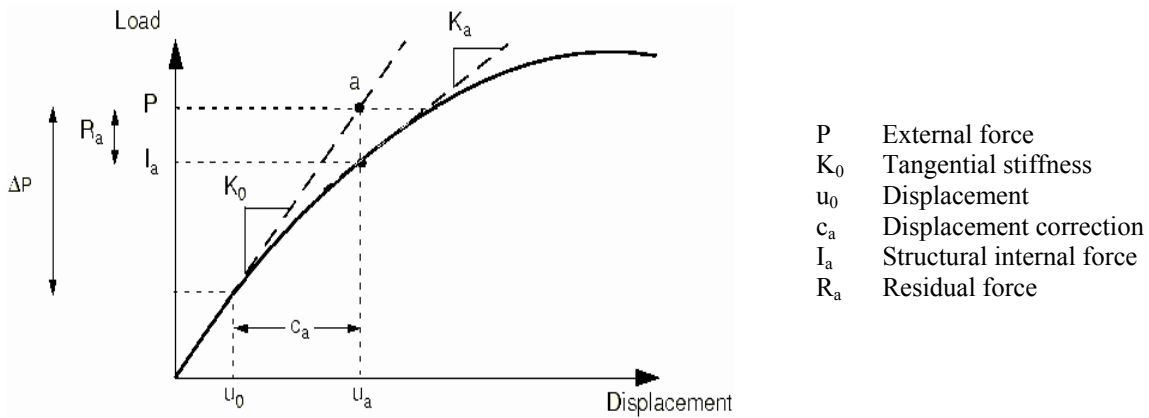


Figure 2-13 First iteration in an increment of ABAQUS [1]

The stiffness matrix of the structure, K_0 , which is based on its configuration at the displacement u_0 , and the load increment ΔP , is used by ABAQUS to calculate the displacement correction c_a . Using this correction, the structure's configuration is updated to u_a , the total displacement in the increment. The internal force I_a is then calculated in this updated configuration. With this it is possible to calculate the difference between the total load and the internal load I_a .

$$R_a = P - I_a \quad (2-52)$$

In this equation, R_a is the residual force for the iteration. If R_a is zero at every degree of freedom (DOF), point a in Figure 2-13 would lie on the load-deflection curve. This means that the external and internal forces would balance each other and the structure would be in equilibrium. This is never the case when solving nonlinear problems. To be able to find a solution ABAQUS compares the value of R_a to a tolerance value, which is called $R_{a, tolerance}$. As long as R_a is not less than $R_{a, tolerance}$ at all nodes the solution will not be accepted by ABAQUS. Additionally to this criterion, ABAQUS checks if the last displacement correction c_a is small in comparison to the total increment displacement $\Delta u_a = u_a - u_0$. In the case that c_a is greater than a defined fraction of the total increment displacement u_a , another iteration is performed by ABAQUS. When the two criteria are satisfied, the solution is converged for the increment and is accepted by ABAQUS.

If no equilibrium solution can be reached, ABAQUS starts another iteration in order to bring the internal and external forces in balance. This iteration is shown in Figure 2-14.

The new stiffness matrix K_a is calculated. This is based on the current displacement u_a . ABAQUS uses the new stiffness and the residual force R_a to calculate a new displacement c_b . This displacement brings the system closer to equilibrium (point b in Figure 2-14). After that, a new residual force R_b is derived, which leads to a new structure configuration u_b . As in the last iteration, the residual force R_b is compared to the force residual tolerance and ABAQUS also checks the displacement control in which the new displacement c_b is compared to the increment of displacement, Δu_b . When the criteria are not satisfied, ABAQUS will perform further iterations.

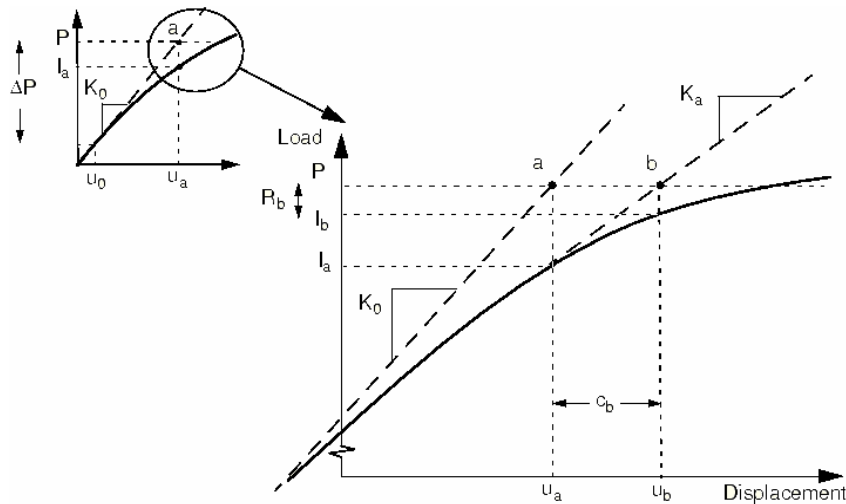


Figure 2-14 Second iteration in an increment of ABAQUS [1]

In nonlinear problems the stiffness matrix of the model is computed and the entire system of equations is solved. This effort can be very time consuming for a large number of elements, especially when the increment size is small and a lot of cut-backs are allowed. Different solvers apply different methods to solve problems that include nonlinearity. ABAQUS automatically adjusts the size of the increment in order to solve nonlinear problems efficiently. The user only needs to suggest the size of the first increment.

The Newton-Raphson method with artificial damping [1]:

It is possible that nonlinear static problems are unstable. Such instabilities may be of geometrical nature, for example buckling problems. They might also be caused by material behavior such as material softening or degradation. If the instability is localized, strain energy will be carried over from one part of the model to the adjoining elements. Therefore global solution methods may not work. In this case, the problem has to be solved dynamically or with the aid of artificial damping.

In ABAQUS, a mechanism for stabilizing these kinds of problems is provided. This mechanism is triggered by the STABILIZE parameter on nonlinear quasi-static procedures.

$$F_v = c \cdot M^* \cdot v \tag{2-53}$$

In this equation, F_v represents the viscous force, which is added to the global equilibrium equation.

$$P - I_a - F_v = 0 \quad \text{with } v = \frac{\Delta u}{\Delta t} \tag{2-54}$$

M^* represents the artificial mass matrix calculated with the unit density. c is the damping factor (DF) and v is the vector of nodal velocities. Δt is the time increment, though this does not necessarily have a physical meaning in the context of the problem.

It is assumed that the problem is stable at the beginning of the step. This means that instabilities occur during the step. As long as the model is stable, the viscous forces and therefore the viscous energy dissipated are very small. In this case, the artificial damping factor does not affect the analysis. If a local region loses its stability, the local velocities

increase and part of the strain energy, which is released is dissipated by the applied artificial damping. ABAQUS calculates and prints the damping factor c to the message file. Its values are based on the solution of the first increment. In most cases however, the first increment of the step is stable even without the application of artificial damping. When this is the case, the damping factor is determined in such a way that the extrapolated dissipated energy for the step is a small fraction of the extrapolated strain energy. This fraction is called the dissipated energy fraction. Its default value is set to 2.0×10^{-4} by ABAQUS/Standard automatically. It can also be changed by the user by assigning the needed value to the STABILIZE parameter in the input file.

3. User subroutines- Simulation of skin-stringer debonding

3.1 General overview

User subroutines provide an extremely powerful and flexible tool for analysis. They are provided to increase the functionality of different ABAQUS options for which the common data line usage alone may be too restrictive. The user subroutines in ABAQUS are normally written in the FORTRAN programming language. They must be included in a model when the analysis is executed. It is possible to include more than one subroutine in the analysis of one model but they cannot be called from one another. It is also possible to call utility routines that are provided by ABAQUS. In this work, the user subroutines are used to simulate the material behavior of the adhesive layer.

It was necessary to develop different user subroutines for several reasons. The main reason was to be able to predict the collapse load of a composite panel structure more accurately than it was possible with the ordinary version of ABAQUS. With the developed subroutines it was possible to simulate the degradation within the adhesive, which connects stringer and skin of the panel, in a more realistic way.

Three different subroutines were developed in [17], which differ in their numerical approach and level of accuracy. These three user subroutines will be described in a more detailed way in the following chapter. The subroutines influence the analysis by changing the material properties if required. Therefore they affect the stiffness matrix of the model directly. In the first iteration of an increment all of the user subroutines are called twice for each integration point. In the first call of the user subroutines, the original stiffness matrix is calculated by using the configuration of the model at the beginning of the increment. When the subroutine is called for the second time, the new stiffness matrix, which is based on the updated configuration of the model, is created. In the following iterations, the corrections of the model set-up are calculated with the new stiffness from the end of the previous iteration.

The first subroutine that is described is the User Defined Field (USDFLD). This routine calls the stresses from ABAQUS. It is used to redefine so called field variables at a material point. The field variables are used to change the material properties at the material point. No calculations including the stresses or stiffness are made in this routine.

The next two user subroutines are versions of the so called User Material (UMAT), one working explicitly and the other working implicitly. These routines are also used to change material properties according to exceeded failure criteria but these subroutines also include calculations involving the stiffness and the stresses in contrast to the USDFLD.

3.2 The user subroutine USDFLD (User Defined Field)

3.2.1 Data flow of the USDFLD

This user subroutine is used to redefine field variables at a material point. The routine allows the user to define field variables at a material point as functions of any material point quantities.

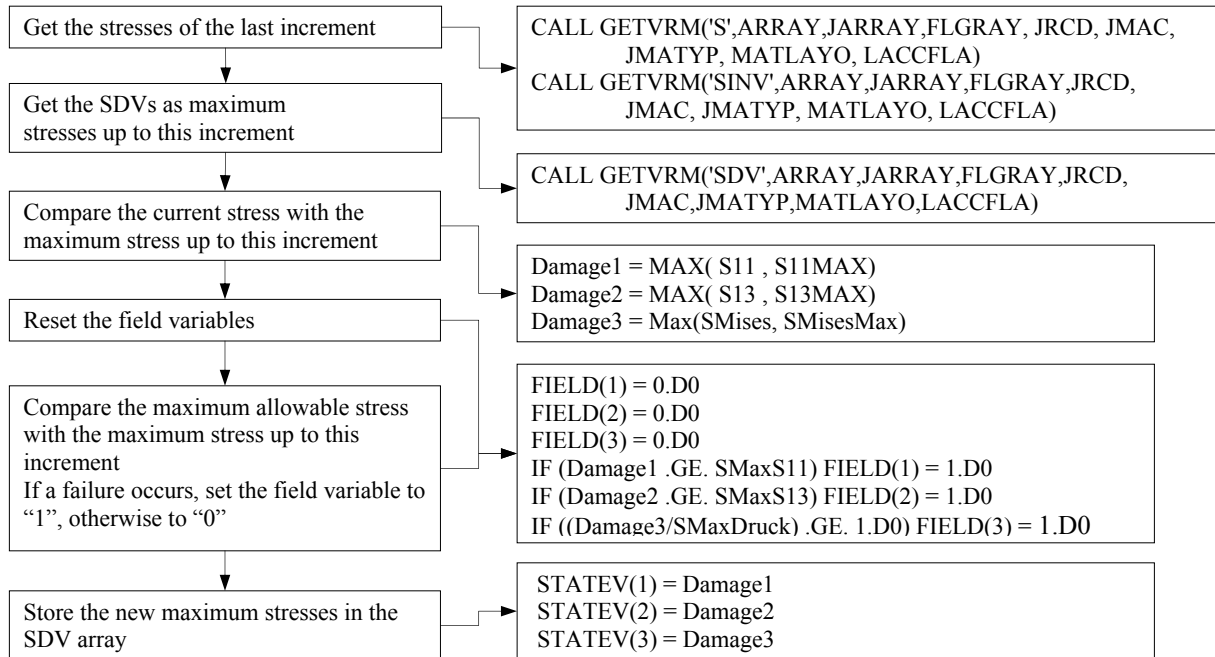


Figure 3-1 Data flow of the USDFLD [17]

In this work, this routine was used to compare current stresses with the maximum allowable stresses. This means, that the concept of the routine is to compare the stresses of the analyses state with the maximum allowable stresses and predict a failure of the material at the integration point when the maximum allowable stresses are exceeded. The information on failure occurrence can be passed to ABAQUS via the field variables (FV), and the material properties are changed with the new values defined in the input file.

The stresses are read in from the last increment. The reason for this is that the subroutine is called at the beginning of an increment, where no current results for the stresses of the active increment exist. The stresses of the last increment are called and afterwards compared to the maximum stress up to the current increment. This is done to prevent a healing mechanism. The field variables are set to one in case that failure occurs. If that happens, the modulus of the material is reduced, which causes a reduction of the stresses as well. Therefore in the next increment, this material point would probably not fail again and the field variable could be set back to zero. This healing mechanism is physically impossible.

Therefore the maximum stresses up to the current increment are stored in the solution dependent state variables (SDV) and compared to the current stresses. SDVs are parameters that can be called in the running subroutine. If the stresses stored in the SDVs are higher than the stresses of the current increment, they are taken as the relevant stresses to be compared to the maximum allowable stresses. Therefore the element will fail again and the corresponding field variable stays at one. When the failure of a material point is predicted in an element, the new maximum stresses are stored in the SDVs.

From Figure 3-1 it can be concluded that three different stresses were taken into consideration for the prediction of failure, S11 (normal stress perpendicular to the adhesive layer), S13 (shear stress acting on the same face in the axial direction of the panel) and SMises (von Mises stress). The first two stresses were chosen from the six possible stresses because they were assumed to be the most critical values for the prediction of failure. The von Mises stress as a comparison stress is a typical and frequently used failure criterion.

3.2.2 Definition of the material properties and the FVs

The updated material properties that ABAQUS uses to calculate the new stiffness and stresses are given in the input file. Here it has to be identified which material is used and at which combination of field variables are redefined with new values. The field variables work as a simple switch for the material properties. Figure 3-2 shows the declaration of the material properties in the input file. This figure shows the case that the three failure criteria defined, for example S11, S13 and SMises as shown in Figure 3-1, are actually used in the routine.

```

**Material in MPa
*MATERIAL, NAME=MAT_ADHESIVE
*ELASTIC, TYPE=ISOTROPIC, DEPENDENCIES=3
3000.0    0.4,  0.0  0.0,  0.0,  0.0
30.0     0.4,  0.0  1.0,  0.0,  0.0
30.0     0.4,  0.0  0.0,  1.0,  0.0
30.0     0.4,  0.0  0.0,  0.0,  1.0
30.0     0.4,  0.0  0.0,  1.0,  1.0
30.0     0.4,  0.0  0.0,  1.0,  1.0
30.0     0.4,  0.0  1.0,  0.0,  1.0
30.0     0.4,  0.0  1.0,  1.0,  1.0
*USER DEFINED FIELD
*DEPVAR
3
    
```

Figure 3-2 Declaration of the material properties in the input file

The first line gives the name of the material. In the next line, the material option is initiated. In this case, an elastic and isotropic material was used. The dependencies given in the same line represent the number of field variables used. The first value of the following data line is the Young's modulus, the second value represents the Poisson's ratio and the third value is the thermal expansion ratio. The next three variables are the FVs. The first data line gives the material properties in case that no failure occurs. The following lines give the new material properties in dependence of the combination of the field variables. The number of solution dependent state variables is defined with the *DEPVAR function. As mentioned before the SDVs are used to store the maximum value of the comparison of the stresses up to the current increment with the current stresses. These values are called the damage values in the subroutine and are given to the SDVs at the end of each subroutine run. Therefore the SDVs carry the maximum stress that has been predicted at the corresponding material point, even if the stresses are reduced due to the reduction of the material properties. The SDVs are updated only once at the end of the increment so that the stored values are from a converged solution.

3.3 The user subroutine UMAT explicit (User MATerial)

The UMAT is called at all material calculation points of elements for which the material definition includes the *USER MATERIAL option in the input file. It can be used to define the mechanical constitutive behavior of a material. It has a wide field of appliance because it can be used with any procedure that includes mechanical behavior.

The UMAT explicit is based on the concept of the USDFLD. It was developed to be less increment size dependent during the analysis and to derive the failure propagation more precisely. In the subroutine used by the DLR the failure state is calculated from the stresses of the previous increment just as in the USDFLD. This is the reason why this subroutine is called “explicit”. Stresses are taken directly from the previous increment. The programming of the failure prediction is also very similar to the USDFLD, although the UMAT explicit uses only solution dependent state variables instead of field variables.

3.3.1 Data flow of the UMAT

Figure 3-3 shows the basic data flow of the UMAT explicit. It is obvious that the flow is very similar to the flow of the USDFLD shown in Figure 3-1. When the subroutine is started, it calls the stresses of the last increment. Afterwards the maximum stresses up to the increment are called, which are stored in the SDVs. The stresses are compared and the higher value is stored as the damage value. Then the damage values are compared to the maximum allowable stresses of the material. If a failure criterion is exceeded, the Young’s modulus is reduced according to the material properties defined in the input file. The new maximum stresses are stored in the solution dependent state variables. As mentioned earlier in the description of the USDFLD, this is necessary to prevent a healing mechanism. If the Young’s modulus was changed, in addition to the stresses, the stiffness also have to be updated. After the stresses are calculated, the subroutine is closed and ABAQUS continues with the analysis.

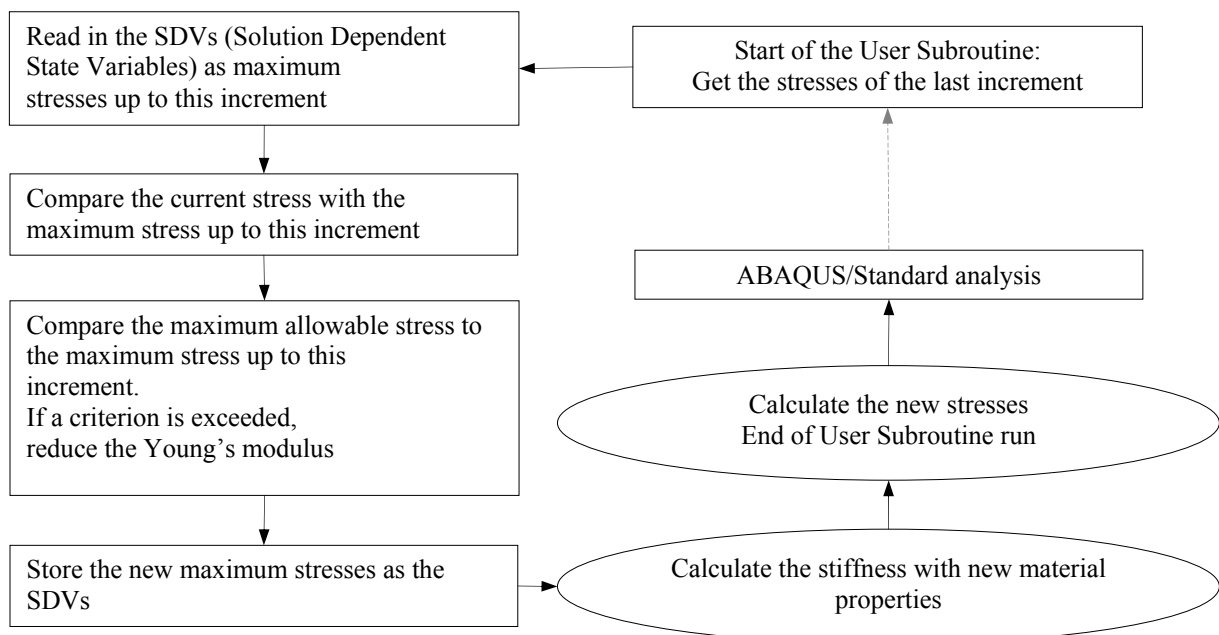


Figure 3-3 Data flow of the UMAT explicit [17]

3.3.2 Definition of the material properties and the SDVs

As in the USDFLD, the required material properties after the occurrence of failure are defined in the ABAQUS input file. The UMAT uses the *USER MATERIAL option to provide the values of the material properties in the input file. The failure stresses are also programmed in the input file. This is a major difference to the USDFLD where the failure stresses have to be written into the subroutine directly. The declaration of the variables is shown in Figure 3-4.

```
*User material, Constants=9
3.0E3, 30.00, 30.00, 30.00, 30.00 , 0.4 ,8.00 ,38.00,
48.00
*DEPVAR
7,
```

Figure 3-4 Declaration of the material properties in the input file

The number of constants used is nine. Every constant stands for a material property. The first value is the Young's modulus without any degradation. The following four constants describe the material properties in case that the different failure criteria are exceeded. The sixth value is the Poisson's value. In this example the last three constants are the failure stresses of the material in MPa that are used to predict the onset of failure. These values are all used as PROPS() values in the UMAT. A more detailed description can be found in Figure 3-5. The order of the values is dependent on the programmed subroutine. Therefore the SDVs have to be defined in accordance with the order of the properties of the material. The first three values are used to store the damage values of the running increment. The following three values (SDVs 4 to 6) are used as switches to initiate the corresponding failure criterion and to reduce the Young's modulus according to the exceeded criterion. The last variable SDV 7 is used to store the new Young's modulus.

```
PROPS(1) - E without degradation
PROPS(2) - E at S11 >= SMaxS11 (mechanism 1)
PROPS(3) - E at S13 >= SMaxS13 (mechanism 2)
PROPS(4) - E at SMises/SMaxDruck >= 1.0 (mechanism 3)
PROPS(5) - E at S11>= SMaxS11,S13>= SMaxS13
and SMises/SMaxDruck>= 1.0s
PROPS(6) - NU
PROPS(7) - SMaxS11
PROPS(8) - SMaxS13
PROPS(9) - SmaxDruck
STATEV(1) -Damage1
STATEV(2) -Damage2
STATEV(3) -Damage3
STATEV(4) -0: mechanism 1 not active
1: mechanism 1 active
STATEV(5) -0: mechanism 2 not active
1: mechanism 2 active
STATEV(6) -0: mechanism 3 not active
1: mechanism 3 active
STATEV(7) -Young's modulus according to failure criteria
```

Figure 3-5 Declaration of material properties and SDVs

As described earlier, the current maximum stresses are detected and stored. The damage stresses are compared to the maximum allowable stresses. In case that the maximum

allowable stresses are exceeded, the so called failure identifiers IDF are set to one. Otherwise, they remain zero. The reduction of the material properties is very similar to the USDFLD, because the IDFs work as switches for the different mechanisms shown in Figure 3-5 as well. The IDFs are stored in the SDVs 4 to 6, while the damage stresses are stored in the SDVs 1 to 3.

3.3.3 Calculation of the stiffness and stresses

One of the main differences between the USDFLD and the UMAT is that in the UMAT subroutine, it is necessary to calculate the new stiffness matrix and subsequent new stresses after the material properties were changed in an increment. The material on which the subroutines were applied was assumed to be linear elastic. This is valid for small elastic strains. Hookes law of elasticity was used to calculate the relation between the stresses and the strain tensors.

$$\underline{\sigma}_i = D_{ij}^{el} \cdot \underline{\varepsilon}_j^{el} \quad (3-1)$$

In this equation σ_i is the total stress, D_{ij}^{el} represents the elasticity tensor and ε_j^{el} is the total elastic strain. In order to calculate the new stresses of the increment, the new elasticity tensor had to be derived.

Firstly, the elements of the elasticity tensor had to be calculated for the case of linear elasticity that was assumed for the material. Afterwards the stresses of the increment were calculated. Since linear elastic material behavior was assumed, which means that the material stays in the elastic part of the stress-strain graph, once the maximum allowable stress was exceeded, the Young's modulus was reduced. Then the stresses were decreased to a value under the critical value. The corresponding equation to calculate the stresses is:

$$\sigma_j = D_{ij} \cdot (\varepsilon_i + \Delta\varepsilon_i) \quad (3-2)$$

In this equation, ε_i is the strain up to the current increment, while $\Delta\varepsilon_i$ is the strain of the running increment. A more thorough description of the calculation of the stresses can be found in the Appendix and in [17].

3.4 The user subroutine UMAT implicit

The main difference between the UMAT explicit and implicit is that in the implicit version, the stresses of the current running increment are used to calculate the failure of the material. The stiffness matrix is also updated in every iteration, not only once per increment. This is the reason why this subroutine is called implicit, as it does not take the stress values from ABAQUS directly, but they are calculated within the subroutine. The code of the explicit and implicit version of the UMAT differs only in the calculation of the stiffness and the stresses at the beginning of the UMAT implicit.

3.4.1 Data flow of the UMAT implicit

As mentioned earlier the data flow is very similar to the flow of the UMAT explicit, but in the implicit version, the stresses at the beginning are not called from the pervious increment.

The new stress state is calculated based on the updated material properties. In Figure 3-6 the term “current” means the stresses or material properties at the present point in time at the beginning of each subroutine run. This subroutine uses the updated strain field to calculate the stresses of the iteration. The data flow of the UMAT implicit is shown in Figure 3-6.

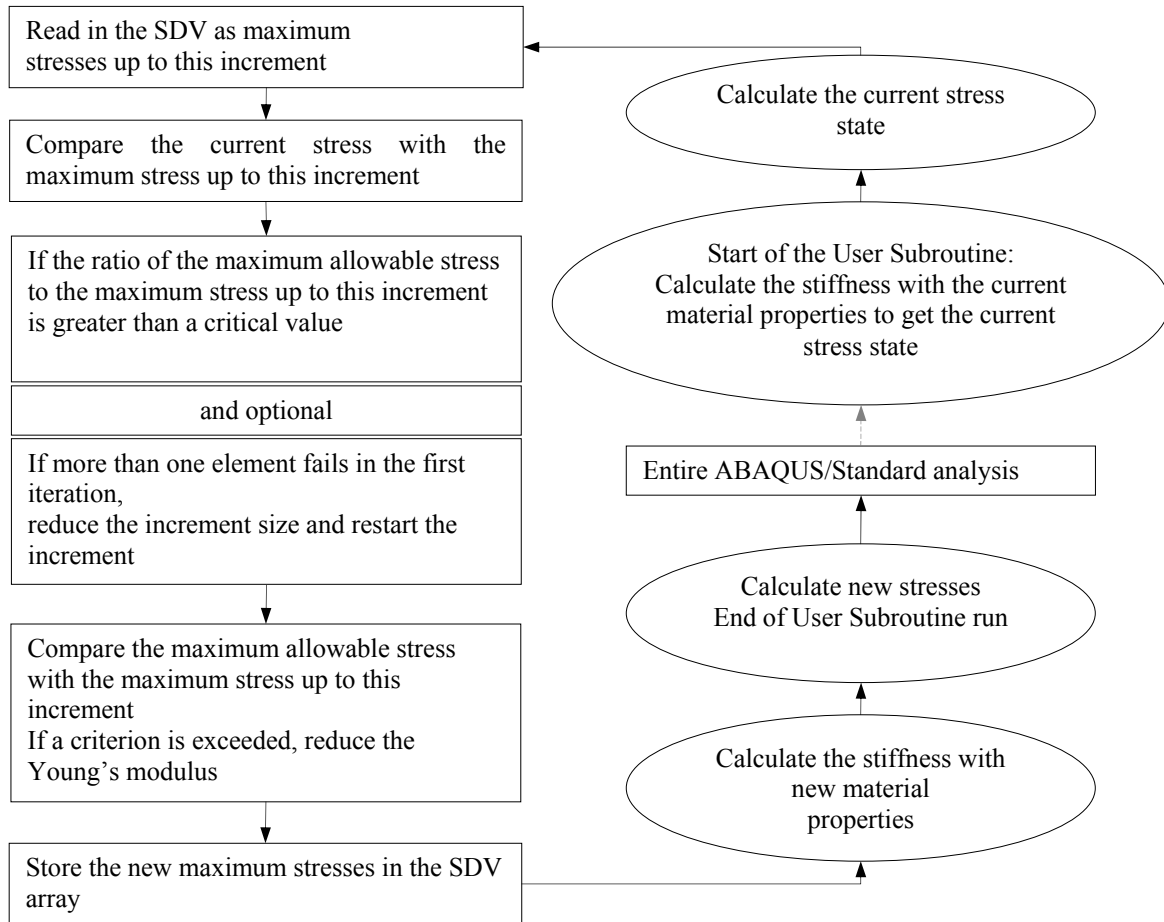


Figure 3-6 Data flow of the UMAT implicit [17]

3.4.2 Problems of numerical instability and their solutions

Another main difference between the UMAT implicit and the other subroutines introduced in this chapter is the problem of numerical instability. The standard version of the UMAT implicit broke down frequently at an early stage of the analysis, because too many elements were failing in one increment. Therefore the material properties had to be changed at too many integration points at the same time. To prevent this problem, a version of the UMAT was developed that provided several ways to control the increment size because it was assumed that numerical stability can be achieved by reducing the size of the increment, which leads to a reduced number of failing elements. The subroutine counts the number of failing elements and continually reduces the increment size until no more than a specified number of elements, in this case one, failed during the first iteration. Therefore this subroutine is increment size independent as opposed to the UMAT explicit and the USDFLD.

The subroutine checks the stress ratio between the maximal allowable stress and the current stress of the analyzed material point. In case that this ratio is greater than a defined critical

value, the increment is restarted with a smaller load step. This function is called stress ratio control and is discussed more thoroughly in Chapter 5 of this work.

Optionally, it is possible for the subroutine to check if the number of elements failing in the first iteration is higher than the number specified in the routine. If the number is exceeded, the increment will be restarted. This function is called the “one element failure control” and is discussed more thoroughly in Chapter 5.

After the two criteria are passed, the subroutine compares the stresses of the increment with the maximum stresses up to this increment and stores the higher value in the SDVs. This is to prevent the healing mechanism described earlier in this work. Afterwards, the maximum stresses are compared to the maximum allowable values. If any failure is predicted, the subroutine reduces the Young’s modulus. The new stiffness and stresses are calculated as described in Section 3.3.3. Their new values are then passed on to ABAQUS.

3.5 Comparison of the subroutines

The following brief comparison of the three user subroutines is based on the results stated in [17].

USDFLD:

This is the most simple subroutine of the three routines used in this work that can be included into a model. The failure stresses are defined in the header of the subroutine itself and therefore they can be changed directly in the program itself. The new material properties have to be defined in the input file by the declaration of different combination of failure criteria as shown by Figure 3-2. The USDFLD is a usable subroutine for simple material models and when this subroutine is included, the probability to experience numerical problems is very low.

Concerning the analysis time, the USDFLD has been the fastest tool to receive results. Additionally, the subroutine did not cause numerical instabilities. As the stiffness and the stresses are not updated during the run of the routine, ABAQUS always finds a solution when the USDFLD is included.

When comparing the results of the analyses in which the subroutines were included, the results of the USDFLD are very similar to the results of the more time consuming subroutines. Therefore the USDFLD can be recommended to receive quick average results for analyses with small increment size.

A disadvantage of the USDFLD is that the definition of the failure stresses has to be done in the subroutine directly, not in the subroutine itself. Also this routine is only able to include very simple failure criteria into the simulation by using the FV’s as a simple switch. The potential of the routine to include more complex degradation models is very low.

UMAT:

The UMAT routines are more challenging than the USDFLD because the stresses and stiffness are calculated during the run of the subroutine. In contrast to the USDFLD it is not necessary to change any parameters of the subroutine itself because all material properties

before and after failure is experienced are defined in the input file using the *USER MATERIAL command.

The use and the set up of the UMAT implicit requires the same skills as the UMAT explicit but in the implicit version, the stress ratio of the maximum allowable stress and the current stress of the material point has to be declared because it is used to steer the increment size. Also, the switch to decide whether to run the standard or the advanced version of the UMAT implicit has to be set in the code of the subroutine.

The usability of the UMAT explicit is similar to the USDFLD. The analysis results calculated by this version of the UMAT and the USDFLD were very similar and the computation time was also similar to the USDFLD. Also this subroutine should be used for models with small increments.

The UMAT implicit standard is more time consuming than the USDFLD and the UMAT explicit but was also considered more accurate than these two subroutines. In conclusion, this subroutine represents a good compromise between analysis time and accuracy of the results if no numerical instabilities are experienced.

The version of the subroutines that was considered the most accurate by [17] was the UMAT implicit advanced. This assumption was based on the integration of several complex tools to steer the increment size in order to give a realistic prediction of failure behavior. The main disadvantage of this subroutine is that the time consumption is very high in comparison to the other routines but the advantage is that it is independent of the increment size and more flexible in terms of numerical stability.

4. Description of the simulation model

4.1 Description of panel geometry

In this section a brief introduction to the panel used in the COCOMAT project is given. The geometry of the panel used for the simulation and the experimental testing was based on the 15th variation of a panel that was used in the POSICOSS project and was therefore termed V15. In this work, there were two other names used for the panel. The geometry was the same for all these panels. P23 was the name of the panel that was used for the experimental testing. The simplified model used for the simulations in ABAQUS as described in Section 4-3 was termed Design1 (D1). The geometry of the COCOMAT panel consisted of a CFRP skin stiffened by five CFRP stringers. The panel is shown in Figure 4-1.

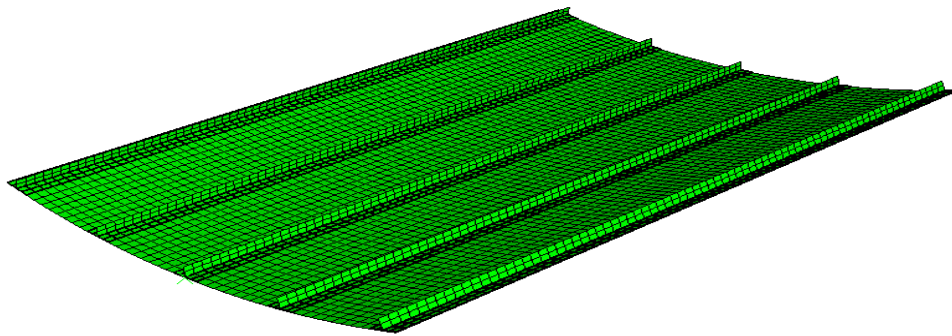


Figure 4-1 Geometry of the panel V15

At both ends of the geometry the last 60 mm were encased in resin while the left and the right edges of the panel were free. Figure 4-2 gives an overview of the applied boundary conditions of the model.

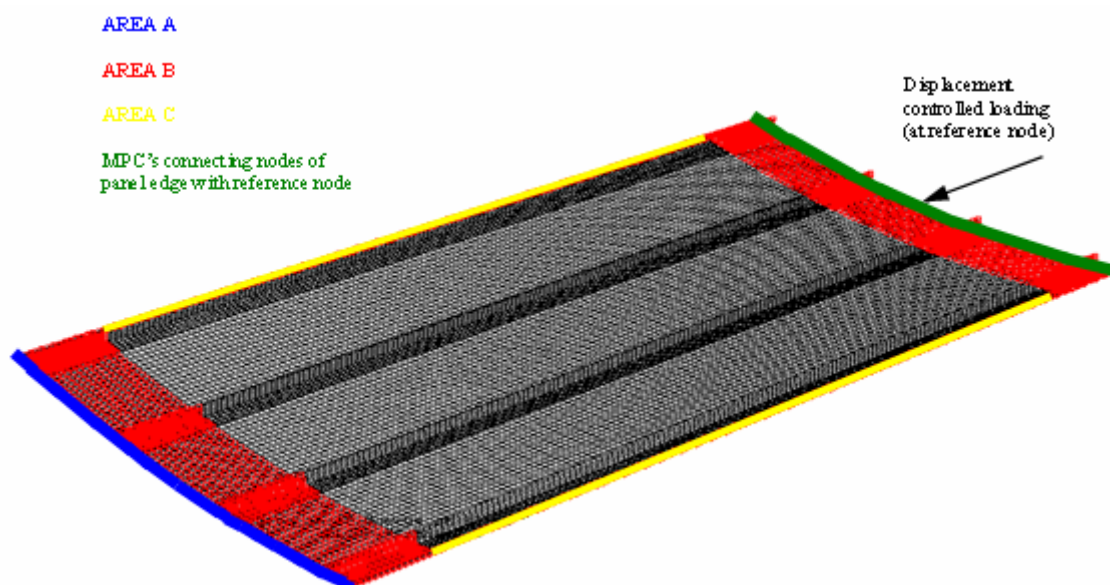


Figure 4-2 Panel with applied boundary conditions [10]

The encased ends are shown in red (AREA B), while the free edges on the right and left side are shown in yellow (AREA C). This was one of the main differences between the POSICOSS and the COCOMAT project because in the POSICOSS the edges were also restricted by boundary conditions.

The load was applied in displacement control. The displacement was applied at one node that was connected rigidly to the entire first row of nodes at the end of the panel. This is implied by the green right edge of the panel in Figure 4-2. The blue edge named AREA A, marks the fixed side of the panel. This side is not able to move during the simulation or the experiment. All six degrees of freedom are retained. It should be noted that the model shown in Figure 4-2 only has four stringers instead of the five stringers used in the COCOMAT project but the described boundary conditions are the same as the conditions used in COCOMAT.

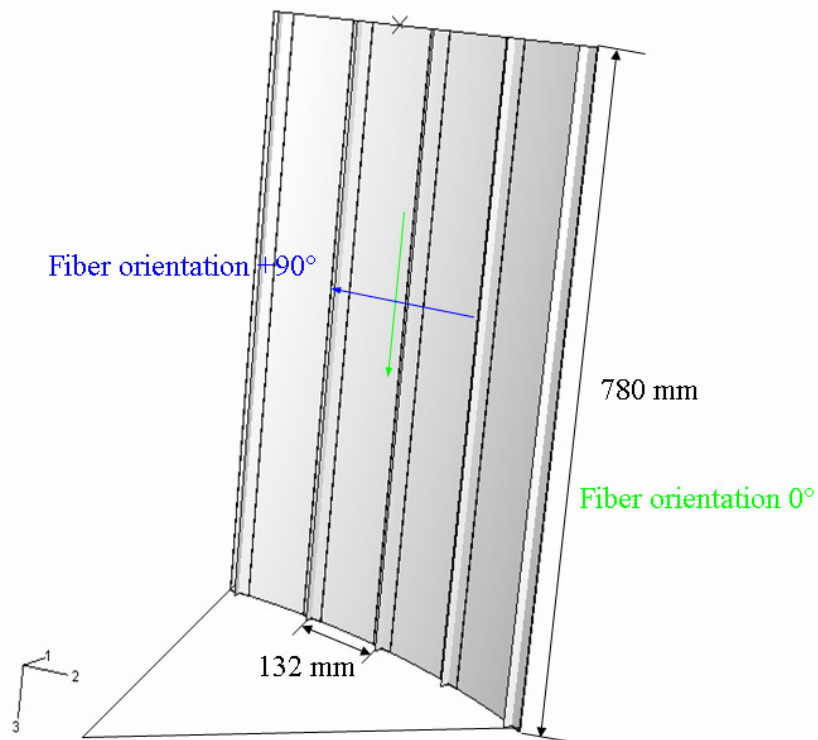


Figure 4-3 Panel geometry and fiber orientation [10]

Figure 4-3 shows the basic panel geometry with the reference coordinate system used in the analysis as well. The lay up of the stringer web $[(45,-45)_3, 0_6]_S$ is split in the center and bended normal (90°) with respect to the stringer blade to form the stringer flange.

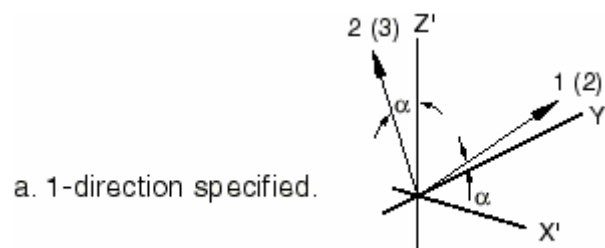


Figure 4-4 Definition of the coordinate system [1]

It is important to mention that for the “1-direction specified” in ABAQUS the fiber-direction 0° is in Y' -direction and not in Z' -direction. That means for the skin lay up the fiber

orientation definition is rotated by 90°. For the stringer blade the “2-direction specified” has been used in ABAQUS. A more detailed description of this specification can be found in [1]. The geometric data of the COCOMAT panel are displayed in Table 4-1.

Length of the panel	$l = 780 \text{ mm}$
Distance between the clamping	$l_f = 660 \text{ mm}$
Radius	$r = 1000 \text{ mm}$
Arc length	$a = 420 \text{ mm}$
Ply thickness of all CFRP layers	$t = 0.125 \text{ mm}$
Number of stringer	5
Thickness of the skin	1 mm
Lay up of the skin	$[90, +45, -45, 0]_s$
Lay up of the stringer web	$[(+45, -45)_3, 0_6]_s$
Lay up of the stringer flange	See Figure 4-5
Stringer height	14 mm
Stringer width	32 mm

Table 4-1 Geometric data of the COCOMAT panel

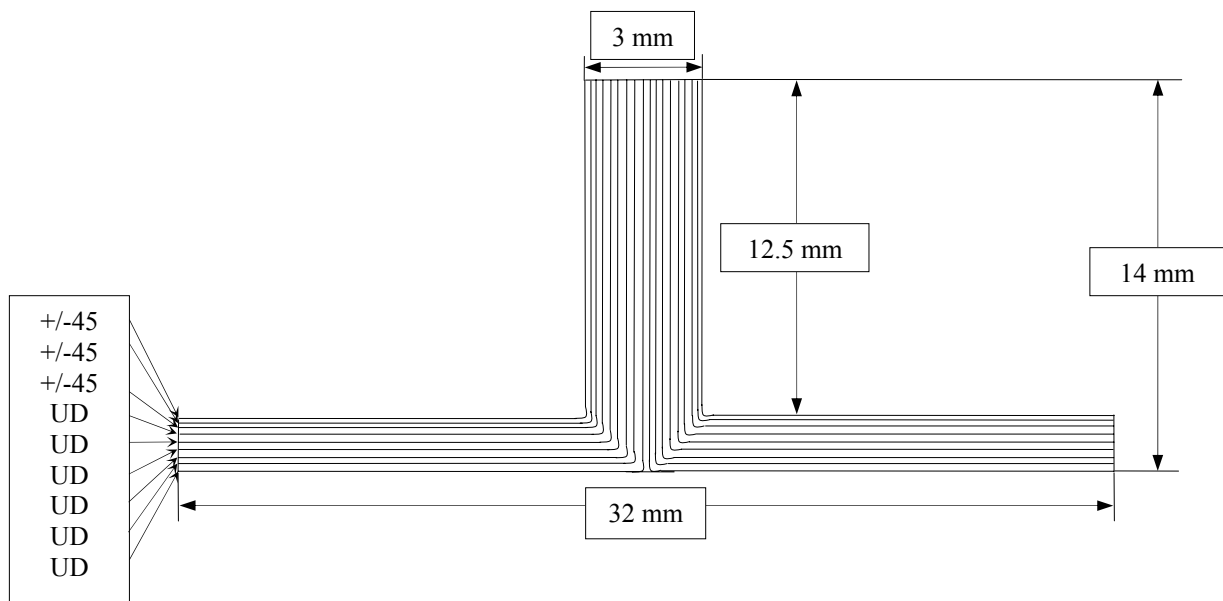


Figure 4-5 Model of the stringer used on the V15 panel

Figure 4-5 shows the lay up of the stringers. Only UD layers were used to model the stringer. The layers in the stringer web were positioned in +/-45° and 0° direction with a symmetric lay up. The lay up of the web was split into two parts and laid on each side of the web. Consequently the stringer flange consisted of half the number of layers as the web.

4.2 Introduction of materials as basis for the simulation model

Table 4-2 gives the material data of the adhesive layer. These data were taken from the product data sheet for Redux 312, an adhesive that is manufactured by Hexcel.

E_1 [MPa]	3000
ν_{12}	0.4
Max. compressive stress [MPa]	48
Max. shear stress [MPa]	38
Max. normal stress [MPa]	8.3

Table 4-2 Material of the adhesive layer-Redux 312 [8]

Based on the material data the Young's modulus was assumed to be 3000 MPa. In previous investigations [23] it was proven that the influence of the Young's modulus on the buckling behavior of a stiffened panel was small as an increase or reduction of the Young's modulus by 50% did not change the behavior significantly.

The material data of the CFRP material is given in Table 4-3. This material and the adhesive material were used in all models of this work. The inter-laminar shear strength given in the table is the strength of two plies that are loaded in shear against each other. The data of the CFRP material was taken from the product data sheet of the Hexply 8552. This material was also manufactured by Hexcel.

E_1 [GPa]	147
E_2 [GPa]	11.8
G_{12} [GPa]	6
G_{13} [GPa]	6
G_{23} [GPa]	4
ν_{12}	0.34
Tensile strength in fiber direction X_t [GPa]	2.715
Compressive strength in fiber direction X_c [GPa]	1.400
Tensile strength rectangular to the fiber direction Y_t [GPa]	0.056
Compressive strength rectangular to the fiber direction Y_c [GPa]	0.025
Shear strength [GPa]	0.101
Inter-laminar shear strength [GPa]	0.131

Table 4-3 Material of the plates: Prepreg IM7/8552 (Carbon/Epoxy) [8]

4.3 Modeling of the panel

The original version of the V1 panel was modeled with approximately 40,000 elements. This model was expected to be very time consuming, especially once the user subroutines were included in the analysis. In order to create a model that used fewer elements but still achieved similar results to the COCOMAT panel, parametric studies were performed in [17]. The entire model was assumed to have linear elastic material behavior, the only failure mechanism was implemented in the adhesive layer connecting the skin and the stringer.

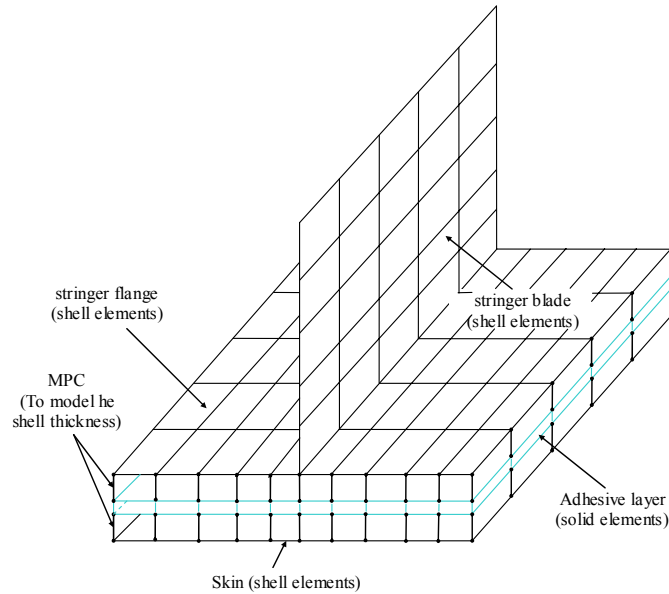


Figure 4-6 FE model of the skin-stringer connection

S4R were used as two dimensional shell elements to model the skin and the stringer. These elements consist of four integration points and four nodes. The adhesive layer was modeled with 3D solid elements (C3D8), a linear element with full integration. The SR4 and the C3D8 were previously described in Section 2.3.4. The adhesive layer was used to bond the skin to the stringer. The shell elements were arranged with the original distance of their thickness to the solid elements. This was done to ensure that it was not possible for the adhesive and the composite skin to penetrate each other. The solid elements of the adhesive were connected to the elements of stringer and the skin with multiple point constraints (MPCs). In this case, rigid link type MPCs were used to transfer all constraints from one node to the other. The lengths of the MPC links accounted for the fact that the nodes of the shell elements were situated on the mid-plane of the composite laminate, not on the edges. The FE model of the skin-stringer connection is shown in Figure 4-6. Note that this figure shows the mesh of the original simulation model V15. It used more elements in comparison to the simplified D1 model, namely 10 rows of elements instead of five rows in the stringer flange and five rows instead of two rows in the stringer blade. The mesh of the D1 model is shown in two dimensional view in Figure 4-7.

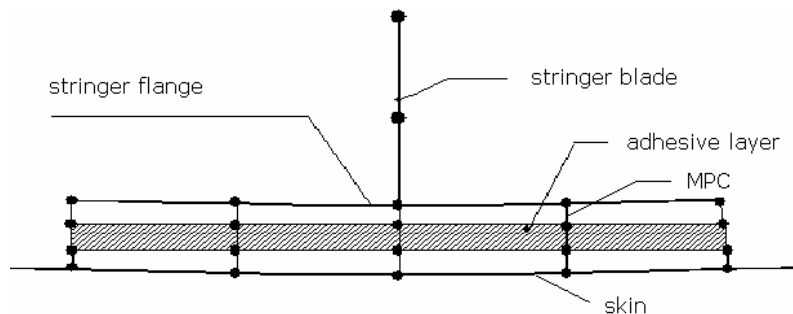


Figure 4-7 Mesh of the D1 model [17]

The model that was chosen for further investigations after performing a parametric study, which investigated the influence of the number of elements in the panel, was the D1 model. The results of the V15, termed Variation 1 in Figure 4-8, with the 40,000 elements (black curve) and the Design 1 model (red curve) with only 7,956 elements are shown in Figure 4-8.

The Variation 2 model that consisted of only 3,000 elements was also investigated. In this case the V15 panel (Variation 1) was the nominal or reference panel, while in the panels Design 1 and Variation 2 changes were included into the simulation models. As mentioned before, the geometry of the panels was kept the same, only the number of elements was varied in order to find a compromise between accuracy of the simulation model and the time consumption of the analysis.

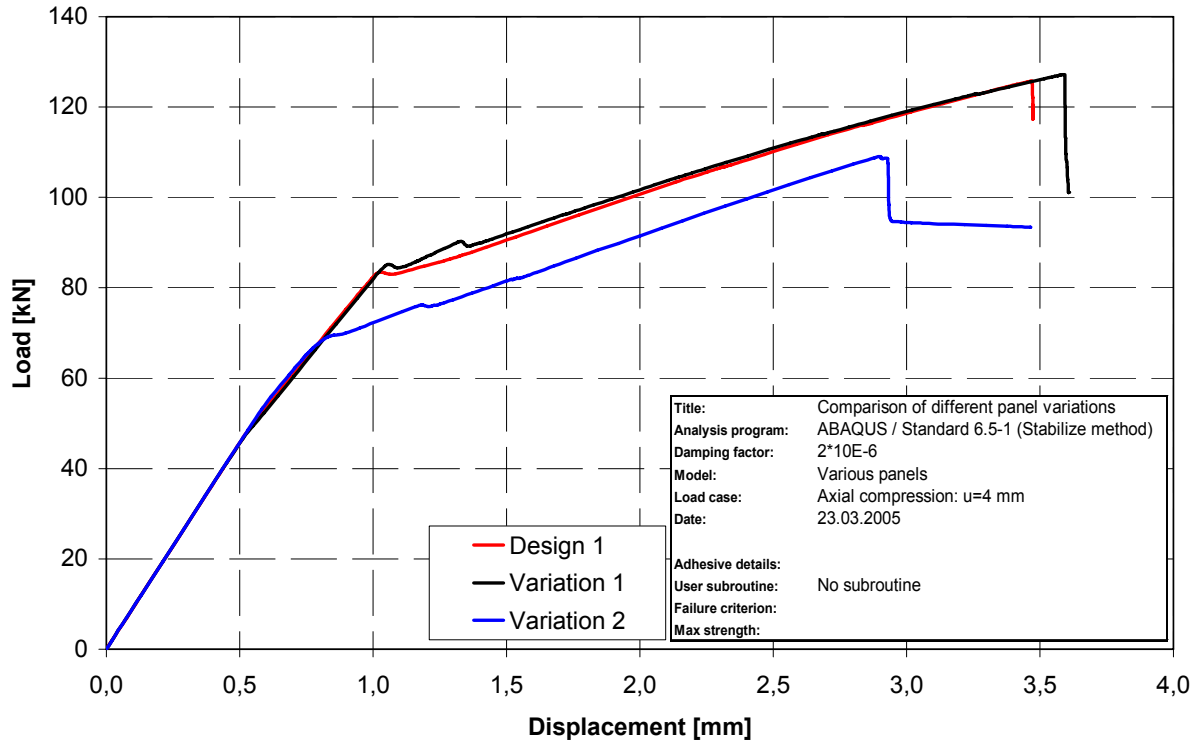


Figure 4-8 Load-shortening graph of panel V15 with different mesh densities [17]

From the high similarity of the load-shortening graph it was concluded that the differences in axial stiffness were negligible. The collapse of the panel was initiated slightly earlier than the collapse of the V1 panel, but the results of the D1 model were taken as sufficiently accurate for all further investigations, with and without the degradation subroutines previously described.

As mentioned earlier, the number of elements was reduced to 7,956. In contrast to the model with 40,000 elements, which was modeled with four elements along the web and eight elements along the flange, the web of the D1 model contained only two elements while the stringer flange was modeled with four elements in the width direction. Eight rows of elements were placed between the stringers. The model contained a total of 78 elements in the axial direction.

4.4 Numerical results without degradation

In real structures discrepancies are often included during the manufacturing process for example inhomogeneous concentration of the fiber in composite structures. These discrepancies are called imperfections. Besides the imperfections due to the manufacturing process, eccentric introduction of load shows similar influence on the stability of the structure. While plates are rather nonsensitive to imperfections, the imperfections are of major importance in shell structures. In this kind of structures imperfections lead to a strong

reduction of the critical loading. Shells that are not stiffened fail at the branching point and are only able to carry a small percentage of the original load. This is shown in Figure 4-9. An excess of the critical loading can not be permitted. The influence of imperfections is shown by the dotted lines.

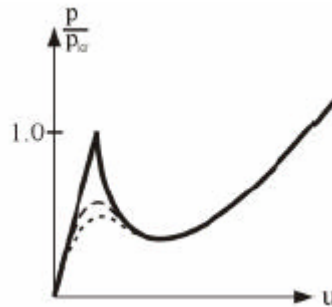


Figure 4-9 Load-shortening graph of shells without stringers [25]

Figure 4-10 shows the load-shortening graph of the D1 panel without degradation involved. This graph gives an impression of the typical buckling behavior of stringer stiffened panels. After the branching point is reached (onset of local buckling), the loading is redistributed in the structure. This means that the percentage of load that is carried by the stringer is increased because the skin is able to carry only a small fraction of the load. Since the stringers are usually much stiffer than the skin, they are able to carry additional load. Only when the loading is increased further, the stringers buckle and the structure experience so called global buckling. If the loading is still increased after global buckling, the structure experiences a breakdown also known as collapse that is characterized by a strong reduction of the load-carrying capacity.

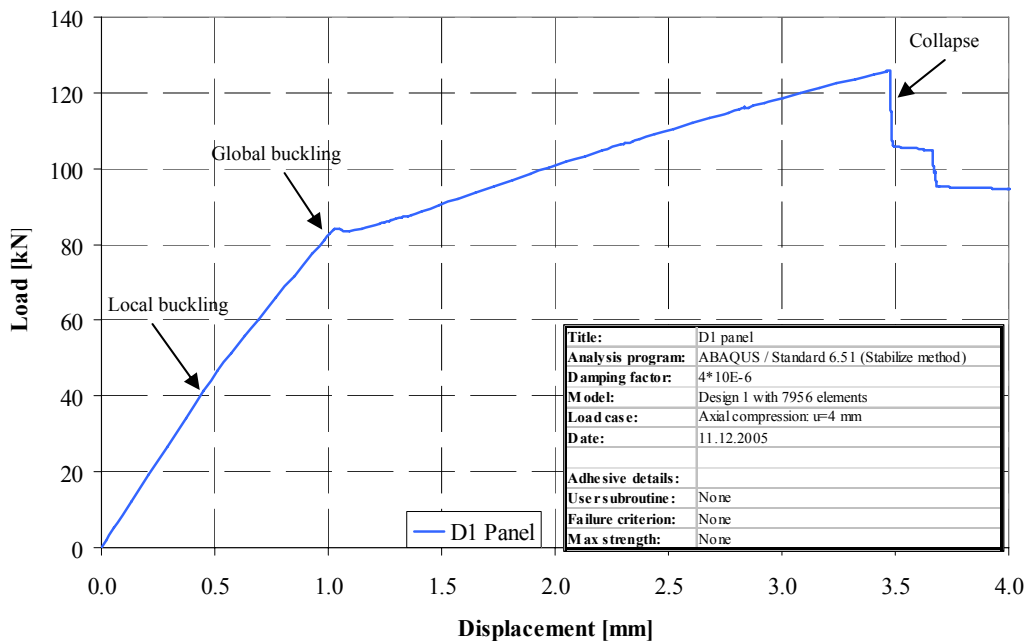


Figure 4-10 Load-shortening graph of the D1 panel without degradation

5. Parametric studies

This chapter is divided into three major parts. The first part focuses on the investigation of the previously developed subroutine UMAT implicit in order to gain a better understanding of the main parameters that influence the simulations. In the next part, changes were done in the geometry of the simulation model to be able to evaluate the influence of different factors as the number of elements in the adhesive or the thickness of the adhesive layer on the subroutine itself. For these parts, the previously developed subroutines were used. The Young's modulus was reduced to 1% of the original value because there were less numerical instability experienced than for a reduction to 0.1% and the computation time was also shorter. This was acceptable because the main focus was put on the investigation of the sensitivity of the routines. The last part includes two different newly developed versions of the USDFLD. The changes were explained in detail and parametric studies were performed to evaluate the accuracy of the different routines.

5.1 Influence of parameters within the UMAT implicit advanced

The first parametric studies performed investigated the numerical stability of the previously developed UMAT implicit advanced. As mentioned earlier the original version of the UMAT implicit had problems with numerical instability. Therefore options to steer the increment size were added to the advanced version of the UMAT implicit. In order to optimize the accuracy and the time consumption of the subroutine, parametric studies were performed for the PNEWDT factor as well as the stress ratio steering the increment size. The results are presented in the following section.

5.1.1 PNEWDT factor [1]

The variable PNEWDT is a factor that is used to steer the increment size. It is provided by the call of the UMAT subroutine. This factor is the ratio between the suggested new time increment, $DTIME_{new}$, to the time increment currently used in the calculation $DTIME_{current}$. In this work, the UMAT implicit advanced used the PNEWDT factor to reduce the increment size in the case that the stress ratio steering the increment size (Section 5.1.2) was exceeded or if failure occurred in more than one element in the first iteration.

$$PNEWDT = \frac{DTIME_{new}}{DTIME_{current}} \quad (5-1)$$

PNEWDT is the factor of the time increment change. This variable allows the user to provide input to the automatic time incrementation algorithms in ABAQUS. It can be updated during the run of the subroutine and leads to a restart of the increment. Normally, PNEWDT is set to a large value by ABAQUS before each call of the subroutine. If the PNEWDT factor is defined to be less than one, the time increment is cancelled by ABAQUS. Afterwards ABAQUS attempts the time increment with a smaller increment size. The suggested new time increment provided to the automatic time integration algorithms is given by

$$DTIME_{new} = PNEWDT \cdot DTIME_{current} \quad (5-2)$$

The value of PNEWDT used is the minimum value for all calls to the user subroutines that allow redefinition of PNEWDT for the current iteration.

In case that the value of PNEWDT is defined to be greater than one for all calls to the user subroutines for the current iteration and the increment converges in the iteration, the time increment may be increased by ABAQUS. As mentioned earlier, the suggested new time increment that is provided to the automatic time incrementation algorithms is the product of PNEWDT and the current time increment $DTIME_{current}$. The PNEWDT factor used is the minimum value for all calls to user subroutines for this iteration.

If no automatic time incrementation is selected in the analysis procedure, all values that are greater than one are ignored and all values of PNEWDT that are less than one cause the job to terminate. It is important to mention that in this work, static displacement controlled analysis were performed. This means that when speaking about a reduced increment size it is meant that the applied displacement change was reduced. The reason for this was that there was no time step available in the analyses.

Figure 5-1 shows the load-shortening curve of the parametric study investigating the PNEWDT factor. Four different factors were applied, the smallest value was 0.8, the highest value was 0.95. The first three factors showed very similar results. The only differences can be found in the deep post buckling region at a shortening of approximately 3.5 mm. With a PNEWDT factor of 0.95 a slightly different buckling behavior was predicted even at smaller shortenings of the panel. The first difference to the load-shortening curves of the other factors occurred at a shortening of approximately 2.75 mm.

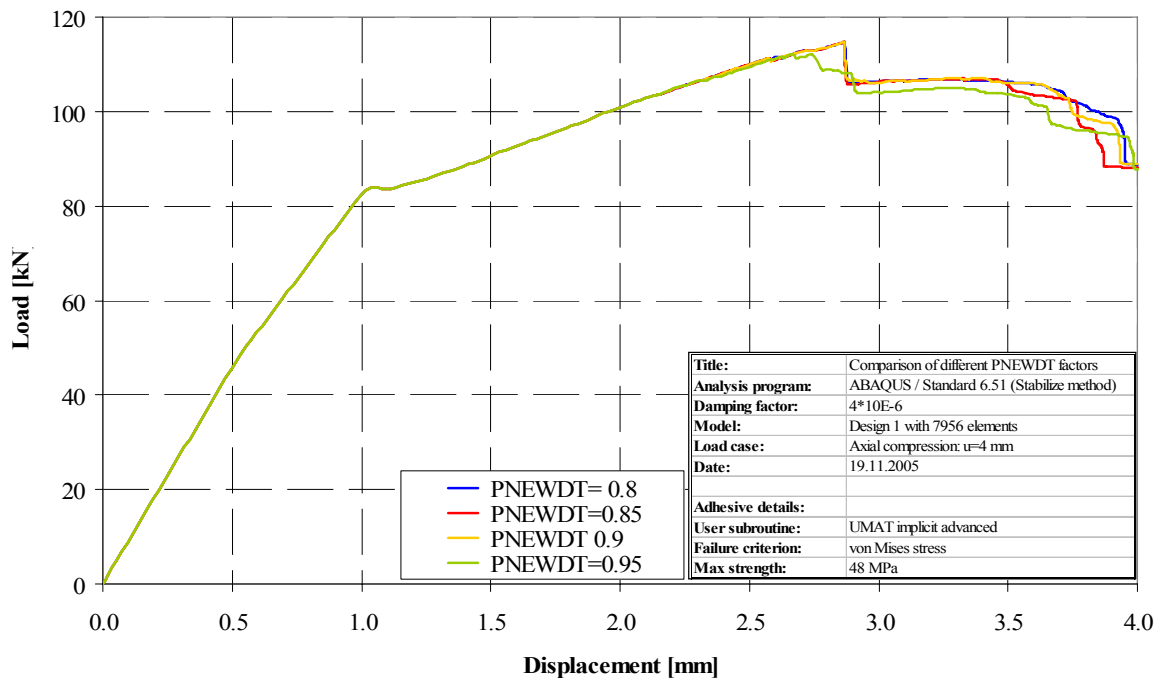


Figure 5-1 Load-shortening curve with different PNEWDT factors

Besides the accuracy of the simulation, the next criterion in order to choose a PNEWDT factor for further investigation was the time consumption. The time consumption of the different simulations is shown in Table 5-1. The longest time that was used to complete the analysis of the D1 panel was for the PNEWDT factor of 0.95. The PNEWDT factor that showed similar buckling behavior as the simulations with the other factors but with a

significantly smaller computation time was the PNEWDT factor of 0.85. The analysis time was 15 hours and 53 minutes.

PNEWDT-factor	Seconds [s]	Hours [h:min:s]
0.8	105,457	29:37:17
0.85	57,182	15:53:02
0.9	141,128	39:12:08
0.95	172,144	47:49:04

Table 5-1 Time consumption for the analysis of the D1 panel for different PNEWDT factors

Values of PNEWDT close to one give an inefficiently slow increment reduction, which makes an increased number of cut-backs necessary during analysis. On the other hand, PNEWDT factors that are too small give a faster reduction of the increment size but could result in a overly small increment. This leads to an inefficient process in which ABAQUS resizes the next increment while at the same time the subroutine repeatedly shrinks the increments size every first iteration. Especially when models with a large number of elements are investigated, a large number of equilibrium iterations and cut-backs can be caused by the advanced version of the UMAT implicit. An increasing number of equilibrium iterations and cut-backs leads to a higher time consumption and makes the usage of the ABAQUS *CONTROLS command [1] necessary. The parameters are dependent on each other and on the model that is analyzed. The CONTROL command is included in the input file of a model. It is usually used to optimize the performance of the solving process. The command is placed after the *STEP/*STATIC command lines:

```
*CONTROLS, PARAMETER=TIME INCREMENT
50, 50, 50, 50, 40, 8, 15, 20, 12
```

The first value represents the number of equilibrium iterations after which the check is made whether the residuals are increasing in both of two consecutive iterations.

The second parameter is the number of equilibrium iterations at which logarithmic rate of convergence check begins.

The next value is the number of equilibrium iterations after which the residual tolerance is used.

The fourth value gives the maximum number of equilibrium iterations that is allowed. The default value is $I_C=16$.

The next value represents the number of equilibrium iterations after which the increment size is reduced with a default value of $I_L=10$.

The sixth parameter is the number of equilibrium iterations allowed in consecutive increments for the time increment to be increased.

The next value represents the maximum number of severe discontinuity iterations allowed in an increment.

The eighth value steers the allowable cut-backs of an increment. The corresponding default value is $I_A=5$.

The last parameter controls the maximum number of severe discontinuity iterations allowed in consecutive increments for the time increment to be increased.

The parameters that were considered most important because they were sometimes changed during the analysis were the forth, the fifth and the eighth value.

Since the results of the first three simulations were very similar, the smaller time consumption of the PNEWDT factor of 0.85 was the major reason for the decision to perform further simulations with a factor of 0.85.

5.1.2 Stress ratio control

For the UMAT implicit, the PNEWDT factor and the critical stress ratio have to be defined. When the stresses are calculated, the ratio of the maximum allowable stresses to the current stress is calculated.

$$ratio = \frac{\sigma_{current}}{\sigma_{max.allowable}} \quad (5-3)$$

The ratio needs to satisfy two conditions. It has to be larger than 1.0 and at the same time it may not exceed a defined critical value. If this critical value is exceeded, the PNEWDT factor is used to decrease the increment size. When the increment size is decreased, the current stress state is reduced as well. Therefore the stress ratio decreases. The subroutine also checks if the integration point has already failed in a previous increment. Otherwise it is not necessary to decrease the size of the increment. The values of the stress ratio are usually 5% to 10% above failure stress. This means that the stress ratio has to be larger than 1.0 and below 1.05 or 1.10 to successfully detect failure within the iteration. If the critical value is exceeded, PNEWDT is used to reduce the size of the increment. The mechanism is used to steer the increment size of the subroutine.

Figure 5-2 shows the parametric study performed with the stress ratio. Six different ratios between 1.05 and 1.1 were simulated. The results calculated are very similar even in the deep postbuckling region and there are only very small differences between different the curves. These differences can be considered negligible.

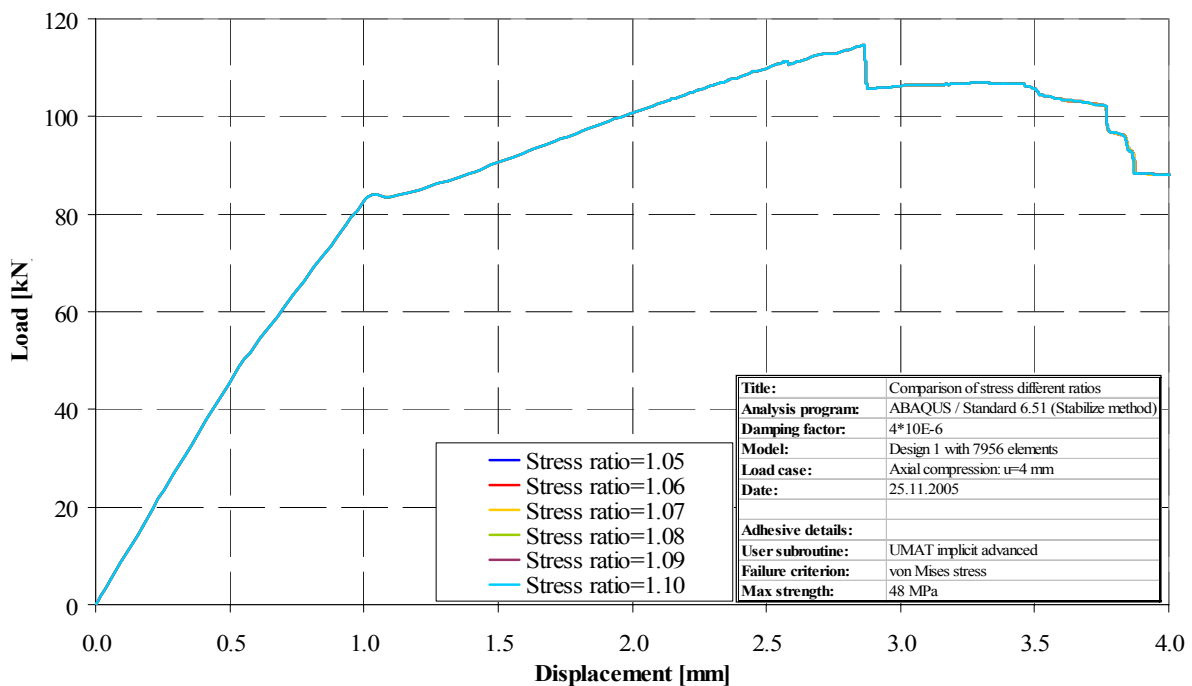


Figure 5-2 Load-shortening curves with different stress ratios

From the load-shortening graph it was concluded that the stress ratio is not a critical parameter in terms of accuracy of the simulation because it does not have a great influence on the results of the analyses.

Although the actual results of the simulations were very similar for all stress ratios analyzed, the computation time showed great discrepancies. The time consumption of the UMAT implicit advanced for the D1 panel is given in Table 5-2. The computation time varied between 22:26:54 hours for a stress ratio of 1.08 and 52:11:56 hours for a stress ratio of 1.07. This is a difference of more than 230%. Since these two stress ratios were right next to each other in the parametric study, it is difficult to give a clear recommendation for the choice of a stress ratio. Since the increase of time consumption is stronger at values smaller than a stress ratio of 1.08, stress ratios greater or equal to 1.08 are recommended. In this work a stress ratio of 1.1 was used for all further simulations.

Stress ratio	Seconds [s]	Hours [h:min:s]
1.05	162,917	45:15:17
1.06	177,543	49:19:03
1.07	187,916	52:11:56
1.08	80,814	22:26:54
1.09	119,281	33:08:01
1.10	120,654	33:30:54

Table 5-2 Time consumption for the analysis of the D1 panel for different stress ratios

One element failure control:

For the sake of completeness a brief description of the second method to steer the increment size is given in the following paragraph, although no parametric studies have been performed with this parameter.

This program counts the calls of the subroutine during the analysis and the failing elements per iteration. If more than one element is failing in the first iteration of an increment, the increment size is reduced. When the increment size is reduced and the first failing element failed, the analysis will not take this option into account for the remaining iterations of the increment. This method prevents ‘domino’ effects of material failure, especially in the case of small stress gradients around a failure site. A more detailed description can be found in [17].

5.2 Variation of the geometry of the simulation model

In order to test the sensitivity of the subroutines to changes in the geometry of the model, three different variations of parameters concerning the adhesive were performed. The first one was the variation of the thickness of the adhesive. The influence of the variation of the numbers of elements in thickness direction as well as the axial direction was also tested. The subroutine used was the original version of the USDFLD, which was previously developed in [17/23]. This subroutine uses the von Mises stress as comparison stress in order to predict the failure of the adhesive. The comparison stress used in all simulations in this section was 8.3MPa. Although this subroutine does not predict the failure in the adhesive in the most accurate way, it was used to investigate the influence of the different parameters because the time consumption was less than in any other subroutine developed and tested so far. Since in

this investigation only results of the subroutine were compared to each other, the version of the subroutine used was considered of minor importance.

For the sake of completeness it has to be mentioned that during the process of changing the model, several modeling errors were detected. It was found that the length of the beam elements used to symbolize the MPCs in the model as described in Section 4.3, was not constant over the adhesive. This means that the five rows of nodes used to form the four rows of adhesive elements over the length of each stringer had different distances to the adhesive. The model of one stringer with its corresponding nodes is shown in Figure 5-3. Table 5-3 gives a summary of the different lengths of the beam elements and the error in percent compared to the desired distance.

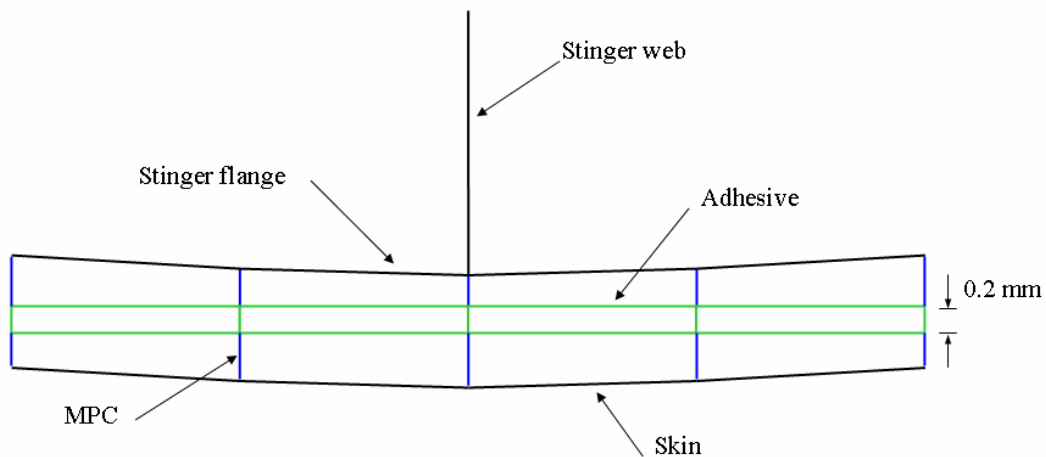


Figure 5-3 Build up of the stringer model

Node	Lower beam length [mm]	Actual lower beam length [mm]	Error [%]	Upper beam length [mm]	Actual upper beam length [mm]	Error [%]
1	0.5	0.5	0	0.75	0.75	0
2	0.5	0.598	19.6	0.75	0.653	-12.9
3	0.5	0.63	26.0	0.75	0.62	-17.3
4	0.5	0.598	19.6	0.75	0.653	-12.9
5	0.5	0.5	0	0.75	0.75	0

Table 5-3 Variation of the beam length

The table also shows that the sum of the actual upper and lower beam length was the same for all nodes. The distance between the nodes of the adhesive elements was also always the same for the five rows of nodes.

The reason for this modeling mistake might be that at the first attempt to model the adhesive layer, only one element was used instead of the four necessary elements. Afterwards this element was split into the four rows of adhesive elements. Therefore the fact that the panel was curved was not taken into account for the modeling of the adhesive because the elements themselves did not have a curved shape.

Since this error was made in the original D1 model, all simulations still had the same starting conditions. Therefore the influence of the mistake was considered to be roughly the same in

all simulations performed. Since this was a “constant” mistake in all simulations it was considered negligible in the comparison of models to each other.

It only had to be taken into consideration when comparing analysis results to experimental data. In order to evaluate the influence of the modeling mistakes, the corrections were done in the D1 panel. The comparison of the model with and without the modeling mistakes is shown in Figure 5-4. It was concluded that the influence of the modeling mistakes were very small. The only difference was that the model without modeling errors predicted the onset of collapse slightly earlier. This meant that the influence of the modeling mistake was non conservative. Still, the differences were considered negligible. Therefore the analyses were not performed again with the corrected version of the model.

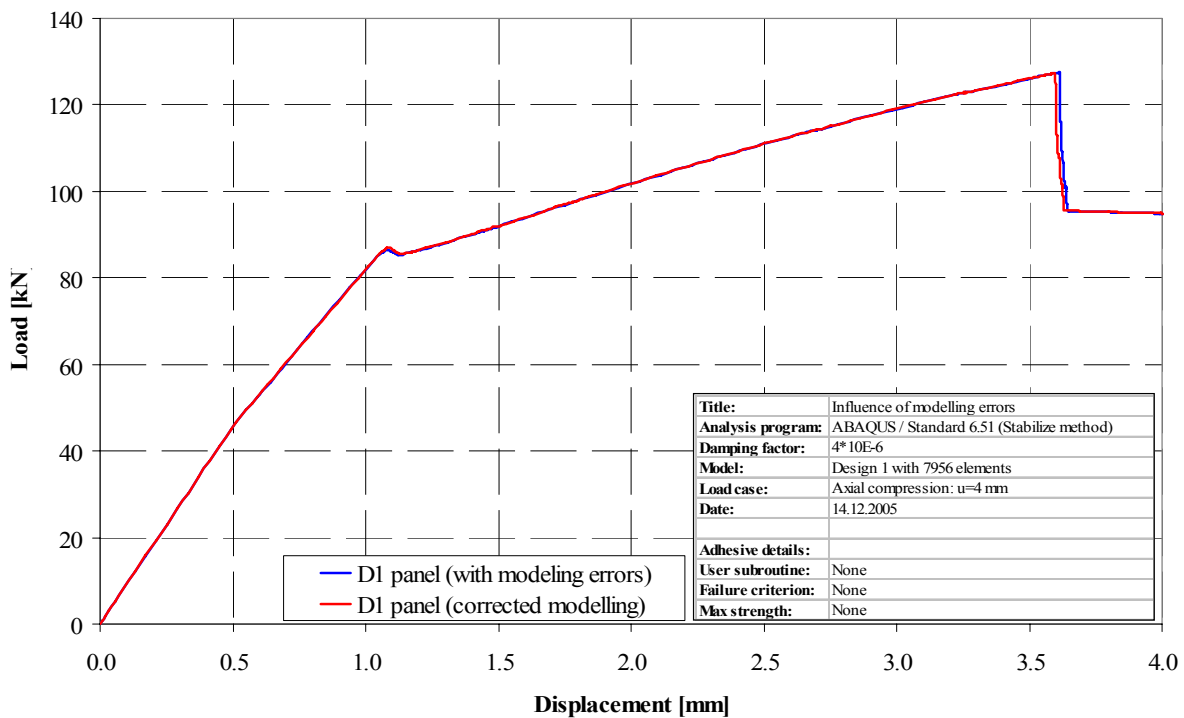


Figure 5-4 Load-shortening curves of the D1 panel with and without modeling mistakes

5.2.1 Variation of the thickness of the adhesive layer

The first parametric study to investigate the sensitivity of the subroutine to changes in the geometry of the model was the variation of the thickness of the adhesive layer. The original thickness was 0.2 mm because this was the thickness that was manufactured during the bonding process. Five additional simulations were performed with thicknesses of 0.1 mm, 0.4 mm, 0.6 mm, 0.8 mm and finally 1.0 mm.

As described earlier, Patran was used as the pre-processor for all models. Therefore the changes in the model’s geometry were performed in Patran. Varying the thickness of the adhesive was a simple change that was performed in two steps. First, all the nodes of the adhesive, which were connected with the MPCs to the stringer of the panel were moved according to the chosen thickness. It was important to create a cylindrical coordinate system before the moving process to guarantee that the nodes moved in the direction of the radius to ensure that the form of the elements did not change. After the nodes of the adhesive were moved into their new position, the connecting nodes of the upper stringer flange were moved

the same distance into the same direction. Afterwards the new node locations were used to replace the old nodes in the ABAQUS input file.

The influence on the load-shortening graph of the variation of the thickness of the adhesive layer is shown in Figure 5-5. The original simulation with a thickness of 0.2 mm is represented by the red curve. The graphs show that the stiffnesses of the panels prior to global buckling was very similar. The earliest prediction of global buckling was given by the adhesive thickness of 0.1 mm. Also the shape of global buckling was not detected as clearly as in the other simulations. For the other models, the onset of global buckling was shifted towards higher values of displacements for increasing thickness of the adhesive. For a thickness of 0.2 mm global buckling was predicted at a shortening of 1.02 mm, for a thickness of 1.0 mm the onset of global buckling did not appear until a displacement of 1.12 mm. This responds to a difference of 8.93% when using the value for a thickness of 0.2 mm as reference value.

After global buckling the curves did not look as similar. The blue curve representing the thickness of 0.1 mm showed the most significant changes in comparison to the original red curve. Although global buckling was predicted earlier, the stiffness in the postbuckling region was higher than the results of the other simulations. It also was the only curve that showed decreasing stiffness after the change into the second global buckling mode shape at approximately 2.75 mm. In the postbuckling region between global buckling and 2 mm displacement, the models showed different behavior according to the thickness.

Even though this was the case, the progression of the curves of the different simulation models looked more similar to the original calculation than the blue curve, although they all showed a reduced stiffness in comparison to the red curve. Even when the thickness was increased from 0.4 mm to 1.0 mm the final stiffness of all models was similar from 2 mm to 4 mm of displacement. When comparing the stiffness in this region of the original model and the other simulations, the deviation was not higher than 13.31% at the maximum shortening of 4 mm.

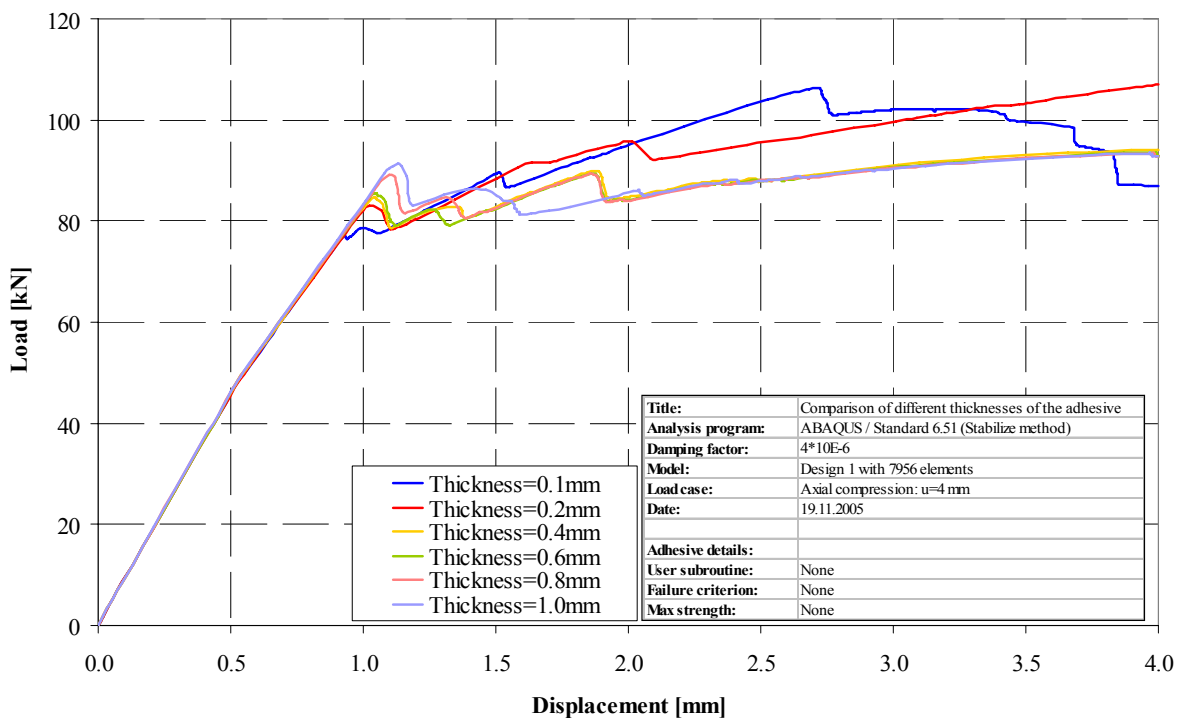


Figure 5-5 Load-shortening curves for different thicknesses of the adhesive

From this parametric study it was concluded that the influence of the adhesive thickness could not be ignored. The onset of global buckling and the stiffness in the post buckling region were predicted differently. The influence of the adhesive thickness has to be taken into consideration when investigating the behavior of the panel.

This parametric study did not investigate the influence of varying adhesive thickness over the panel length. This means that changes in the thickness of the adhesive layer due to manufacturing influences were not simulated. The parameter of the thickness usually is a criterion used in the designing and modeling process because the thickness of the adhesive is predefined during the manufacturing process. Therefore it is very unlikely to find a constant thickness with values higher than 0.2 mm because this was the predefined value of the manufacturing. Still it is possible that changes of the adhesive thickness occur during manufacturing. With the simulation of the different thicknesses it can be assumed that the influence of these changes is small.

5.2.2 Variation of the number of adhesive elements in the thickness direction

In this parametric study the number of elements in the thickness direction was doubled. This means that instead of one row of elements, two rows of adhesive elements were modeled in the radial direction. The changes in the original model were performed in Patran. The modeling was a little more complicated than the modeling of the different thickness of the adhesive. First, the nodes of the adhesive on the stringer side were moved in the direction of the radius. Through this move the thickness of the adhesive was reduced to 0.1 mm. Afterwards a copy of these elements was made in radial direction. The problem was that the beam elements were still connected to the original nodes, now located at a thickness of 0.1 mm. Therefore all beam elements connecting the stringer flange and the adhesive had to be moved to link with the new boundary nodes of the adhesive. Afterwards the new nodes and the old nodes with their new coordinates were entered into the input file. The beams also had to be changed because they did not connect the same nodes as they did previously. They now connected the stringer flange with the new nodes of the newly created adhesive element. The new adhesive elements were also added to the input file and the corresponding group in order to have the same material behavior as the original adhesive elements. Figure 5-6 shows the original and the new build up of the adhesive layer.

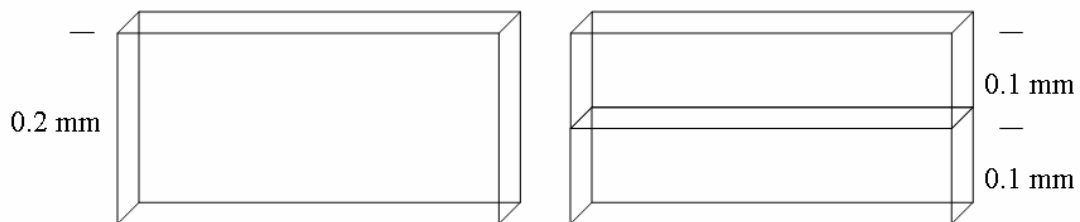


Figure 5-6 Different build ups of the adhesive layers

When running the calculation with ABAQUS, the program outputs a warning in the .dat-file that the aspect ratio was greater than 100 for some elements. The aspect ratio is defined as the ratio between the longest and shortest edge of an element. In this case, the longest side of the adhesive elements was 10 mm and the reduced thickness of the elements was 0.1 mm. The

warning was not given out for all elements in the adhesive layer because the aspect ratio varied for the different elements. The same warning was given for the variation of the adhesive thickness when it was reduced to 0.1 mm. The advised critical ratio of 100 was only slightly exceeded due to modeling mistakes for some elements. There were no convergence problems occurring during the analysis and the effect on the accuracy of the simulation was considered negligible.

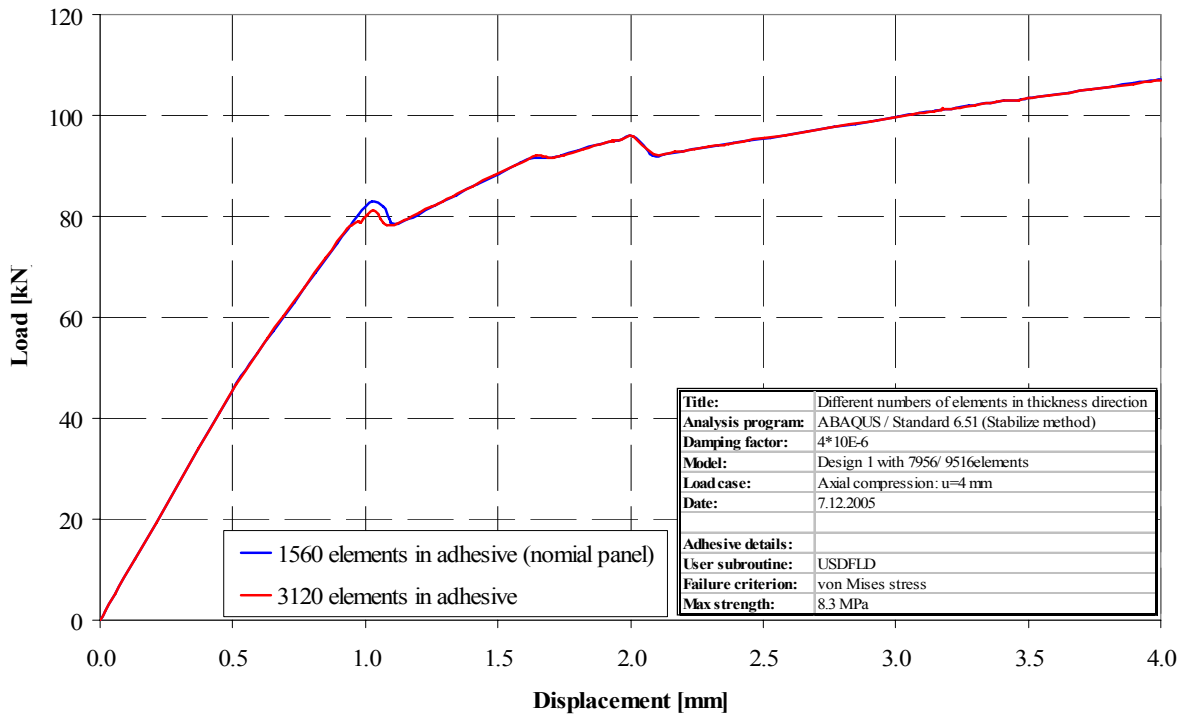


Figure 5-7 Load-shortening curves for different number of adhesive elements in thickness direction

Figure 5-7 shows the load-shortening curve of the original model with 1560 elements in the adhesive (blue curve) and the new model with the double number of elements (red curve). It was shown that the influence of the number of elements was very small. The only difference between the two curves was found in the region of global buckling. In the new model, the reduction of the load-carrying capacity occurred under an axial load of 80.83 kN while the original model did not show this reduction until a load of 83.02 kN. This was an error of 2.62% when taking the original value as reference value. After global buckling the stiffness of the original model was slightly less than the stiffness of the new model but this deviation was considered negligible. It was concluded that the influence of the number of elements in the thickness direction was small and that therefore one row of elements was preferred due to the smaller modeling effort.

The prediction of failure was also very similar to the original model. The occurrence of failure was predicted in the elements of the adhesive. The elements of the newly created row failed in the same increment when their neighbor original element failed. This explains the great similarity of the two load-shortening curves.

5.2.3 Variation of the number of elements in the axial direction

The last parametric study performed, that included geometrical changes in the original model, was the variation of the number of adhesive elements in the axial direction. The changes that were done in Patran were the most complex changes because in order to change the number of elements in the adhesive, the elements of the entire model were changed, too. This is because the nodes of the adhesive elements were connected rigidly to the nodes of the skin and stringer elements. First, all the original elements were deleted except for the one row of elements so that one complete set of elements for the skin, the stinger web and the stringer flange existed in radial direction of the panel. In this case the first row of elements on the bottom of the panel was used. Next the nodes on the side of the elements that was orientated towards the upper side of the panel were moved so that the length of the elements themselves was reduced from 10 mm to 2.5 mm. This meant that the dimension of the panel in axial direction was reduced to 25% of the original length. Afterwards the radial row of these new smaller elements were duplicated 311 times in axial direction to add up to the panel length of 780 mm. Originally there were 78 elements in axial direction of the panel but since the length of one element was reduced to $\frac{1}{4}$ of the original length, the number of elements had to be increased by a factor four to add up to the original panel length of 780 mm. It was important to select only the row of the beam elements to be copied that was orientated to the bottom of the panel because otherwise there would have been two beam elements at the same nodes.

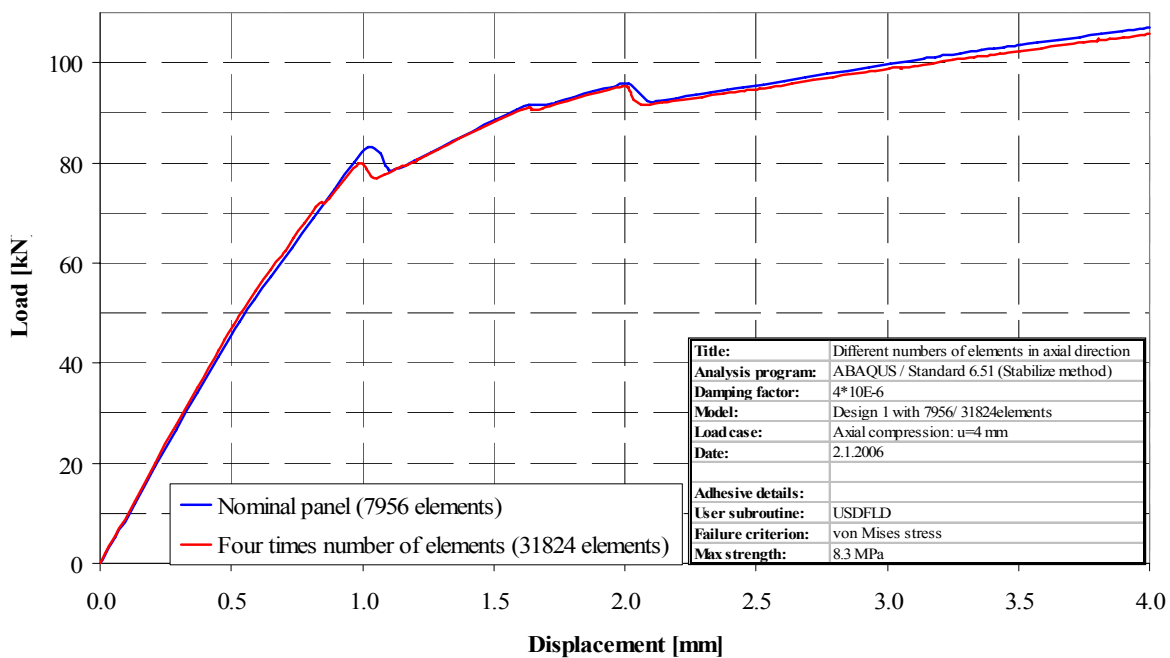


Figure 5-8 Load-shortening graph of different numbers of adhesive elements in the axial direction

The copying of the elements was followed by the redefinition of the groups since all the groups consisted of entirely new nodes and elements numbers. Afterwards the new nodes, elements and groups were added to the input file and the analysis was performed. The results of the simulation are shown by Figure 5-8.

The result of the simulation with four times the number of elements in the axial direction is represented by the red curve in Figure 5-8. The curve was very similar to the original model with only 78 elements although it predicted a slightly higher axial stiffness after the onset of

local buckling. The main difference was the prediction of global buckling that was predicted at slightly smaller shortenings. The maximum difference in load-carrying capacity was approximately 1.08% between the models with 78 and 312 elements.

The computation time of the two different models is given in Table 5-4. From the data it was concluded that the time consumption of the analyses increased dramatically when the number of elements was increased. The time consumption increased by more than 300% when the number of elements was increased to 312.

Number of elements in axial direction	Seconds [s]	Hours [h:min:s]
78	33,191	09:13:11
312	208,950	58:02:30

Table 5-4 Computation time for different number of elements in the axial direction

Since the load-shortening curves of the panel with 78 and 312 elements gave similar result for the prediction of buckling behavior, it was concluded that for this work it was not practicable to apply the user subroutine USDFLD to models with a great number of elements. This was supported by the enormous additional time consumption when the subroutine was included with the models with smaller element size. Therefore it was recommended that the USDFLD should be used only when the number of elements was not too high although for more precise calculations, the increase of the number of elements was possible.

5.3 Development and application of the USDFLD Tension & Compression

After the evaluation of the sensitivity of the UMAT implicit advanced and the USDFLD to different parameters in the previous sections, a new version of the USDFLD was developed. There were several reasons for the need of an extended version of the user subroutine.

This new version aimed at the implementation of a different failure criterion for the prediction of failure because in the original version of the user subroutines, the von Mises yield criterion was used to predict the failure of the elements. As described in Section 2.2, the von Mises stress was a comparison stress that used all three normal stress components σ_x , σ_y , σ_z and the three shear stress components τ_{xy} , τ_{xz} , τ_{yz} to calculate the corresponding stress.

Also the von Mises yield criterion did not take the differences in the maximum compressive stress and the maximum tensile stress into consideration in an accurate way. The only possible ways to predict failure were to compare the von Mises stress to the maximum tensile stress or to the maximum compressive stress. The different results of these two ways of failure prediction are shown in Figure 5-9. It should be noted that in this graph, the declaration of the curves was accidentally exchanged. The blue curved termed as “Advanced-failure stress: 48 MPa” actually used a failure stress of 8.3 MPa. Additionally, the red curve labeled as “Advanced-failure stress: 8.3 MPa” used a failure stress of 48 MPa. The graph was taken from the source [17] because the results of the simulation were already deleted when this work was written.

It is shown that in comparison to the previously performed simulation with a failure stress of 48 MPa, the degradation of the adhesive layer using a comparison stress of 8.3 MPa reduces the axial stiffness of the panel during the entire deep postbuckling region significantly but it

did not produce a proper collapse point. In this work the term “deep postbuckling region” means the displacement region with higher shortenings when global buckling already occurred. The other main difference was that global buckling was predicted earlier when the lower comparison stress was used. This version of the subroutine was not able to distinguish between failure due to tension or due to compression. In order to predict failure more accurately, a version of the subroutine was developed that was able to distinguish between failure due to tension and failure due to compression.

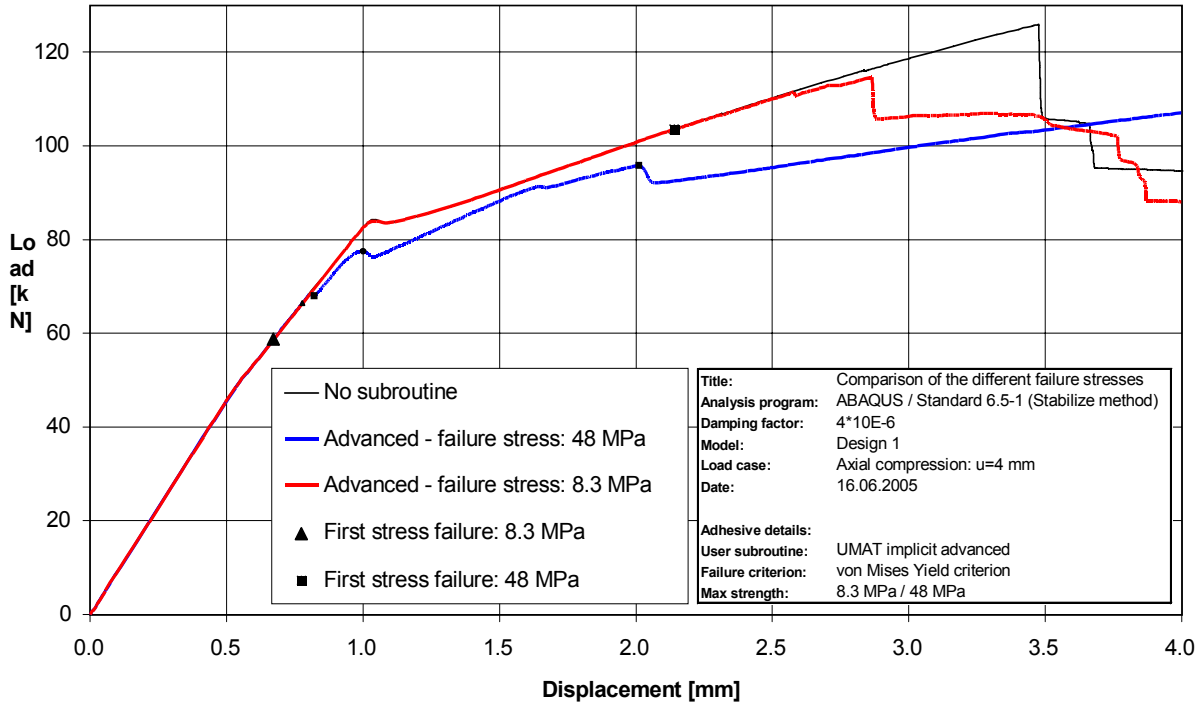


Figure 5-9 Comparison of different failure stresses [17]

5.3.1 Explanation of the subroutine code of the USDFLD Tension & Compression

A description of the basic concept and data flow of the USDFLD as well as the usage of field variables to define the material properties was already given in Section 3-2. Therefore this chapter mainly concentrates on the changes made in the new version of the user subroutine to distinguish between failure due to tension or compression. This version of the subroutine takes the normal stresses into account for the prediction of adhesive failure. The attempt to use the normal stresses is not very realistic in physical terms because the failure prediction then depends on the choice of the coordinate system. This problem will be explained more thoroughly in Section 5.3.4. Still, this section was included in this work because the conclusions made and the programmed code were used to develop the version of the USDFLD that used the principal stresses for failure prediction.

The definition of the maximum allowable stresses was changed in order to take the problem of Tension & Compression and therefore the problem of positive and negative preceding sign into account. This is the reason why SMAXDruck, the maximum compressive stress of the adhesive material, is defined negative in contrast to the earlier versions of the routine.

```
PARAMETER(SMaxS11=8.3D0,SMaxS22=8.3D0,
           SMaxS33=8.3D0,SMaxShear=38.D0,
           SMaxDruck=-48.D0)
```

It has to be mentioned that the variable SMaxDruck now actually represents a minimum. The next change was that the three normal stresses and the three shear stresses were used to predict failure. This is already shown by the call of the stresses of the current increment.

```
call getvrm('S',array,jarray,flgray,jrcd,
$   jmac, jmatyp, matlayo, laccfla)
S11 = array(1)
S22 = array(2)
S33 = array(3)
S12 = ABS (array(4))
S13 = ABS (array(5))
S23 = ABS (array(6))
SShear = MAX (S12, S13, S23)
```

In this part of the subroutine all six elements of the stress array are called. The three normal stresses were separately compared to the maximum allowable stresses while for the shear stresses, only the absolute maximum value was taken. This was possible because they were all compared to the same critical stress of 38 MPa. Therefore the number of relevant stresses decreased from six to four.

In the next step, the maximum stresses up to the currently running increment were called. Again, only the relevant stresses were called from the SDV array.

```
S11MAX = ARRAY(1)
S22MAX = ARRAY(2)
S33MAX = ARRAY(3)
SShearMAX = ARRAY(4)
```

After this call, the maximum stresses that were used to be compared to the maximum allowable stress had to be chosen in order to predict failure correctly. This was more complex than in the earlier version of the routine because the program had to distinguish between six different possible combinations of positive and negative stress values instead of only one combination. In the following section, these six possibilities are explained only for the normal stress in the 1-direction. In the complete subroutine that can be found in the Appendix, this part of the code is also repeated for the normal stresses in 2- and 3- direction.

The first possibility was that both the current stress S11 and the stress up to this increment S11MAX were positive. This was the only combination that was needed in the original version of the subroutine because the von Mises stress is always a positive value. In this case, the damage variable was the higher of the two values.

```
IF(S11.GT.0.D0.AND.S11MAX.GE.0.D0) THEN
    Damage1 = MAX( S11 , S11MAX )
ENDIF
```

The next two possible combinations had the same prerequisite, namely that the current stress S11 was positive and the maximum stress up to the increment S11MAX was negative. When comparing these two values, it was not possible to compare only the absolute values. The problem was that the maximal allowable compressive stress was 48MPa and therefore higher than the maximum allowable tensile stress of 8.3 MPa. If only the maximum of the two absolute values was taken, it was possible that it was not the relevant stress that would lead to failure later on.

For example, when $S11=9$ MPa and $S11MAX=-15$ MPa, the maximum value of the absolute values of the two was 15 MPa. Therefore $S11MAX=-15$ MPa would be stored as relevant damage value. In the progress of the subroutine, this value would not lead to failure since the maximum allowable compressive stress was -48 MPa. On the other hand, $S11=9$ MPa would already lead to failure because the maximum tensile stress is only 8.3 MPa but the subroutine would not be able to recognize this exceeded failure criterion.

Therefore the variable “factor” was introduced to make sure that the right value was stored into the damage variable. The variable factor was defined as the absolute value of the ratio of the maximum allowable tensile stress and the maximum allowable compressive stress.

$$\text{factor}=\text{ABS}(\text{SMaxS11}/\text{SMaxDruck})$$

When the product of the factor and the absolute value of the negative stress $S11MAX$ was smaller than the current stress $S11$, the positive stress $S11$ was stored in the damage variable $Damage1$ because then the element was more likely to fail due to tension. The other possibility was that the product of $S11MAX$ and factor was greater than $S11$. In this case, the negative value $S11MAX$ was stored into $Damage1$ because the element was more likely to fail due to compression.

```

IF(S11.GT.0.D0.AND.S11MAX.LE.0.D0) THEN
    IF(S11.GT.(ABS(S11MAX)*factor)) Damage1=S11
    ENDIF
C
    IF(S11.GT.0.D0.AND.S11MAX.LE.0.D0) THEN
    IF(S11.LT.(ABS(S11MAX)*factor)) Damage1=S11MAX
    ENDIF
    
```

The next two combinations also had a similar prerequisite. In both cases the current stress was assumed to be less than 0 MPa and the maximum stress up to the increment $S11MAX$ was higher than 0 MPa. For these possible combinations of positive and negative stresses, the variable factor was also used to choose the relevant stress. This time, the negative variable $S11$ was multiplied with the factor because the maximum compressive stress was still higher than the maximum tensile stress. If the positive stress $S11MAX$ was higher than the product of the variable factor and the negative stress $S11$, the element was more likely to fail due to tension and therefore the positive stress $S11MAX$ was stored into $Damage1$. The other possibility was that the product $ABS(S11)*factor$ was higher than $S11MAX$. In this case the negative stress $S11$ was stored as the damage variable because the element was more likely to fail due to compression.

```

IF(S11.LT.0.D0.AND.S11MAX.GE.0.D0) THEN
    IF(S11MAX.GT.(ABS(S11)*factor)) Damage1=S11MAX
    ENDIF
C
    IF(S11.LT.0.D0.AND.S11MAX.GE.0.D0)THEN
    IF(S11MAX.LT.(ABS(S11)*factor)) Damage1=S11
    ENDIF
    
```

The last possible combination was that both stress values $S11$ and $S11MAX$ were negative. In this case simply the minimum of the two values was stored as the relevant damage stress. It was necessary to take the minimum of the two stress values in order to store the maximum negative stress value into the damage variable.

```

IF(S11.LT.0.D0.AND.S11MAX.LE.0.D0) THEN
    Damage1 = MIN( S11, S11MAX)
ENDIF
    
```

This process was run with the three normal stress components. The main reason to include all these criteria, especially the four where different preceding signs were used, was to prevent the so called healing mechanism when elements could “repair” themselves and set their Young’s modulus back to the original value even though a failure criterion was exceeded earlier. This was very likely to happen in cases when one of the stresses, the current stress or the maximum stress up to the increment, changed its preceding sign during the analysis. To demonstrate this effect an example is given with the prerequisite that the subroutine only distinguished between positive and negative values for S11. The corresponding code lines, which lead to a wrong choice of damage variables are:

```

IF(S11.GT.0.D0) THEN
    Damage1=MAX(S11, S11MAX)
END IF
    
```

and

```

IF(S11.LT.0.D0) THEN
    Damage1=MIN (S11, S11MAX)
END IF
    
```

In this example $S11=-4$ MPa and $S11MAX=9$ MPa. This means that the failure criterion of the maximum tensile stress was already exceeded and the Young’s modulus was reduced. But since the current stress changed its preceding sign from positive to negative in the next call of the subroutine, the other criterion, namely that S11 is negative, will be applied. Therefore the minimum stress value, in this case $S11=-4$ MPa will be stored as the damage value. In the course of the subroutine, this damage value will not exceed the failure criterion and the Young’s modulus is set back to its original value, which would be wrong.

The choice of the damage shear stress variable was simpler because all shear stresses were positive. Therefore the number of possible stress combinations was reduced to one.

```

Damage4=MAX(SShear,SShearMAX)
    
```

The next step was to update the field variables. In this version of the subroutine, four FVs were used to store the damage values of the three normal stresses and the maximum shear stress. The number of possible combinations of field variables that have to be defined in the input file increases from seven to fourteen in comparison to the original version of the USDFLD, which uses only three FVs.

```

FIELD(1) = 0.D0
FIELD(2) = 0.D0

FIELD(3) = 0.D0
FIELD(4) = 0.D0
    
```

After the field variables were set to zero, the subroutine compares the damage stress and the maximum allowable stress in order to predict failure. It is necessary to distinguish between failure due to compression and due to tension. Therefore the following passage was added to the code.

```

IF (Damage1.GT.0.D0) THEN
  IF (Damage1.GE.SMaxS11) FIELD(1) = 1.D0
  ratio1 = (Damage1/SMaxS11)
ELSE
  IF (Damage1.LE.SMaxDruck) FIELD(1) = 1.D0
  ratio1 = (Damage1/SMaxDruck)
ENDIF
    
```

First the subroutine checked if the stored damage variable is greater than zero. If this is the case the damage variable is compared to the maximum allowable tensile stress, when the damage variable is greater than the maximum stress allowed, the corresponding field variable is set to one and the ratio is calculated. The ratio is only needed as output variable in the course of the subroutine. If the damage variable is negative, it is compared to the maximum allowable compressive stress. Again, if the criterion is exceeded the FV is set to one. This part of the subroutine is again repeated for the two additional normal stresses.

For the shear stress, the inquiry simplifies again. In this case it is only necessary to compare to the maximum shear stress since there is only one critical value.

```

IF (Damage4.GE.SMaxShear) FIELD(4) = 1.D0
    
```

At the end of the subroutine, the four damage values are stored into the array of the solution dependent state variables.

5.3.2 Comparison of the different versions of the USDFLD

All normal failure stresses set to 8.3 MPa:

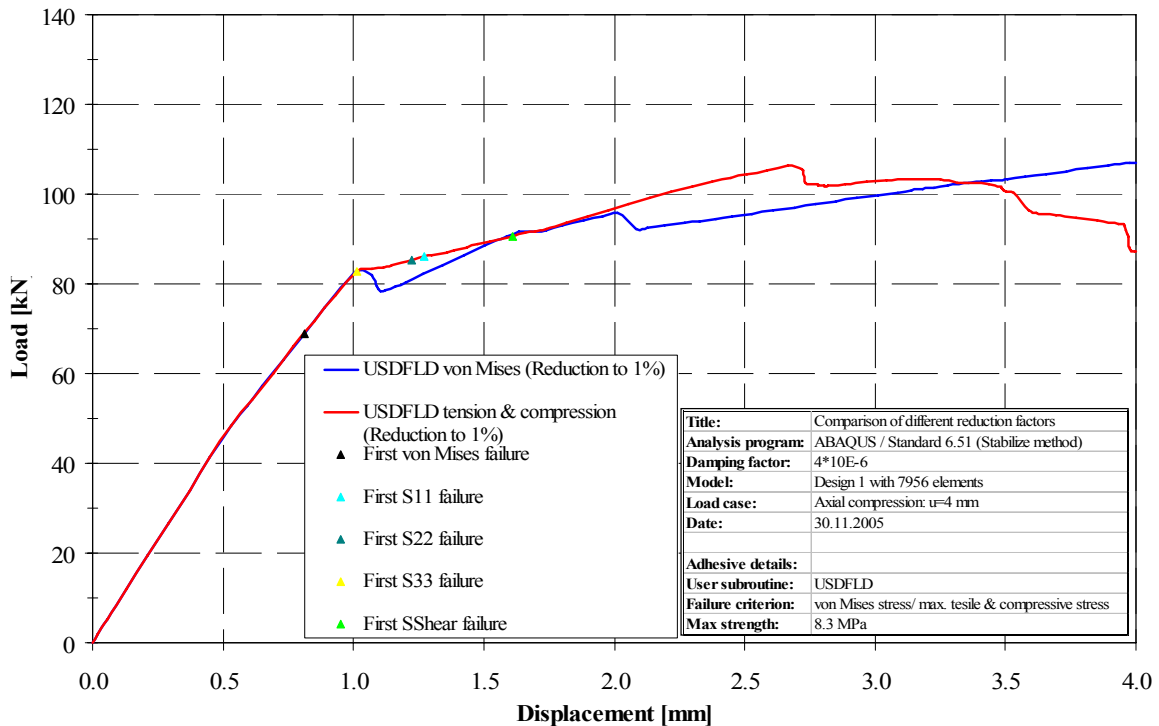


Figure 5-10 Comparison of different versions of the USDFLD for SMAX=8.3 MPa

As a first step, all failure stresses were set to 8.3 MPa in the original version of the USDFLD and the newly developed Tension & Compression version. This was done to receive closer results of the new version to the original version, which used one stress as the critical stress as described earlier for the von Mises stress.

Although this did not meet the demand of a more accurate prediction of failure, which was the main reason for the development of the new USDFLD version, this comparison was done to be able to evaluate if the newly developed version contained major mistakes. Previous controls of the output data of the new USDFLD had been checked and validated earlier for several different models before the analysis was done on the D1 panel.

The Tension & Compression version of the USDFLD only took the three normal stresses and the greatest shear stress into consideration for the prediction of failure. In contrast to the original version of the USDFLD, the von Mises stress was not used. The comparison showed that the prediction of axial stiffness was very similar for both subroutines. The onset of global buckling was also predicted at the same shortening although the new version did not show a strong reduction of the load-carrying capacity as the original version did. After the onset of global buckling the stiffness of the new version was slightly less than the stiffness of the original version up to a shortening of 2.0 mm. At this point, the original version underwent another change of its buckling mode shape while the slope of the new version was constant up to a shortening of approximately 2.75 mm where the new version changed into a new buckling shape. The new version underwent one more change of the buckling mode at a shortening of approximately 3.5 mm while the original version did not show any reduction in the load-carrying capacity.

As mentioned earlier, this comparison was only done to validate the code of the new subroutine. The two load-shortening curves are not perfectly identical because the original version used the von Mises stress as comparison stress for the prediction of failure while the new version used all three normal stresses and the maximum shear stress to predict failure. Still the two curves were similar enough to assume that no major mistakes were present in the code and that the new version of the USDFLD worked correctly.

The computation time of the two subroutines were also compared. The analysis of the original version took a total time of 33191 seconds to be finished. This is equivalent to a time of 9 h 13 min 11 s. In comparison, the computation time of the USDFLD Tension & Compression was 67042 seconds or 18 h 37 min 22 s. This is more than double the computation time of the original version of the USDFLD.

Material properties as failure stresses:

As the next step, the maximum stresses were changed in the new version of the USDFLD. This means that the maximum tensile stress was set to 8.3 MPa and the maximum compressive stress was decreased to -48 MPa. This was done to achieve a more realistic prediction of failure because the material properties of the adhesive material are used more accurately for failure prediction. The results are shown in Figure 5-11 and represented by the green curve. In the following, this version will be referred to as the third version of the USDFLD.

The predicted axial stiffness was very similar for the three subroutines up to the point of global buckling. The two versions of the USDFLD Tension & Compression did not show a relatively strong reduction of load-carrying capacity as the original version of the subroutine

did. In the postbuckling region, the third version (green curve) predicted a slightly higher axial stiffness in comparison to the second version (red curve). This was expected since the failure criteria for the compressive stress was eased because it was set from only -8.3 MPa to -48 MPa. Therefore the actual compressive stress of the elements now had to increase by almost a factor six to cause compressive failure of the element.

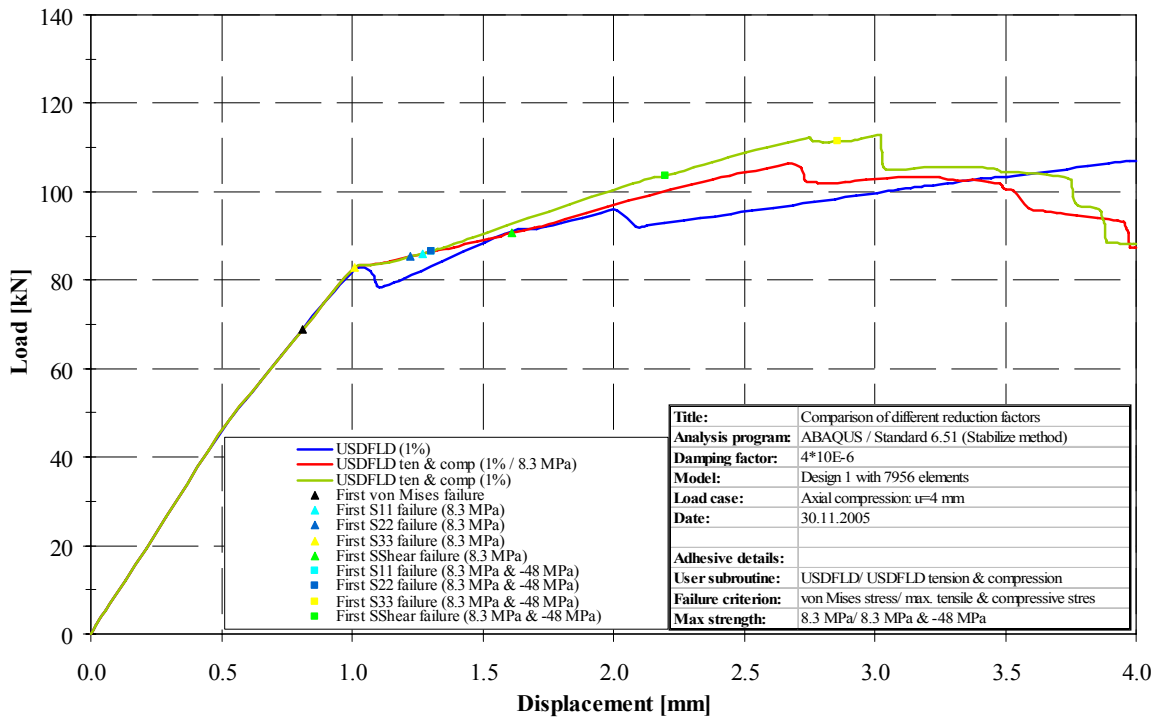


Figure 5-11 Comparison of different versions of USDFLD

In the following progression of the load-shortening curves, the third version predicted the onset of the first buckling mode shape after global buckling at a shortening of approximately 3.02 mm. For the second version this change of buckling mode was experienced earlier at a shortening of 2.72 mm. Afterwards the predicted stiffness was very similar until the second version predicted another change in buckling shapes at approximately 3.58 mm of shortening. The third version did not experience another buckling shape change up to a shortening of 3.76 mm but underwent another change soon after at a shortening of 3.88 mm. The predicted stiffness and main characteristics of the buckling shapes at the final shortening of 4 mm were similar for both routines although the prediction of the location of the main inward buckle differed for the routines. The buckling shape predicted by the original version of the routine differs from the prediction of the new versions because it shows one inward buckle on the right side and one outward buckle on the left side of the panel. The buckling shape is asymmetric. Figure 5-12 shows the buckling shapes of the original version (a), the second version (b) and the third version of the USDFLD (c).

In Figure 5-12 the displacement perpendicular to the panel plane, namely in the 1-direction is shown. In this work, the legend for the displacement in this direction is similar. The colors red and yellow represent positive displacement, which is directed outward in the view given in the corresponding figures, while the blue and green areas represent negative displacement that is directed inward.

The two versions of the USDFLD Tension & Compression showed similar buckling behavior although in the second version the larger buckle was located on the right side of the panel

while for the third version of the routine, the larger inward buckle was placed on the left hand side. The buckling behavior of these routines was approximately symmetric. The original version of the routine showed an asymmetric buckling behavior with one outward buckle on the left side and an inward buckle on the right side of the panel.

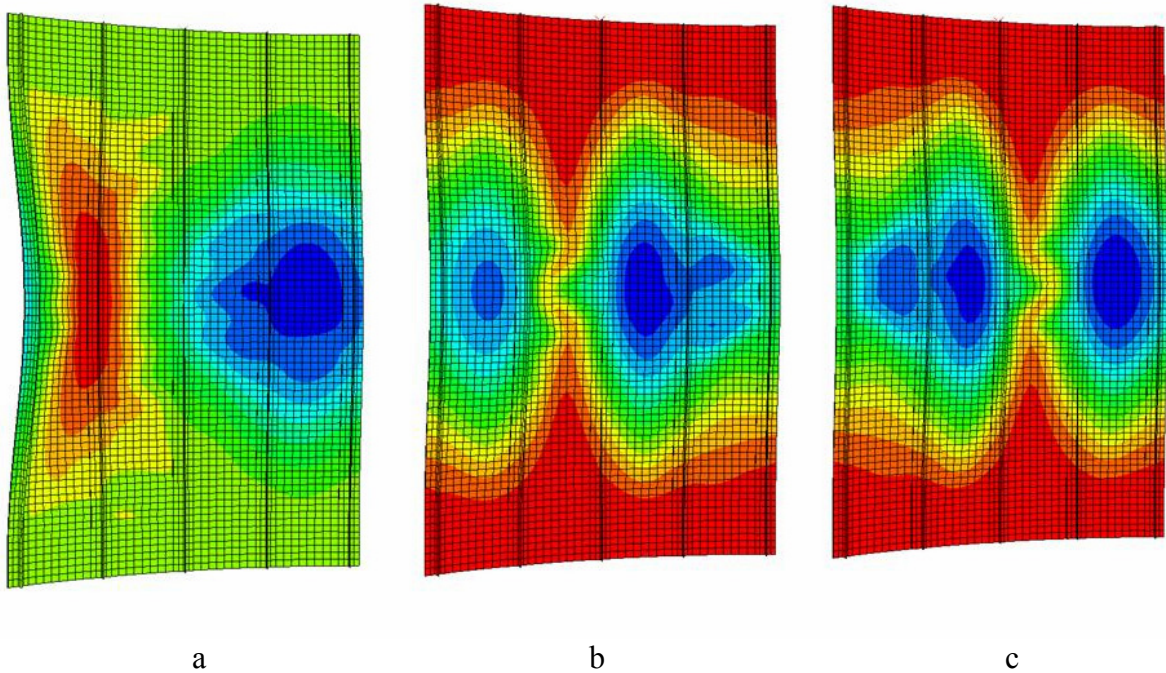


Figure 5-12 Final buckling shapes of the three version of the USDFLD

The next point of comparison between the routines was the differences in the failure prediction. Figure 5-13 shows the five rows of adhesive material at a shortening of 4 mm of the analysis with the original routine. The red color represents elements that failed while elements that have not failed yet are shown in blue. It can be seen that almost all elements in the adhesive were predicted to fail due to transgression of the von Mises stress. Only a few elements at the top and the bottom of the stringer did not fail.

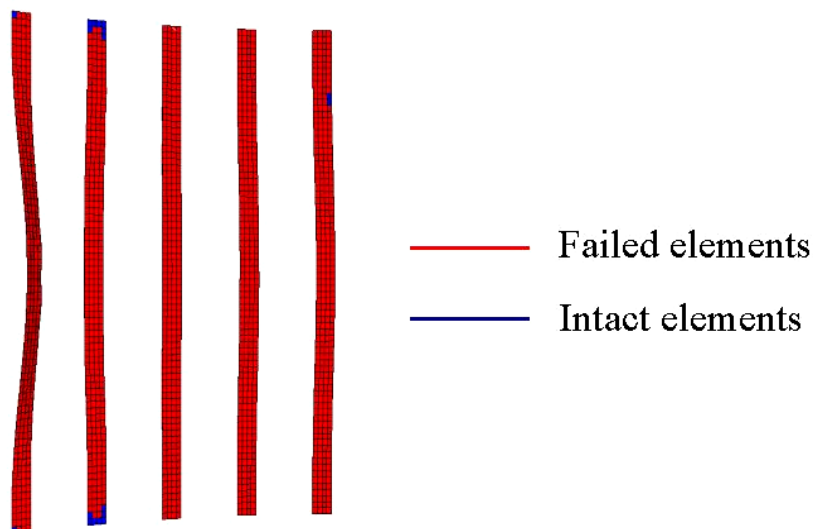


Figure 5-13 Failure prediction for the last increment for the original USDFLD

It was not easy to compare this result to the results of the new version of the routine because the four failure criteria were shown in four different views as presented in Figure 5-14. To compare the actual failure prediction these four views had to be superimposed.

The points of failure prediction for the third version of the subroutine are marked by squares in Figure 5-11. From the load-shortening graph it was concluded that the panel was predicted stiffer. This corresponded to a smaller number of elements that experience failure. This is supported by the view on the adhesive at the final shortening of 4 mm, which is given in Figure 5-14. Most elements failed due to stress in the 1-direction. This was expected because the 1-direction is the direction perpendicular to the skin of the panel. In case of axial compression of the panel and the connected skin-stringer debonding, this fact represented comprehensible structural behavior. From the output of the ABAQUS/ Viewer it was not possible to decide whether the elements failed due to compression or tension although it was possible to include the corresponding code into the subroutine for example with additional FVs. The subroutine also predicted a high number of elements failing due to transgression of maximum allowable stresses in the 2-direction. The 2-direction is located in the panel plane, perpendicular to the direction of loading.

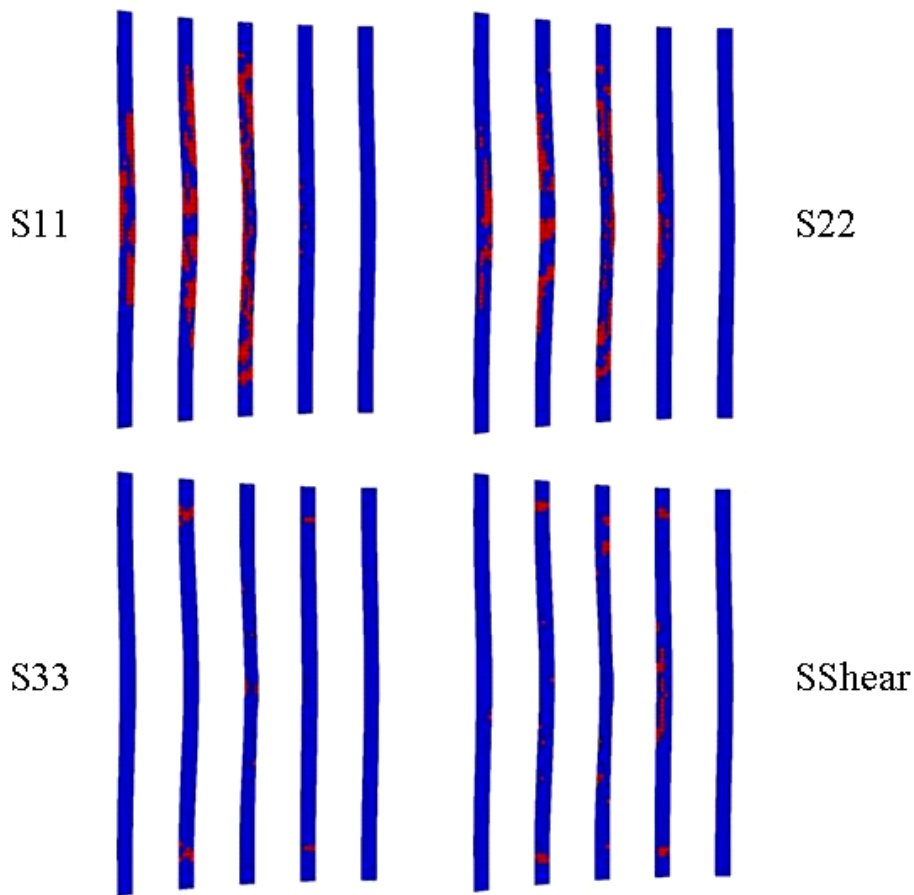


Figure 5-14 Failure prediction for the last increment for USDFLD Tension & Compression

The view on the adhesive also shows that there were very few elements, which were expected to fail due to the transgression of the maximum allowable shear stress or the maximum allowable stresses in 3-direction. These failure criteria were therefore considered less critical than the maximum allowable stresses in 1- and 2-direction.

Although the superposition was only done visually, it was concluded that a smaller number of elements failed in the new routine. This conclusion corresponded well with the load-shortening graph because the USDFLD Tension & Compression showed a stiffer behavior that went along with fewer elements failing.

In conclusion, the version of the USDFLD Tension & Compression took the corresponding material properties as comparison stress to predict the failure of adhesive elements. The new version of the subroutine was also able to distinguish between failure due to compression or tension, which was not possible for the original version since the von Mises stress was always positive, although it was not possible to see the difference in the ABAQUS/ Viewer directly. This change in the subroutine code opened the possibility to apply different material properties for the different coordinate directions and the different stress directions.

5.3.3 Comparison of different failure criteria in the USDFLD Tension & Compression

In order to be able to evaluate the function of the new version of the USDFLD, a parametric study was performed, which investigated the application of different failure criteria for the routine. The model was analyzed with four different failure criteria applied. First, the single normal stresses S11, S22 and S33 were individually simulated. Afterwards the maximum shear stress was used as only failure criterion. From the failure prediction shown in Figure 5-14 it was expected that the simulations with S11 and S22 should give the most similar buckling behavior in comparison to the version of the USDFLD Tension & Compression, in which all stresses were checked for failure.

As mentioned before, the time consumption of the USDFLD Tension & Compression was higher than for the original version of the subroutine. The parametric study aimed at the reduction of time consumption without a significant reduction of accuracy. The results of the analyses are shown in Figure 5-15.

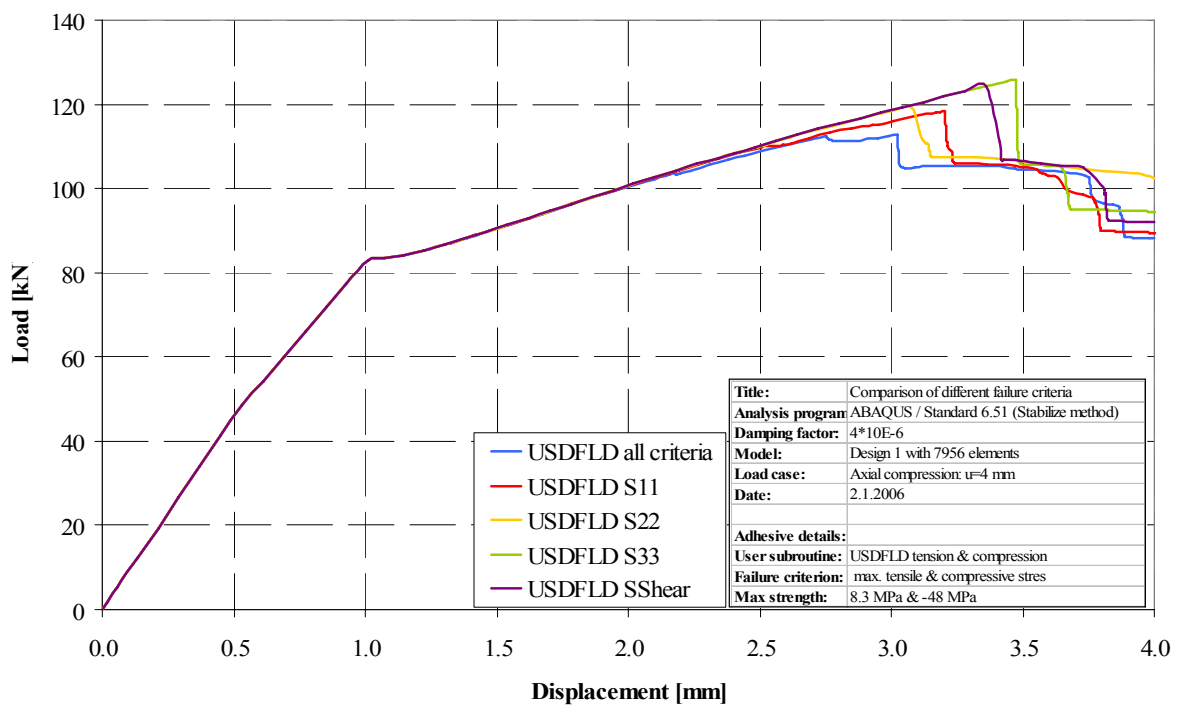


Figure 5-15 Comparison of different failure criteria for the USDFLD Tension & Compression

When only the stress S11 (red curve) was checked for occurring failure, the load-shortening graph showed very good agreement to the version with all failure criteria applied (blue curve), even in the deep postbuckling region. Collapse was predicted slightly later and the load-carrying capacity prior to collapse was predicted higher since the load-carrying capacity of the

original simulation was reduced at a shortening of approximately 2.75 mm. The same was valid for the simulation that used only the stress S22 as failure criterion, although its prediction of collapse corresponded better with the version where all failure criteria were applied. The next two single failure criteria S33 and SShear gave good prediction of the axial stiffness and the buckling behavior even at the beginning of the postbuckling region, but collapse was predicted significantly later than for the original version. Also the axial stiffness prior to collapse was higher. From the load-shortening graph it was concluded that the failure criteria that gave the closest prediction in comparison to the original version was the stress in 2-direction S22.

Besides the comparison of accuracy the second most important factor was the time consumption. Table 5-5 gives an overview of the computation time of the different versions of the USDFLD Tension & Compression. The data show that the simulation of S33 needed the longest computation time. In addition to the insufficient accuracy in the deep post buckling region this criteria did not seem to be useful to be applied as single criterion. The same was concluded for the shear stress criterion although the computation time was the shortest.

Failure criterion	Seconds [s]	Hours [h]
All criteria	56,566	15:42:46
S11	42,701	11:51:41
S22	21,638	06:00:38
S33	83,927	23:18:47
SShear	20,775	05:46:15

Table 5-5 Time consumption of USDFLD Tension & Compression for different failure criteria

From the load-shortening graph and the comparison of the time consumption it was concluded that the normal stress in 2-direction S22 was the appropriate failure criterion in order to give the most accurate prediction of failure in a short computation time. Of course this was valid only for this kind of panel under similar loading. Still, this subroutine with the specific failure criterion is only suitable for fast approximation analysis.

5.4 Development and application of the USDFLD Principal Stresses [6/21]

The next modification of the USDFLD was to use the principal stresses instead of the normal stresses to predict failure in the adhesive layer. This change was required because in the USDFLD Tension & Compression the prediction of failure depended on the chosen coordinate system in the simulation. As mentioned before this does not represent the physical context. In order to explain this development, a brief overview of the background of the principal stresses is given in the following section.

The normal stress tensor $\underline{\underline{S}}$ consists of the stresses that are parallel to the axis of the coordinate system. Equation 5-4 gives the stress tensor for the three dimensional and the two dimensional stress state (plane stress state).

$$\underline{\underline{S}} = \begin{bmatrix} \sigma_x & \tau_{xy} & \tau_{xz} \\ \tau_{xy} & \sigma_y & \tau_{yz} \\ \tau_{xz} & \tau_{yz} & \sigma_z \end{bmatrix} \quad \underline{\underline{S}} = \begin{bmatrix} \sigma_x & \tau_{xy} \\ \tau_{xy} & \sigma_y \end{bmatrix} \quad (5-4)$$

It is possible to calculate stresses in arbitrary sections under arbitrary angles through the considered body. It is known that both maximum and minimum stress values occur for one special angle φ . These different sections for plane stress are shown in Figure 5-16.

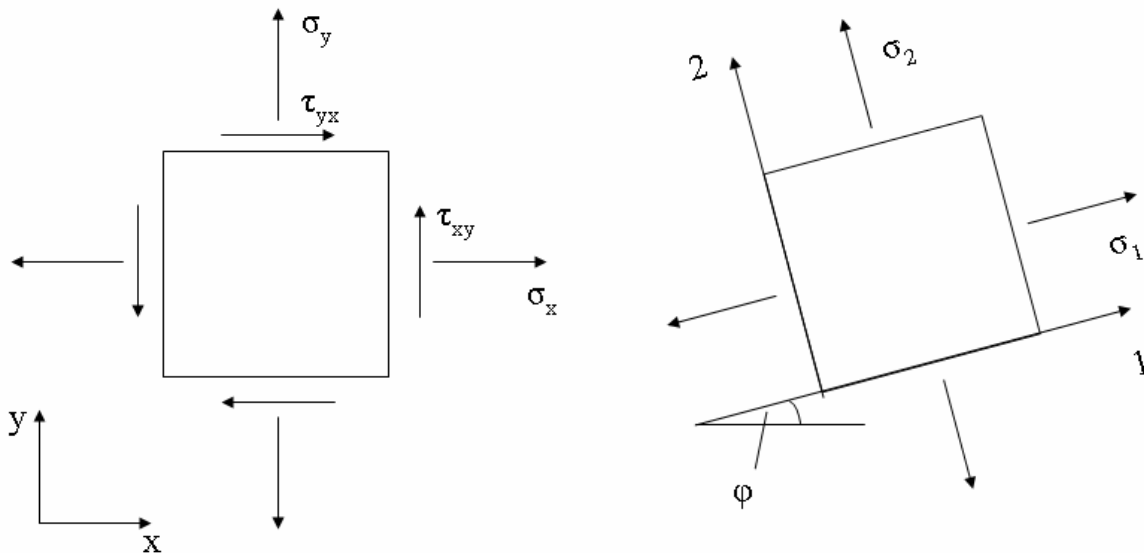


Figure 5-16 Example: Stresses in different coordinate systems for a plane stress state [21]

The maximum and minimum normal axial stresses are known as the principal stresses, and the planes at which they occur are known as the principal planes. At the principal planes, where the axial stress is a maximum or minimum, the shear stress will be zero. The value of the principal (maximum/minimum) stresses for the two dimensional stress state are given by:

$$\sigma_{1,2} = \frac{\sigma_x + \sigma_y}{2} \pm \sqrt{\left(\frac{\sigma_x - \sigma_y}{2}\right)^2 + \tau_{xy}^2} \quad (5-5)$$

For the three dimensional stress state the calculation of the three principal stresses σ_1, σ_2 and σ_3 is more complex. The complete derivation for the three dimensional state can be found in [6].

The graphical illustration of the three dimensional stress state including the principal stresses is given by Figure 5-17. The numbering of the principal stresses corresponds to the numbering in ABAQUS where $\sigma_3 \geq \sigma_2 \geq \sigma_1$. This does not agree with the usual numbering of the stresses a often found in the corresponding literature.

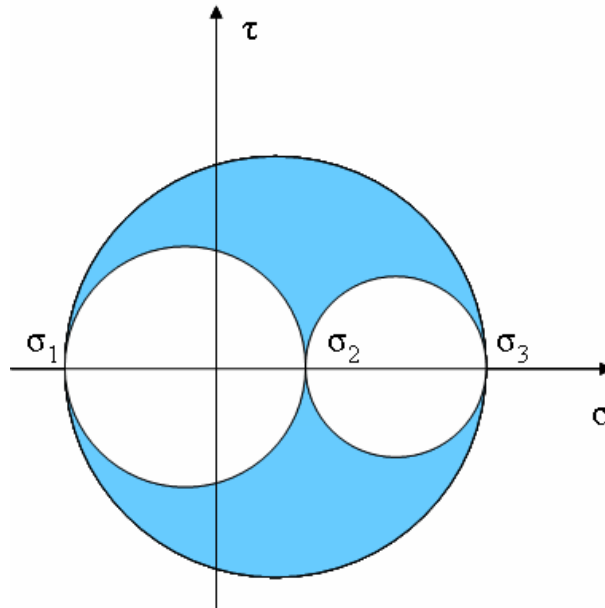


Figure 5-17 Illustration of principal stresses in 3D stress state [6]

The calculation is done by ABAQUS automatically and passed to the subroutine directly. From the theory was concluded that there were only two critical stresses that had to be checked for failure since σ_1 was always smaller than or equal to σ_3 and bigger than or equal to σ_2 . The new version of the USDFLD included the two principal stresses σ_1 and σ_3 and the maximum shear stress. It has to be mentioned that the maximum shear stress was in this case means the maximum of the three shear stresses S_{12} , S_{13} , S_{23} . This means that the shear stresses still depend on the coordinate system, which has no physical context as previously mentioned. A more detailed description of the subroutine code can be found in the Appendix A. The code was based on the previously developed USDFLD Tension & Compression, only the principal stresses are taken into account in the prediction of failure. The main reason why the principal stresses were used in order to predict failure was that the principal stresses are the highest occurring stresses in the adhesive. The other versions of the USDFLD always assumed that the element would fail in the direction of one of the axis of the coordinate system. The new version with the principal stresses takes all possible failure directions and angles into account and is therefore considered to give a more realistic prediction of failure than the other routines. Still, the shear stresses are not integrated in the correct way because the shear stress still depends on the coordinate system. The maximum shear stress calculated by

$$\tau_{\max} = \pm \frac{\sigma_3 - \sigma_1}{2} \quad (5-6)$$

should be examined as possible failure criterion. The results of this routine in comparison to the other versions of the USDFLD are given in Figure 5-18.

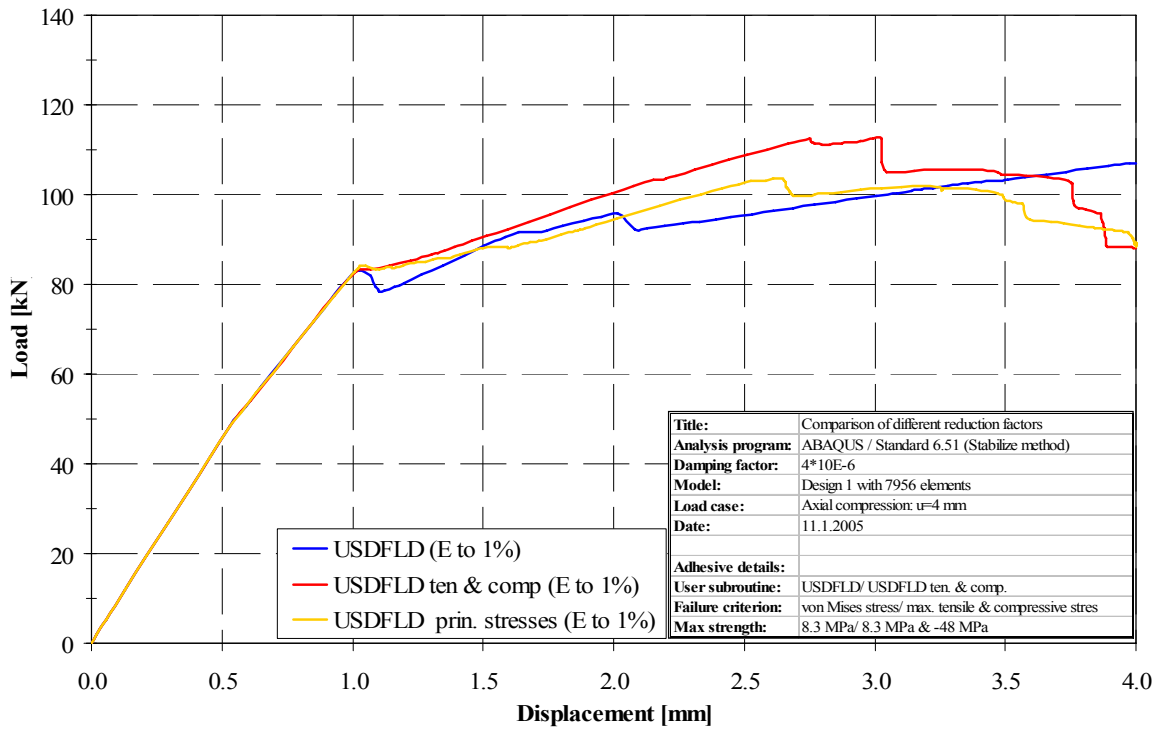


Figure 5-18 Load-shortening graph of all different versions of USDFLD

The first analysis performed with the new routine included a reduction of the Young’s modulus to 1% of the original modulus when failure occurred. This is represented by the yellow line in Figure 5-18. When comparing this progression to the USDFLD Tension & Compression with a reduction to 1%, the subroutine that used the principal stresses showed a significantly reduced stiffness after the onset of global buckling. Up to the point of global buckling, the subroutine predicted similar buckling behavior and stiffness as the simulations without any degradation and the other versions of the routine. In the entire region following global buckling, the curves progresses with a smaller slope.

It should be noted that the time consumption of the USDFLD Tension & Compression was generally higher than that for the original version and the USDFLD Principal Stresses. This was due to the extended volume of the subroutine code as more failure criteria were checked during each call of the routine. The time consumption increased dramatically when the Young’s modulus was reduced to 0.1% of the original. The analysis was manually stopped after 95 hours and 28 minutes when 97.3% of the analysis was finished. The time consumption for the USDFLD Principal Stresses was less than for the USDFLD Tension & Compression but a dramatic growth of computation time when the Young’s modulus was reduced to 0.1% was also witnessed. It was suspected that the numerous failure criteria in combination with the small Young’s modulus lead to numerical problems. Table 5-6 gives an overview of the different versions of the USDFLD, the applied failure criteria and the computation time. The original USDFLD was applied with the maximum tensile stress of 8.3 MPa as maximum allowable stress. This meant that all occurring von Mises stresses were compared to a maximum allowable stress of 8.3 MPa. The corresponding load-shortening graph is shown in Figure 5-10.

Also it should be noted has that the USDFLD Principal Stresses as programmed in this work has the potential for a reduction of computation time because the principal stress σ_3 is always higher than the principle stress σ_1 . Therefore it is only necessary to compare σ_3 to the maximum allowable tensile stress since if the element fails due to a exceeded failure criterion

in traction direction, it always fails due to the value of σ_3 . The same is true for the compression direction, respectively the maximum allowable compression stress and σ_1 . This gives the opportunity to exclude some of the failure criteria used in this work's version.

Additionally, the programming code included some weaknesses in the declaration of the second field variable that should be investigated and excluded in future version of the routine if it is concluded that the principal stresses are a suitable failure criterion for the adhesive layer.

Version of USDFLD	Failure criteria	Reduction of Young's moduls	Computation time [h:min:s]
Original	von Mises	0.1%	10:54:27
		1%	5:32:19
Tension & Compression	S11 S22 S33 SShear	0.1%	95:28:13 (at 97.3%)
		1%	15:42:46
Principal Stresses	SP1 SP3 SShear	0.1%	136: 50:11
		1%	11:58:12

Table 5-6 Comparison of different versions of the USDFLD

5.5 Summary of the parametric studies

The parametric studies that were performed in this chapter can be divided into three major fields, which all included different versions of the subroutines that were used to include degradation into the simulation model.

The first section focused on the analysis of the user subroutine UMAT implicit advanced that was previously developed [17]. The version of the UMAT implicit investigated in this work used the von Mises stress as failure criterion. The sensitivity of the subroutine to two specific parameters was investigated. PNEWDT was the first factor that was varied in order to detect the influence on the routine. The influence of PNEWDT was very small until the deep buckling region in terms of similarity and accuracy. In order to receive a short computation time a PNEWDT factor of 0.85 was recommended for all following simulations. The other factor investigated was the stress ratio that was used to steer the increment size of the subroutine. Six different stress ratios were analyzed and it was found that the stress ratio did not have a great influence on the prediction of buckling behavior of the panel itself. The main difference was the time consumption for the analyses that showed differences of more than 200%. Therefore stress ratios greater or equal to 1.08 were recommended for further simulations including this version of the UMAT.

The next section investigated the influence of changes in the geometry and the number of elements of the model. First, the adhesive thickness was varied in order to allow a better evaluation of possible manufacturing errors. Although the adhesive thickness showed influences on the panel behavior, this parametric study was considered of minor importance as the thickness of the adhesive was fixed during the manufacturing process and therefore more important from a design perspective. Next, the number of elements in the thickness direction was doubled in order to detect the influence of this parameter. Since only small differences in buckling behavior were predicted at approximately the onset of global buckling,

the influence was considered negligible. Especially because the time consumption was higher for the model with twice the number of elements in the adhesive, the original model with only one row of elements in thickness direction was recommended for further simulations. Finally, the influence of the number of adhesive elements in the axial direction was investigated. The number of elements was quadrupled. From the small changes in the load shortening graph it was concluded that the number of elements in the axial direction did not have a great influence on the buckling behavior and load-carrying capacity, although the computation time was increased dramatically. Still, the choice of the model used for the following simulations was not always conservative for example the nominal panel with 7,956 elements was chosen although the model with 31,824 elements predicted an earlier onset of global buckling (Section 5.2.3). Since the results of the chosen, more simple model were not always conservative in comparison to the results of the more complex model, these influences still should be considered in future simulation, although the deviations were small.

In the next section, the subroutine code of the USDFLD was modified in order to implement different failure criteria into the routine. The first modification was done in the USDFLD Tension & Compression that used the normal and shear stresses for failure prediction. Parametric studies were performed with this new version of the routine in order to validate its function by comparing its results to previous analyses with the original subroutine version. Also different allowable stresses were used as failure criteria and compared to other subroutine versions in terms of load-carrying capacity, buckling behavior, onset of element failure in the adhesive and time consumption. The sensitivity of this subroutine to the application of different failure criteria was investigated in terms of accuracy and time consumption. As mentioned before, in the version of the routine that used normal stresses, the prediction of failure depended on the choice of the coordinate system. Since this did not satisfy the physical context, the next modification was made by including the principal stresses as means of failure prediction to the subroutine. It was concluded that this version of the routine used the physically more comprehensible failure mechanism in comparison to the version that used the normal stresses and gave a more realistic prediction of adhesive failure compared to the USDFLD Tension & Compression. Still, it was not possible to decide which failure criterion was more realistic, the von Mises stress or the principal stresses. In order to receive a more realistic prediction of failure, it was considered necessary to investigate which stress based failure criterion suited the material behavior of the adhesive best.

In order to improve the user subroutines developed in this and previous works the involvement of the following parameters are recommended for future works:

- Extension of the subroutine code to improve the post processing possibilities concerning exceeded failure criteria and the number of failing elements
- Reduction of the code lines used in the USDFLD Principal Stresses by excluding unnecessary checks of failure criteria in order to reduce the time consumption of the analysis
- Involvement of the changes made in the USDFLD (i.e. principal stresses instead of Mises stress) in the UMAT explicit and implicit
- Involvement of more complex degradation models of different COCOMAT partners in UMAT explicit and implicit
- Development of new simulation model for example with two dimensional adhesive elements to avoid the problem of stress singularities

In order to receive a more realistic prediction of failure of the adhesive layer in the simulation, it is necessary to perform the following tasks:

- Literature review in order to investigate which failure criterion is the most realistic criterion for adhesives in general
- Implementation of the chosen criterion into the subroutine
- Analysis of the results including the new failure criterion and comparison of the results to the other user subroutines

6. Experiment

As described earlier the aircraft industry demands a cost reduction through the reduction of structural weight. Therefore high efforts are made in order to find new ways to reduce the structural weight by increasing the exploitation of structural reserves. This may not reduce the safety of aerospace structures. Therefore it is necessary to predict the structural responses with very high reliability. This comprises the coverage of real geometry, realistic loading conditions, accuracy of simulation and suitable material models as well as experimental validation of simulation tools.

One of the main goals of COCOMAT is to produce a validated approach to include the effects of material degradation in the analysis. This makes it possible to predict the collapse of the structure more accurately and through this to allow composite structures to be designed with some degradation permitted. The project focuses on the experimental investigation of skin-stringer debonding. In order to validate the numerical results experimental data is essential. Although the panels designed in the COCOMAT project have not been manufactured and tested yet, an identical panel from a separate project was tested at the DLR in Braunschweig. The results from this test were compared to the numerical simulation tools in order to improve these tools until the final panels are tested.

It is necessary to plan the required experiments very carefully to ensure a reliable and goal-orientated validation with respect to numerical analyses. Figure 6-1 gives an overview of modeling, simulation and the role of verification and validation in computational analysis. The “reality” or “experiment” has to be analyzed to obtain the “conceptual model”. This model represents the mathematical equations that are used to describe the physical system. These mathematical equations are coded to generate the “computer model”. The main focus of this work is the “model validation”, which links the “reality” and the “computer model”.

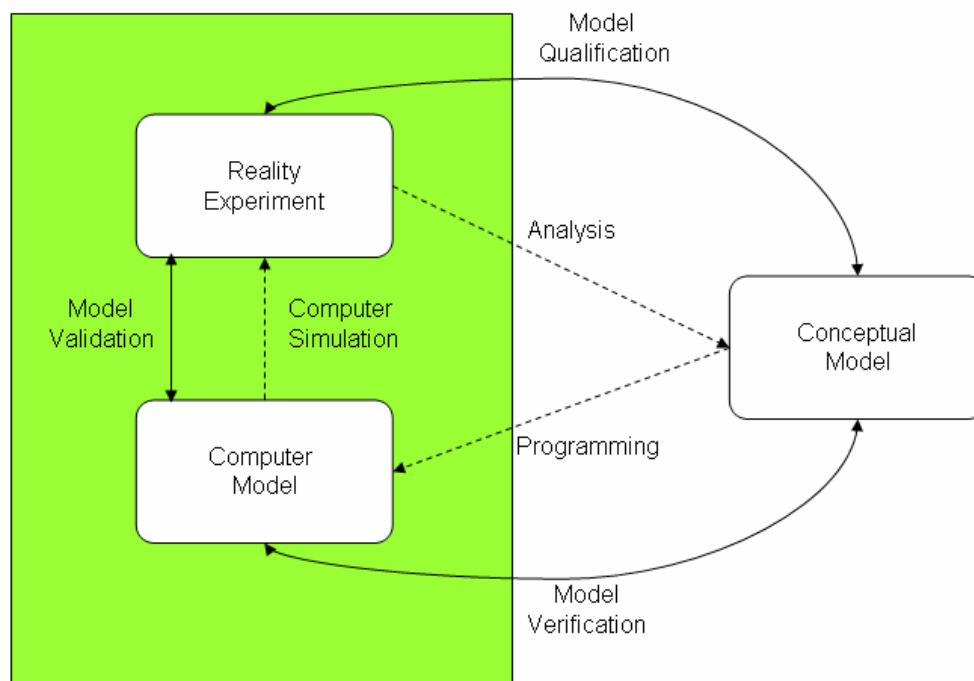


Figure 6-1 Phases of modeling and simulation [18]

The experiment as described in the following section was completed before this work was begun. Therefore in this work it was only possible to fall back on the observations made and data gathered by other scientists cooperating in the COCOMAT project.

6.1 Description of the experiment

The tested panel is shown in Figure 6-2. The panel was built up of the skin and five stringers oriented in the axial direction. Skin and stringers were manufactured separately and finally bonded using an adhesive. Before the panel was placed in the test facility, the upper and lower edge of the panel were sealed into blocks of epoxide resin and filler material. The height of these blocks was 60 mm. Usually, these edges are milled coplanar to ensure that the introduction of the force is homogenous. In the case of the panel P23, a panel similar to the COCOMAT panels, this step was omitted because the main reason for the production and testing of the panel was the testing of the measurement technique, mainly High Speed Aramis.

The main difference between the testing of the P23 panel and the testing of similar panels within the scope of the POSICOSS project is that no restraints were used on the lateral edges in order to prevent sidewise movement of the edges. The restraints were omitted because in the POSICOSS project it was shown that in the simulations the influence of the modeling of the lateral restraints on the axial stiffness in the postbuckling region was very high [23].

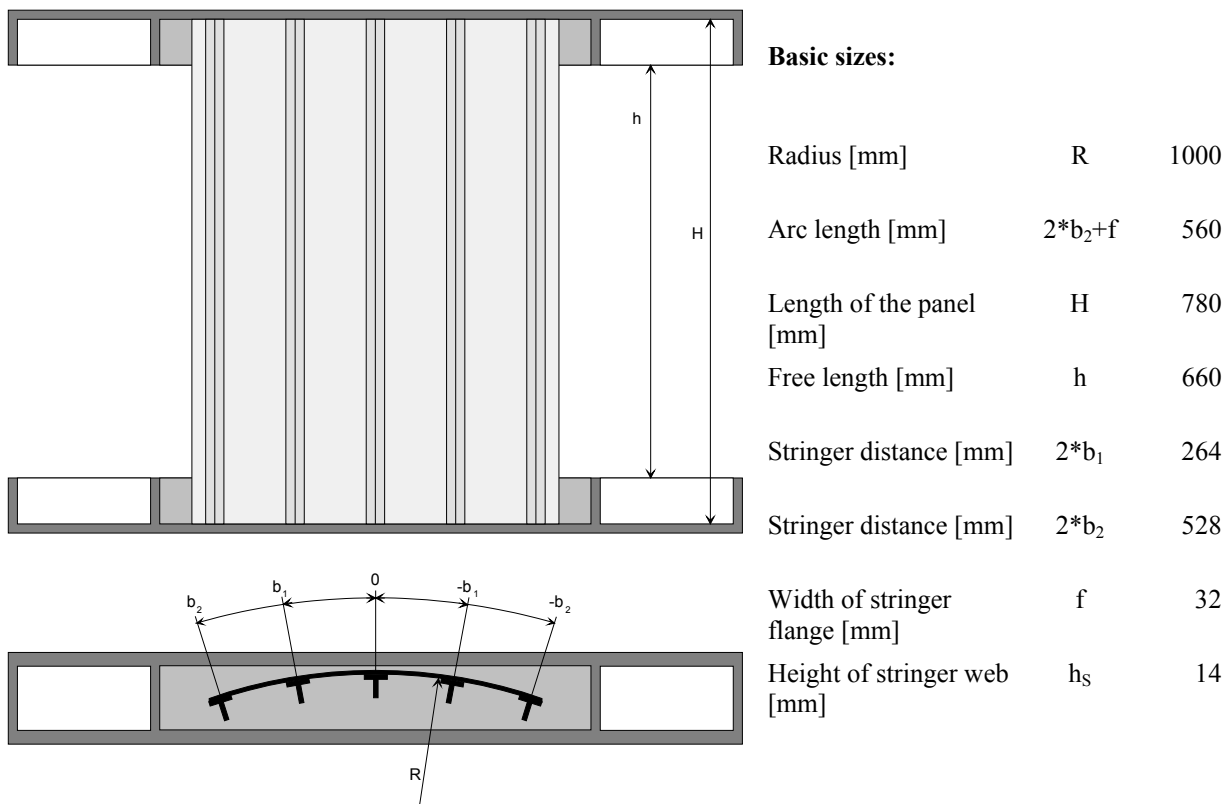


Figure 6-2 Basic dimensions of the tested panel P23 [14]

Although an experimental testing without any lateral restraints does not entirely represent the “reality”, meaning the panel as part of a cylinder representing a fuselage structure, DLR decided to test the eight panels designed by DLR without edge restraints.

The panels that will actually be tested within the scope of the COCOMAT project will be manufactured by Gamesa Aeronautica, a project partner from Spain. These panels will be tested at the DLR in Braunschweig in spring 2006. Gamesa has designed another panel for the COCOMAT project and four panels of this design will be also tested at the DLR. Edge restraints will be used during the testing of the Gamesa panels.

Prior to the final test, pre-test loadings were applied to settle experimental nonlinearities and to calibrate the measuring equipment. Afterwards, quasi-static loading was applied in displacement control until collapse occurred. After the occurrence of global buckling the loading was briefly stopped to inspect the panel. This explains the slight reduction in the panel load around at 1.34 mm axial compression that can be seen in the load shortening curve of the panel shown in Figure 6-7. Subsequent measurements were also performed.

During the experimental testing, the panel was placed into the buckle facility and only exposed to an axial compression load. This load was applied by a hydraulic cylinder that moved the lower constrained edges into the upper direction. The experiment was performed in displacement control. This means that a displacement of approximately 4 mm in the axial direction was applied quasi-statically. The term quasi-statically can be used because the time that passed during the application of the displacement was considerable, about 10 minutes with additional holding time to inspect the panel visually. Figure 6-3 gives two views of the panel P23 in the buckling facility. The left picture Figure 6-3a shows the panel during the testing from the skin side while the other picture Figure 6-3b shows the panel from the stringer side after collapse but still under loading.

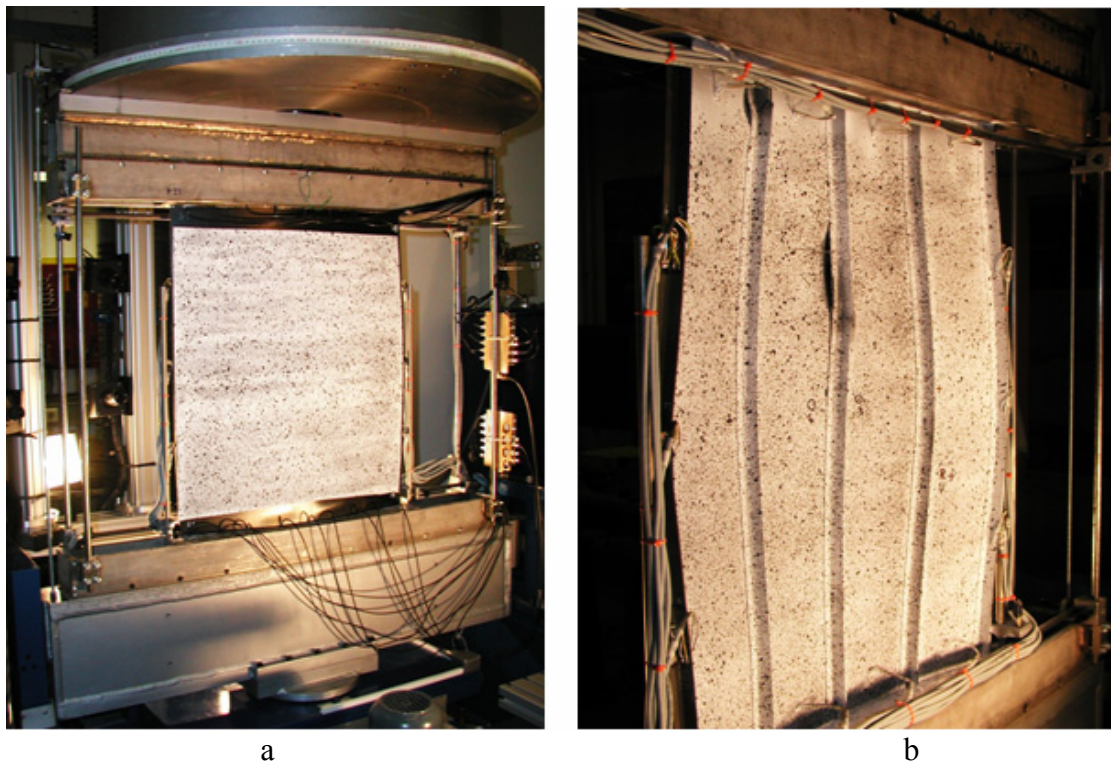


Figure 6-3 Panel in the buckling facility

6.2 Measurement technique [3]

In earlier experimental testing of panels under axial compression performed at DLR, strain gages were used to measure the strains and displacements. This had the disadvantage that the measuring data were restricted to the areas where strain gages had been applied during the test. In order to avoid this problem, in addition to strain gages a new measurement system was used to obtain and record data during the testing of the P23 panel. This system was called High Speed ARAMIS (Aramis), a new version of the optic measurement system ARAMIS. It is a non-contact optical 3D deformation measuring system, which is able to analyze, calculate and document material deformations. This measurement system can be used in a wide field of applications, for example material testing, component dimensioning and verification of FE models. A brief overview of some technical data of the Aramis system is given in Table 6-1. The following section describes the basic operating mode of Aramis.

Standard measuring volume in mm	25×20×15 to 1700×1360×1360
Camera resolution	1280×1024 points
Camera chip	1 inch, CMOS
Max. frame rate	480 Hz at 1280×1024 points 980 Hz at 1280×512 points
Intermediate image storage	On the frame grabber boards of the evaluating computer
Shutter time	0.010 ms up to 1s computer controlled, asynchronously triggerable
Strain measuring range	0.05% up to > 100%
Strain accuracy	Up to 0.02%
Measuring results	two dimensional or 3D displacements, strains and component contours

Table 6-1 Technical data of the Aramis system [3]

Aramis is able to recognize surface structures of the object to be measured with digital camera images and allocates coordinates to the image pixels. This is only possible if the object has many object characteristics. If the object has only a few object characteristics, such as the homogeneous surface of the V15 panel, it is necessary to prepare the surface, for example by applying a stochastic color spray pattern. Usually a white ground-coat is applied to the object and spots of black paint are applied on top of the ground-coat. In theory it is possible to apply the colors in reverse order but the black on white order is preferred in order to avoid reflections on the surface.

When Aramis records the reference condition, it already gathers the first coordinates. This image represents the undeformed or reference state of the object. Depending on the user input, further images are recorded after or during the deformation process of the object. Afterwards, Aramis automatically compares the images of the deformed shape with the reference images of the reference shape and calculates the displacements and deformation of the object characteristics.

For a 3D measurement setup, a pair of cameras is needed that has to be calibrated before the actual testing. As mentioned earlier, Aramis takes images in various load steps. The definition of the so called computation mask, the area that is to be evaluated, and the starting point is possible directly with the camera images.

For the comparison of the deformed state and the reference state so called facets are required. Facets are square or rectangular image details. When calculating the measurement project, Aramis observes the deformation of the project through the images by means of these facets. The facet can be identified because they all have individual gray level structures of the individual pixels within the corresponding facet.

Figure 6-4 and Figure 6-5 show a pair of facets with the size of 15×15 pixels of the right and the left camera of a camera pair. The green values were observed through six stages, where stage 0 is the undeformed reference state and stage 5 is the final deformation state. The white dashed line visualizes the undeformed state. It can be seen that in Figure 6-4, the white line agrees with the edge of the two facets. In the next picture, Figure 6-5, the white dashed line does not match with the edge of the facet anymore. This is due to the deformation of the object under loading.

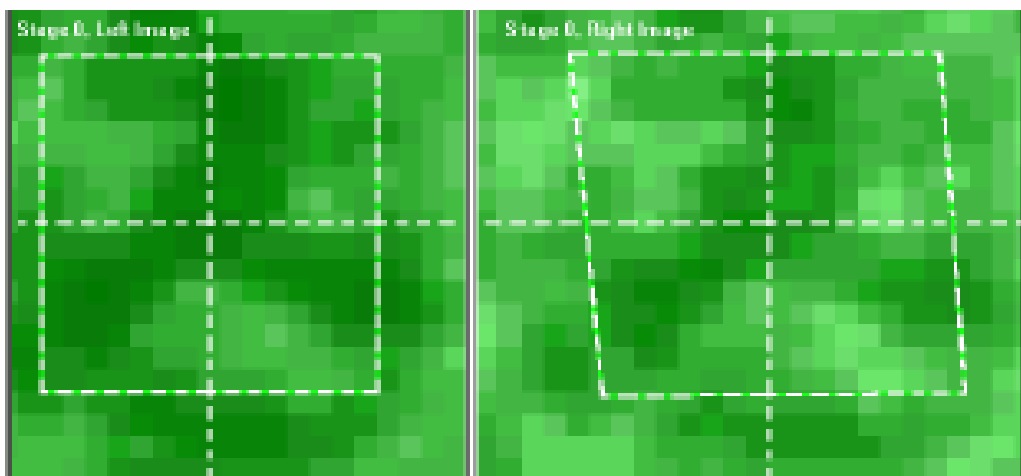


Figure 6-4 Undeformed reference state

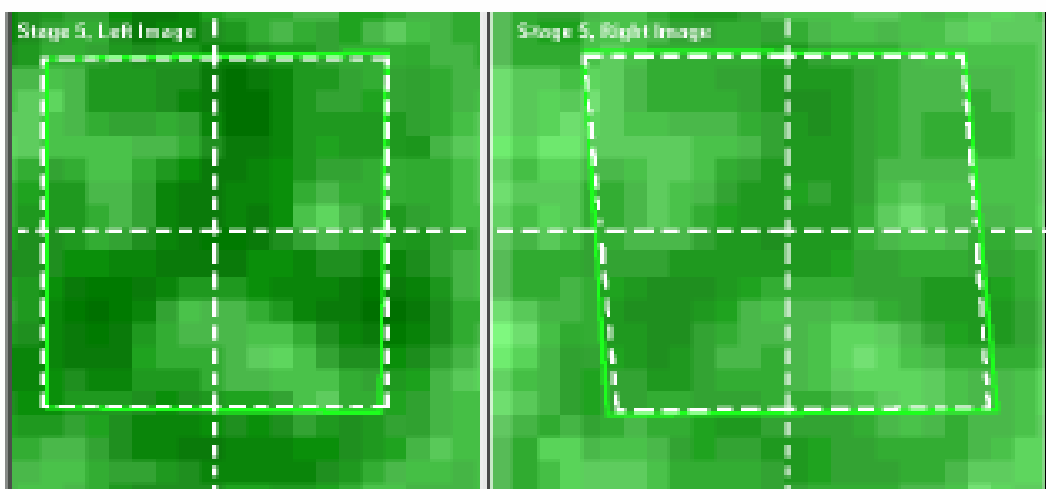


Figure 6-5 Final deformation state

Aramis determines the two dimensional coordinates of the facets from the four corner points of the facets and the resulting centers of the facets. It is possible to calculate 3D coordinates

by using photographic methods to connect the two dimensional coordinates of the left camera with the two dimensional coordinates of the right camera of the same facet.

The fast digital cameras used by the Aramis system are able to take up to 1000 images per second. When the systems are coupled they can enable measurements up to 4000 images per second depending on the quality of the object illumination.

For the experimental testing of the panel P23, which was similar to the COCOMAT panels that have to be manufactured and tested yet, four pairs of cameras were used to record the measurement data. One was positioned on the skin side of the panel, the other three on the stringer side. In order to record the most area-wide experimental data, one camera was placed frontal to the skin side and one camera was positioned frontal to the stringer side of the panel. Since the panel was curved, it was not possible to record the entire stringer regions with the frontal camera pair because the inner part of the stringers was not visible. Therefore the two additional camera pairs were added to be able to receive measurement data from the stringer regions. They were positioned under an angle on the left and the right side of the central frontal camera pair on the skinner side. Unfortunately, one of the side-camera pairs broke during the experimental testing.

6.3 Description of the experimental results

In order to compare the results of the experimental testing to the results of the performed simulations, the results of the testing are discussed in detail in the following section. Within the scope of this description the load-shortening curve and the deformation patterns were taken into account.

The experimental deformation pattern of the P23 panels that is given in Figure 6-6 shows local buckling of 15 longitudinal half sine waves per stringer bay at an axial compressive loading of 0.51 mm. The deformation pattern was slightly asymmetric. This was indicated by the different colors of the panel, where one side was moving towards the center of curvature (blue), the other side moving away (red).

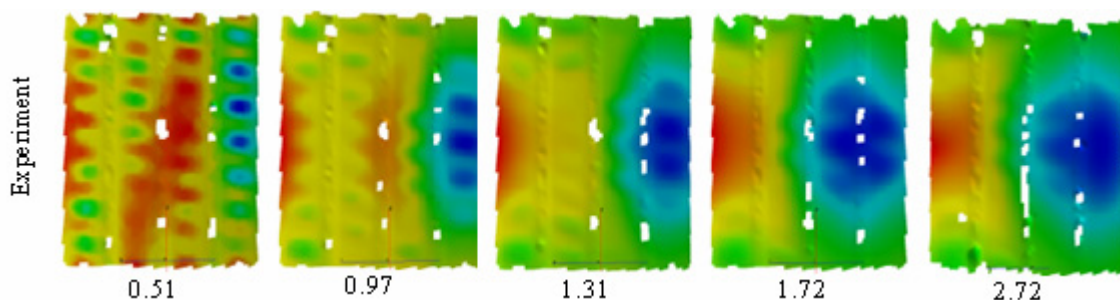


Figure 6-6 Experimental deformation patterns at various values of axial compression [mm], view facing the stringer side: red/yellow→outward displacement, blue/green→inward displacement

The first global buckling occurred at a shortening of about 0.97 mm. This can be seen in Figure 6-7 as the curve progression shows a reduction in load-carrying capacity. The shortening of 0.97 mm corresponded to a loading of 74.4 kN. At this point the deformation pattern showed two global buckles in the outer stringer bays. These buckles were again orientated inwards and outwards. Therefore the deformation pattern was considered asymmetric.

From the load shortening graph it was concluded that another global buckling shape developed at an axial shortening of about 1.72 mm. Again, this was represented by the declension of the curve progression. The deformation pattern at this shortening showed that the inward global buckle grew to the adjacent inner stringer bay.

The collapse of the panel occurred at a shortening of 2.71 mm or a load of 83.6 kN. This was characterized by the reduction of the load carrying capacity of the panel represented by the high declension of the curve progression in the load shortening curve. The collapse was also accompanied by a high level of noise. The deformation pattern at the shortening of 2.72 mm shows the two global buckles, the right, blue one moving inwards, the left, red one moving outwards. The pattern is highly asymmetric.

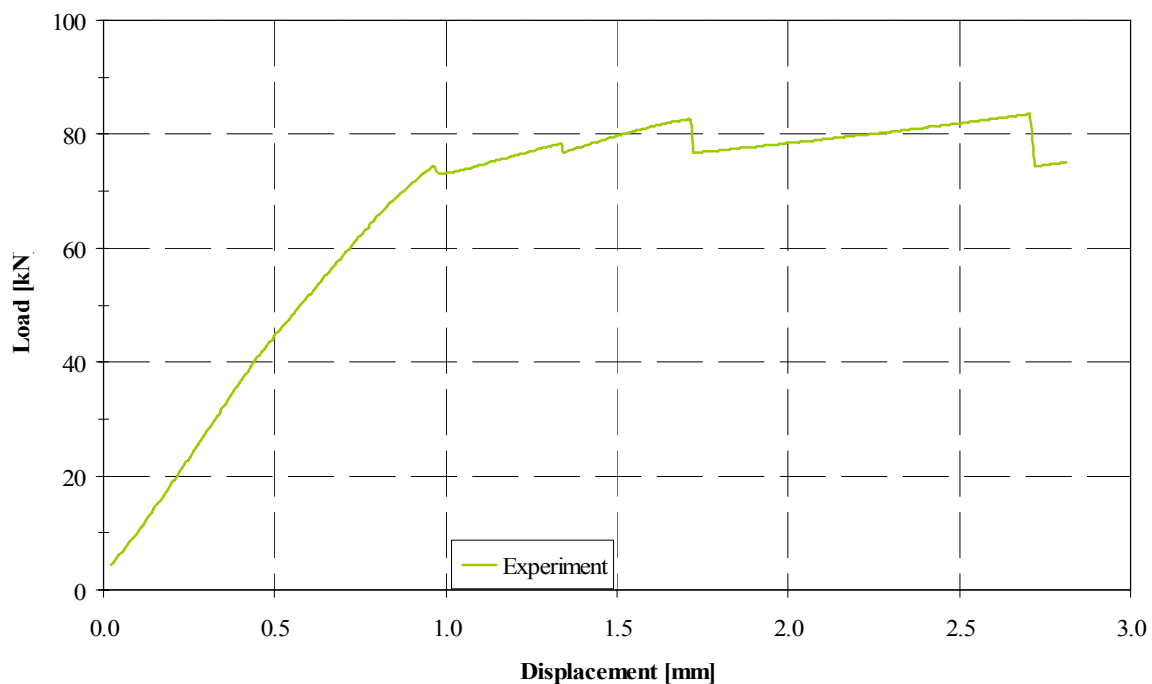


Figure 6-7 Load-shortening curve of the experimental testing of panel P23

After collapse, the panel was removed from the buckling facility and a visual inspection was performed. The panel showed several different composite damage mechanisms such as fiber fracture in the stringer blade and flange and matrix cracking in the skin as well as in the stringer blade and flange. Delaminations were located between the skin and the stringers and between ply groups in the stringer blade. It was assumed that the collapse of the panel was most likely due to fiber fracture across the stringer blade in the center of the left stringer number 5. The numbering of the stringers refers to Figure 7-3. Stringer 5 is located at the edge of the outward global buckle. Regions of separation between the stringer and the skin were located at the center of the middle stringer (stringer 3) and close to the potting in the left inner stringer (stringer 4) on the non-loading side. In these areas, the stringer buckled away from the skin. This can be seen in Figure 6-3.

6.4 Comparison of experimental and numerical prediction without degradation

Figure 6-8 shows the load shortening curve of the experimental testing (blue curve) and the analysis with ABAQUS without inclusion of degradation (black curve). When comparing the ABAQUS model without degradation to the experiment, the solution gave good prediction of the initial stiffness of the panel. This can be concluded from the similar slope of the load shortening curves at shortenings smaller than approximately 0.5 mm. The local buckling mode shapes represented in Figure 6-9 show good similarity at a shortening of about 0.51 mm as well, although the experimental tested panel already showed asymmetric buckling as shown in Figure 6-6. The prediction of the initial postbuckling stiffness was also very similar, although the first global buckling load of the experiment was less than the one predicted by the analysis. As mentioned earlier, global buckling occurred at a shortening of 0.97 mm during the experiment, but during the simulations global buckling did not occur until 1.04 mm for the model without degradation.

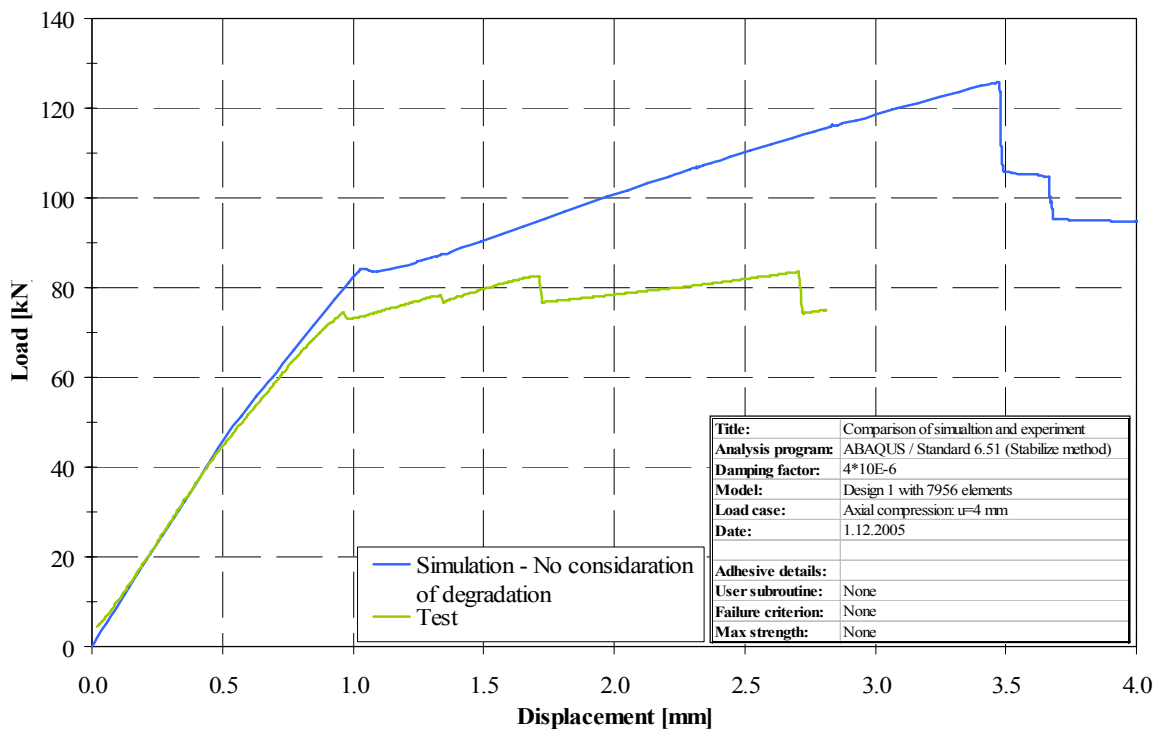


Figure 6-8 Comparison of experimental and simulation data

The main difference between the experiment and the simulation was that the simulation failed to predict the asymmetry in the experimental deformation pattern. The model predicted an initial postbuckling mode shape of two global buckles in the outer stringer bays. These two buckles both went inwards, and the asymmetric inward and outward deformation pattern of the experiment was not seen in the numerical results.

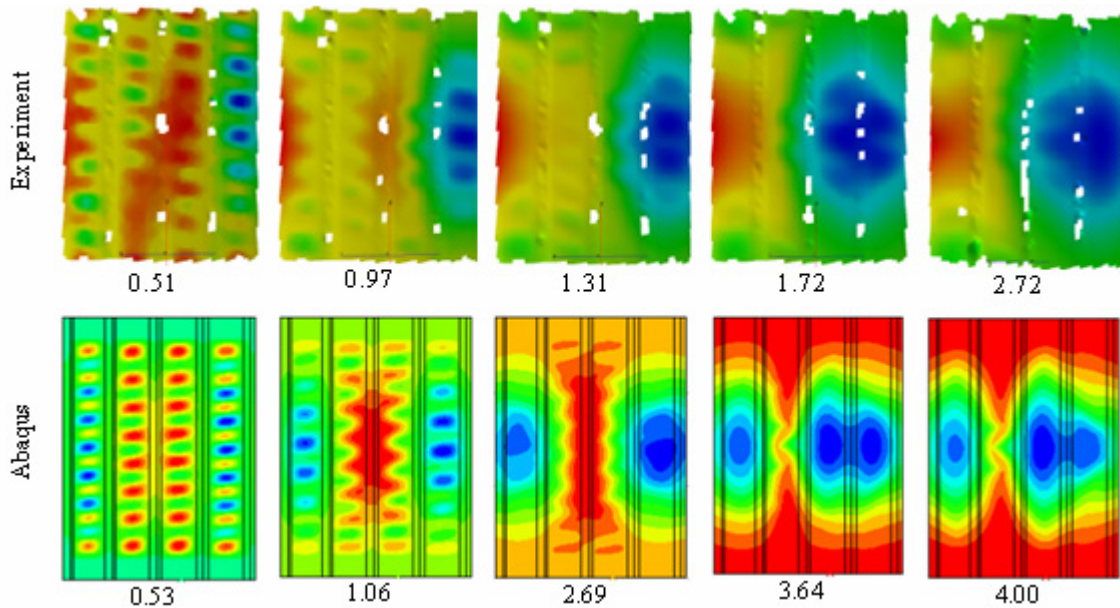


Figure 6-9 Experimental and numerical deformation patterns at different values of axial compression [mm], viewed facing the stringer side [13]

The panel underwent a secondary mode shape change in the simulation and the experiment. This means that not only the magnitude of the deformation but the entire mode shape changed. This is expressed by the reduction of the stiffness that is represented by the slope of the curves in the load-shortening graph. This secondary mode shape change occurred at a shortening of about 1.72 mm in the experimental testing and at approximately 3.48 mm in the ABAQUS simulation.

The new mode shape was characterized again by two global buckles but the buckle of the right side changed its shape into a wider, planer buckle. Although this mode shape was predicted, the simulation failed again to predict the asymmetry of the experimental buckling. The lack of asymmetric buckling behavior of the simulation panel can be assumed as one of the reasons for the differences in loading and axial compression in terms of stiffness, secondary mode shape changes and prediction of collapse.

Additionally the prediction of the debonding of skin and stringer that was made by the ABAQUS simulation did not meet the results of the experiment because the debonding of the skin and stringer was only visible after the panel had collapsed. This was although cracking could be heard prior to global buckling, indicating that some damage was occurring. This assumption was made for the comparison of the simulation without degradation and the experiment. The comparison of the model with degradation included and the experiment is presented in Chapter 7.

6.5 Conclusions

The ABAQUS simulation model gave relatively good prediction up to the onset of first global buckling but only fair prediction in the postbuckling region. Although the buckling shape of the experimental tested panel showed slightly asymmetric characteristics even in the area of local buckling, the stiffness of the simulation model was very similar to the experimental data until the onset of global buckling. Still, global buckling was predicted at higher loadings for the simulation in comparison to the experiment.

The most significant factor affecting the numerical simulation was the inability to predict the asymmetry of the buckling shapes of the tested panel. There are numerous possible reasons for this inability. The panel was assumed to be sensitive to shape changes at the panel edges such as bending and warping that can be caused by the manufacturing process. Since the panel was tested without any longitudinal support on the edges, it is possible that these geometric imperfections have an influence on the buckling shape of the panel. This theory is supported by the fact that even in the local buckling modes, a slightly asymmetric displacement pattern was found.

A second reason for the asymmetric buckling shape might be the variation of the stringer width. Although it is not very likely that layers of fiber were forgotten during the manufacturing process, there have been panels previously tested at DLR where the results of the experimental testing and the simulation did not agree well due to several layers being left out in one of the stringers during the manufacturing process.

A third reason for the asymmetric buckling shape of the panel during the experiment may be due to an asymmetric introduction of load. This might be caused by the potting edges not being totally parallel since the coplanar milling of the potting edges was omitted.

7. Numerical Simulations and evaluation of additional aspects

The main goal of this section was to investigate the influence of different parameters on the buckling behavior of the panel. All simulations including geometric imperfections of the geometry of the model, the evaluation of the strain gage data of the experiment and the evaluation of the user subroutine were all performed in the face of the asymmetric buckling behavior of the experimental tested panel.

7.1 Results of eigenvalue buckling analysis introduced as geometrical imperfections

This type of analysis is performed to estimate the critical load of a “stiff structure”. Stiff structures are defined as structures that carry their design loads primarily by axial or membrane action, not by bending action. They show very little deformation to applied loading prior to buckling. Even if the response of a structure is nonlinear to prior collapse, a general eigenvalue buckling analysis can provide useful estimates of collapse mode shapes.

This method is usually used in the investigation of the imperfection sensitivity of structures. In this analysis, the load for which the model stiffness matrix becomes singular is looked for. The buckling mode shapes are the most useful outcome of this kind of analysis because they predict likely buckling modes of the structure. Eigenvalues are also calculated. These eigenvalues multiplied with the applied load and added to any previous “base state” loading are the predicted buckling loads.

The option used in ABAQUS to perform a buckling analysis is indicated by *BUCKLE. In this step the number of eigenvalues that is to be calculated has to be specified. The command used in the input file is

```
*BUCKLE
10, , , 50
```

where the first number is the number of eigenvalues to be estimated and the second number represents the maximum eigenvalue of interest. The next two numbers are related to the course of iteration. For a more detailed description see [1]

It has to be mentioned that eigenvalue buckling analysis only provides a reliable estimation for the buckling load if the assumption of small geometric changes and linear elastic material response prior to buckling are realistic for the modeled structure.

The next step after the eigenvalue buckling analysis is the nonlinear postbuckling analysis. Here an imperfection based on the buckling mode is imposed. This is done using the *IMPERFECTION option in ABAQUS. The lowest buckling eigenmodes are assumed to provide the most critical imperfections. Therefore these eigenmodes are scaled and added to the perfect geometry to create the perturbed mesh. The command line used in the ABAQUS input file is:

```
*IMPERFECTION, FILE=buckling_analysis, STEP=1, NSET=skin
1, 0.1
```

The result file `buckling_analysis` contains the results of the buckling analysis, this means the node coordinates of the different mode shapes. The NSET parameter is optional and is used to import eigenmode data for a specified node set. If this parameter is omitted, the eigenmode data is introduced to the entire model. In the next line, the first number represents the number of eigenmode that is introduced and the second number is the scale factor. This means that the imperfection is scaled as a function of the magnitude 1. In this case, 0.1 means 10% of the skin thickness.

In order to investigate the sensitivity of the D1 panel to imperfections of the skin, numerous analyses were performed with different buckling shapes and scale factors. As an example Figure 7-2 shows the results of three different analyses. The analysis without any imperfections is represented by the blue curve, the first eigenmode as imperfection with a scale factor of 0.1 is shown by the red curve. This mode was chosen because there was no buckling mode calculated during the buckling analysis that looked more similar to the original buckling mode of the panel without imperfections.

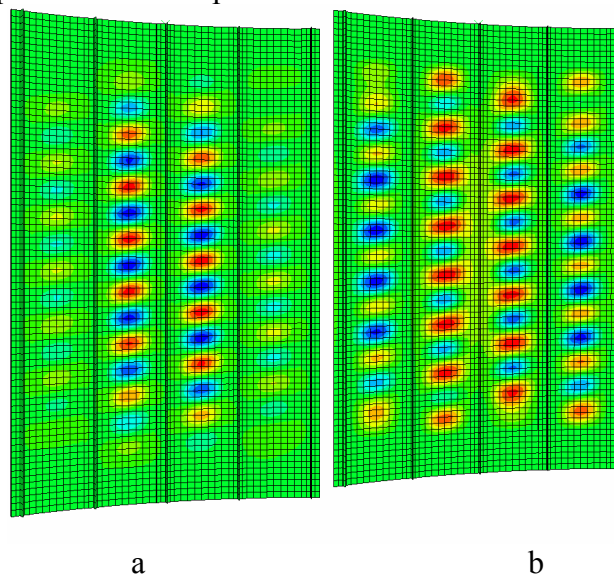


Figure 7-1 Buckling mode shapes of the first eigenmode and the original calculation
Inward displacement→blue, outward displacement→red

These two buckling shapes are shown in Figure 7-1. On the left hand side, the buckling shape of the first eigenmode is shown, on the right hand side the original buckling mode at a shortening of 0.6312mm is shown. The third curve showed the behavior of a model with an introduced imperfection consisting of the first five superimposed buckling modes. This model was chosen because imperfections consisting of only a single buckling mode tend to yield non-conservative results. Therefore the introduction of an imperfection consisting of several superimposed buckling modes was assumed a safer way to test the sensitivity of models to skin imperfections. The weight of the buckling modes is to be chosen by the user, usually the lowest buckling modes should have the largest weight. In this case, the five eigenmodes all was assigned a magnitude of 10% of the skin thickness.

The axial stiffness of the panel was very similar up into the deep postbuckling region. The model with the imperfections of the single eigenmode turned out to be a little less stiff than the original model at a shortening of approximately 0.5 mm, at the onset of local buckling. The stiffness of the model with the superimposed buckling modes also showed a reduced stiffness in comparison to the two other models. The prediction of global buckling was also very similar especially for the original model and the model with the single mode imperfection. The two models predicted global buckling at a shortening of 1.02 mm. The third

model predicted the onset of global buckling at the slightly higher shortening of 1.09 mm. The reason for this might be that due to the introduction of skin imperfections, the energy needed for the model to buckle in its “natural” shape was higher than in the other models. This meant that because imperfections were introduced, the buckling shape was slightly different to the original model.

This was concluded from the difference in the load-shortening graph prior to global buckling. If the buckling modes differed in such a way that buckles occurred at different locations or maybe the panel buckled even in different directions, the result might be a later onset of global buckling because it took the model longer to buckle in the pre-assigned shape. In the course of the analyses these minor derivations could be considered negligible.

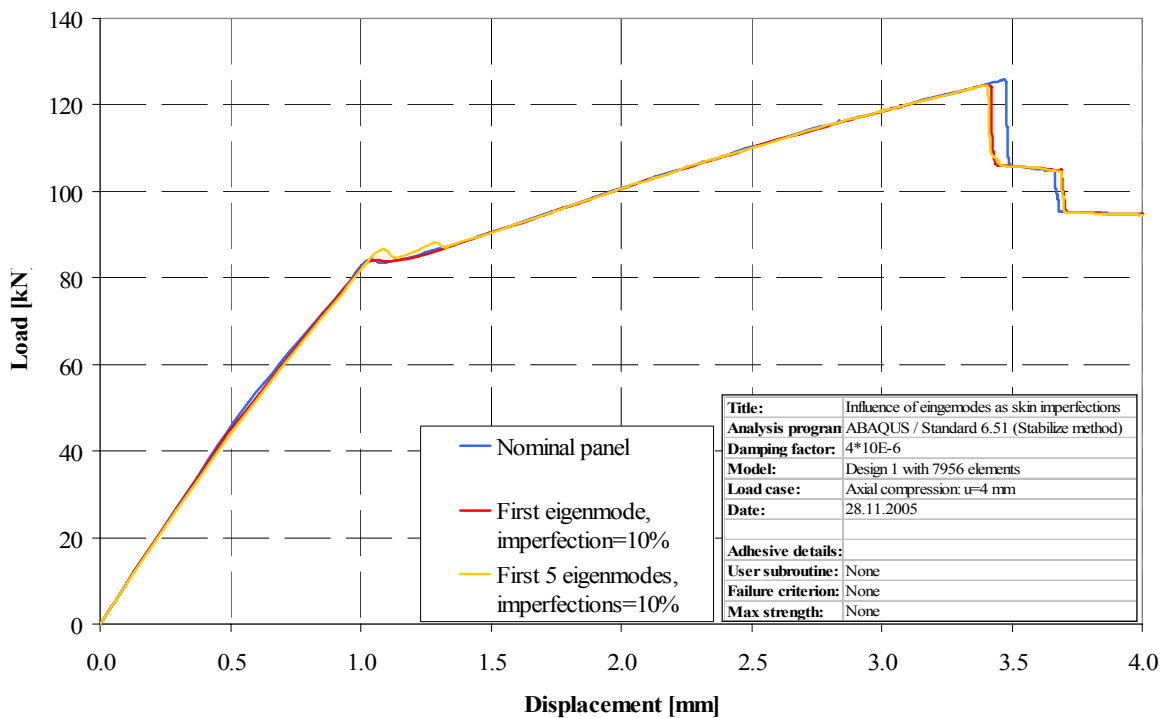


Figure 7-2 Load-shortening curve of the P23 panel with and without skin imperfections.

The three curves showed very similar behavior even in the deep postbuckling region. Although there were small differences in the onset of global buckling and collapse, the three models all buckled into the same shape. This is shown by the good similarity of the load-shortening graph, especially when after collapse the load-carrying capacity of the three models was reduced to the same value, represented by the similar horizontal lines.

From these simulations it was concluded that the panel was not sensitive to imperfections in the skin and that skin imperfections were not very likely to cause asymmetric buckling as shown by the panel during the experimental testing. The buckling shapes looked very similar to the original simulation as shown in Figure 6-9. They showed the characteristic two inward buckles and therefore an almost symmetric buckling shape.

Although the panel did not show sensitivity to skin imperfection, it is advisable to take this kind of imperfection into account in future simulations in order to receive the most accurate simulation results. With the Aramis measurement system it is possible to measure and calculate the skin imperfections prior to the buckling test. To date, it is not possible to trace this measurement data into an ABAQUS model directly. This is a complicated process

because the mesh has to be synchronized. If the measurement data after the introduction of loading is required, the synchronization of the incrementation between Aramis and ABAQUS represents another problem. The DLR has started a cooperation with a software company which aims to develop a software tool that is able to solve these problems so that the effects of geometric imperfections can be taken into consideration more easily for future simulations. This tool might be especially useful for the testing of shells without axial stringers because this kind of geometry is more sensitive to imperfections of the skin than stiffened structures.

7.2 Variation of the stringer thickness

In order to receive the asymmetric buckling mode that was shown by the experimental testing of the panel P23, an investigation considering the width of the stringer was performed. From the experiment it was concluded that the left side with the outward buckle showed weaker structural performance than the right side with the corresponding inward buckle. In order to take this structural weakness into account, plies were removed from the left side of the panel and added on the right side of the panel.

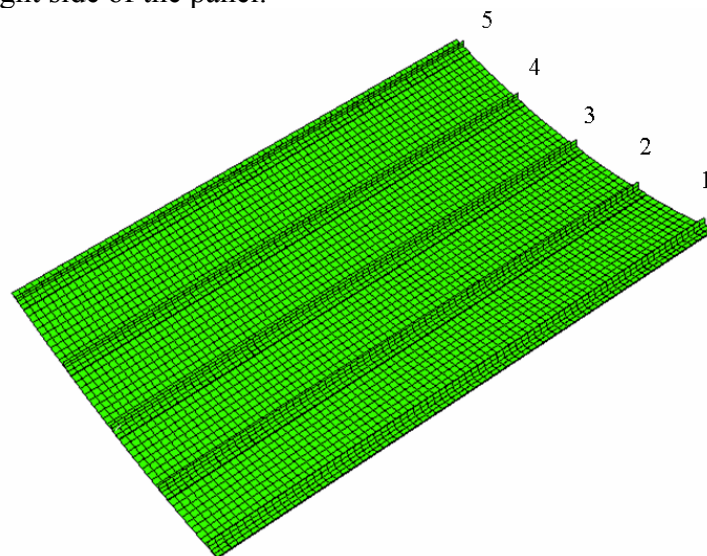


Figure 7-3 Panel geometry and stringer numbering

Figure 7-3 shows the panel and the numbering of the stringers. Three different models were created to evoke an asymmetric buckling shape. In the first analyzed model, only two 0° layers were removed from stringer 5 on the left hand side in order to weaken the structure at this point. The result of this analysis is shown in Figure 7-4. The original calculation with no reduction in the stringer lay up was represented by the blue curve. The red curve was the modified panel. The load-shortening curves looked very similar up to global buckling although a very slight reduction of axial stiffness could be seen prior to global buckling. The differences in the onset of global buckling were also very small. As expected the occurrence of collapse was predicted earlier for the panel with the reduced stringer lay up.

The second modification of the panel was done by removing two 0° layers from stringer 5 and adding two 0° layers to stringer 1 on the other side of the panel. This model is represented by the gold line in Figure 7-4. Up to global buckling the axial stiffness is very similar to the original model. This was understandable because the number of plies in the model was not changed, only the location of the layers. The onset of global buckling and the stiffness afterwards was predicted very similar to the original model. Only the occurrence of collapse

were predicted earlier at a shortening of 3.35 mm in comparison to the original model that did not predict collapse until 3.48 mm. Collapse was predicted even earlier than for the first modified model that collapsed at a shortening of 3.40 mm.

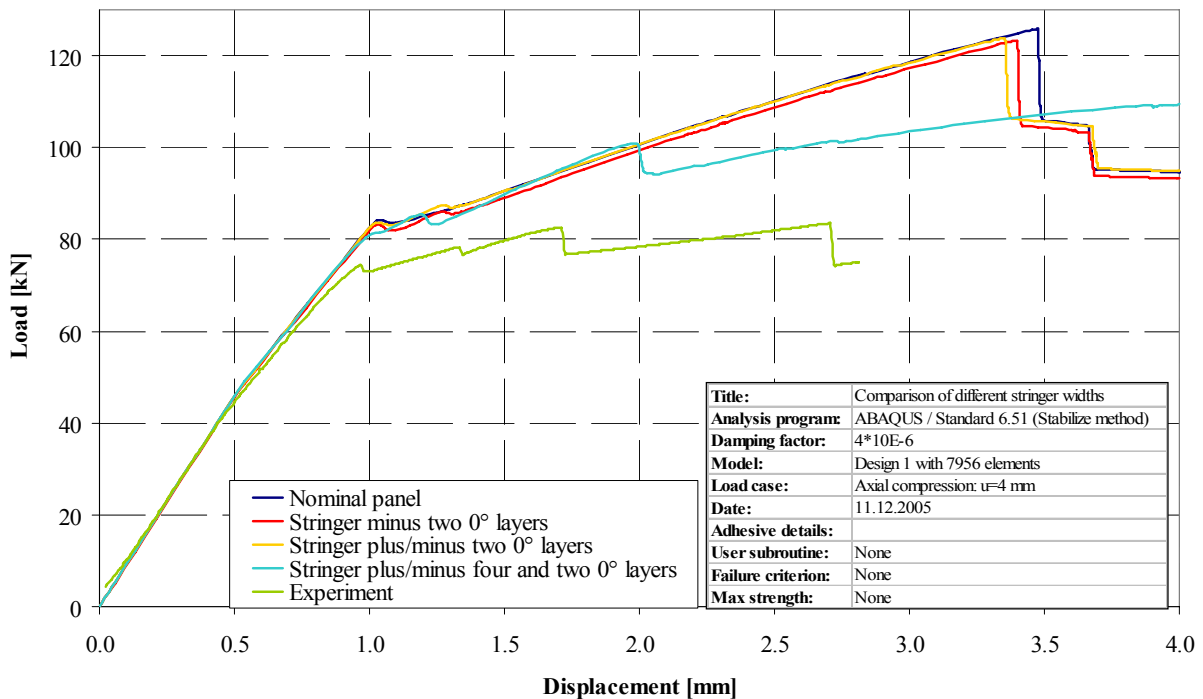


Figure 7-4 Load-shortening curves of models with different stringer widths

The last modification of the model was more significant than the earlier changes. Four 0° layers were removed from stringer 5 and two 0° layers were moved from stringer 4. The lay up of the middle stringer 3 was not changed but two 0° layers were added to stringer 2 and four 0° layers were added to the outer stringer 1. This means that the left outer stringer 5 only contained eight 0° layers while the outer stringer on the other side, stringer 1, contained 16 layers under 0° . This is a difference of eight layers. The neighboring stringers contained ten 0° layers on the left hand side in comparison to twelve 0° layers on the right hand side, a difference of four layers. Only the stringer in the middle, stringer 3, contained the original number of 0° layers, namely twelve.

The buckling behavior of this modified panel is also shown in Figure 7-4 and represented by the light blue curve. The axial stiffness of the panel was very similar to the previous simulations up to the point of global buckling. The modified panel did not show a strong reduction of the load-carrying capacity as the three other panels did at a shortening of 1.01 mm, although the modified panel showed a reduction of stiffness by a reduced slope of the load-shortening graph. After global buckling, the stiffness of the panel was slightly higher than the stiffness of the previous simulations up to a shortening of approximately 2 mm. At this axial displacement, the load-shortening graph showed a strong reduction of load-carrying capacity in contrast to the constant slope of the previous simulations. This reduction was due to the asymmetric build up of the panel. After the change of the buckling mode, the slope of the load-shortening graph was nearly constant up to the final displacement of 4 mm. In comparison to the other simulations, the stiffness was reduced in this area up to the point, where the other panels experienced collapse with the corresponding reduction in load-carrying capacity. The stiffness of the modified panel was then predicted higher than the previously simulated panels.

When comparing the results of the numerical simulations to the results of the experimental testing it was concluded that the first two attempts to change the numerical model to cause an asymmetric buckling shape. The first two load-shortening graphs are very similar to the panel without any imperfection, which did not meet the criteria of an asymmetric buckling shape as described in Chapter 5. This can also be concluded from the buckling shapes of the panels shown in Figure 7-5.

As it was expected from the load-shortening graph, the first two panels (Figure 7-5 a and b) showed very similar buckling modes and these buckling modes were also very similar to the simulation of the nominal panel. The shapes show the typical two inward buckles, where the buckle on the right side was slightly stronger and bigger than the buckle on the left side.

In contrast to this high similarity, the last panel showed a buckling mode that did not agree with the previous simulations (Figure 7-5 c). Instead of the two inward global buckles, it showed only one inward buckle in the middle of the panel. In the middle of the two outer stringers, the panel showed outward movement of the structure in contrast to the previous simulations, where these regions also moved inward as the global buckles. Therefore it was concluded that the significant changes in the stringer widths showed a great influence on the buckling behavior of the panel that lead to a new buckling shape in contrast to the previous simulations.

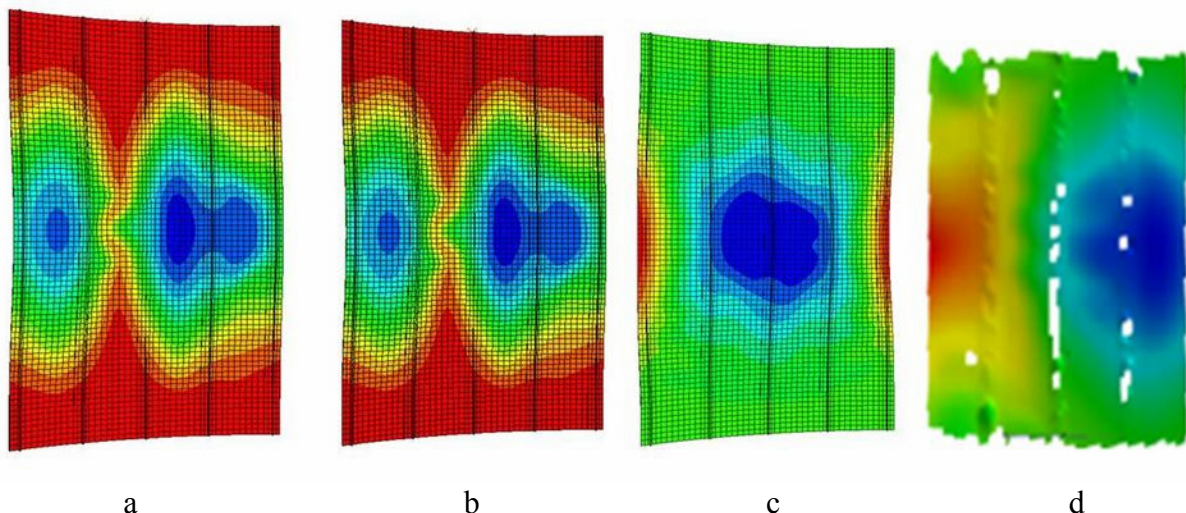


Figure 7-5 Buckling modes of the three modified panels and the experiment

It was possible to evoke a different buckling shape of the panel by changing the stringer lay up but when comparing this new buckling shape to the buckling shape of the experimentally tested panel, it became clear that the buckling modes were not very similar. This is shown in Figure 7-5, which allowed a comparison of the buckling shapes of the three modified panels and the experiment. The shortening of 4 mm was chosen for the three simulated panels because the final buckling shapes of the experiment and the analyses were to be compared. The buckling shape of the experiment was taken from a shortening of 2.72 mm.

The significantly changed model predicted one inward buckle as was shown in the experiment, but the location of the buckle was predicted in the middle of the panel, not on the right side as in the experiment. The location of the outward buckles shown by the analyzed model did not fit the tested panel as well. They were also predicted more concentrated in the middle of the panel in contrast to the experimental tested panel that showed outward movement of the structure almost over the entire length of the panel.

In conclusion, none of the simulations were able to predict an asymmetric buckling shape as was shown by the experimental tested panel. The first two modifications of the panel, namely to reduce and extend the stringer lay up by only two 0° layers, did not show any significant influence on the buckling behavior. The third modification included more significant changes and successfully changed the buckling behavior of the panel, though the predicted buckling shape was not asymmetric. The simulation of the first two modified models did have practical interest because it was not impossible that during the manufacturing process, slight errors in the stringer lay up were made. Although the stringer widths were measured, it was possible because the thickness of the layers was only 0.125 mm that the lack of one or two layers was not detected at first. This situation had occurred in previous DLR tests when it turned out that the unsatisfying agreement between experimental and simulation data was due to the fact that in one of the stringers two layers of fiber were missing. This was only detected after the combustion of the corresponding stringer.

The numerical analysis of the panel of the third variation of the stringer lay up was only of theoretical interest because it was very unlikely that several significant mistakes were made during the manufacturing process of the panel. Also, the changes in the stringer lay up that were included in this model were very likely to be detected during the measuring process of the stringer widths that was performed as part of the routine measurement procedure prior to the test and after the test. The analysis of this panel was mainly performed to evaluate the sensitivity of the panel to changes in the stringer width.

Concluding from the comparisons above, it was not very likely that a dissimilarity in the stringer width caused the panel P23 to buckle asymmetrically. Still, it might be possible that the variation of the stringer width over the length of the panel caused the asymmetric buckling behavior. The width of the stringer web was measured for each stringer over the panel length and it was found that the width was not constant. For future investigations it would be useful to measure the variation of the stringer width with an accurate measurement system and to introduce the deviations as geometrical imperfections into the model. Because the panel did not show a high sensitivity to imperfections of the stringer web, the introduction of the deviations was not considered very likely to be responsible for the asymmetric buckling shape. Still, simulations aim at using models that are as close as possible to the experimental tested panel. Therefore the further investigation of stringer imperfections is considered useful.

7.3 Results of asymmetrical load introduction introduced as geometrical imperfections

In the next attempt to receive an asymmetric buckling shape, two concentrated loads were introduced on nodes located at the lateral edges of the panel. The simulation run with the concentrated forces was the first analysis in this attempt. The load on the right side of the panel was introduced in the negative direction of the 1-axis, meaning radial, while on the left side of the panel the concentrated force was directed in the positive direction of the 1-axis. Therefore the load on the right side was negative, and the load on the left side was positive. The model with the loads and the corresponding coordinate system is shown in Figure 7-7.

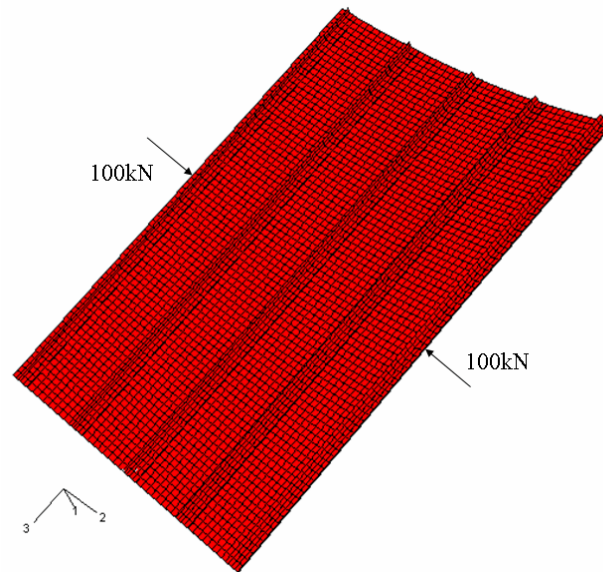


Figure 7-6 Panel with two concentrated loads introduced on nodes on the lateral edges

The magnitude used for the concentrated forces was 100 kN. The loads were introduced on the skin nodes in the middle of the two lateral edges in order to evoke an asymmetric displacement of the panel edges. The background of the introduction of concentrated loads in the way it was done in this simulation only had theoretical background because no loads were introduced during the experiment. The resulting displacement of the edges under an asymmetric loading of 100 kN is shown in Figure 7-7. The values were taken from the first increment of the analysis. The resulting displacements u_1 were written into the fil.-file using the *NODE FILE function of ABAQUS.

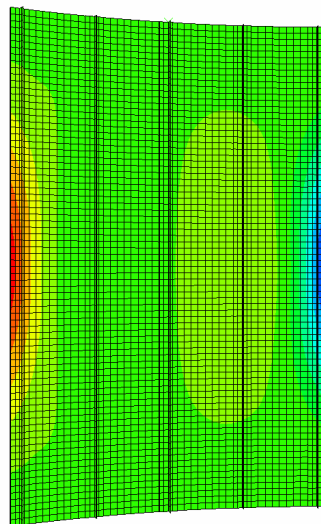


Figure 7-7 Displacement in the 1-direction under asymmetric loading of lateral edges

In the second analysis the resulting displacements from the first simulation including the concentrated forces were then read from the fil.-file and introduced as a geometric imperfection on the nominal panel. The *IMPERFECTION function of ABAQUS was used for the introduction of the displacement in the same manner as was used for the introduction of different eigenmodes as geometric imperfection in Section 7.1. The corresponding code lines in the input file were:

```
*IMPERFECTION, FILE=result_file, STEP=n, INC=m
```

1, scale factor

The result_file represents the fil.-file with the corresponding resulting displacements. The step was the step in which the analysis was performed. Since the analyses of the panel consisted of only one step, this variable had to be set to 1. INC was the abbreviation for increment. It represented the increment of the first analysis with the concentrated forces for which the displacements were introduced. As mentioned earlier in this case the first increment was chosen, therefore m was set to 1. In the second line, the only factor that was to be changed by the user was the scale factor. In the case of introducing the results of a STATIC analysis, the scale factor was defined as a percentage of the total displacement calculated in the previous analysis.

Numerous analyses were performed with the same displacement shape introduced into the perfect geometry of the nominal panel, with a variety of different scale factors used. A total of seven different scale factors were used, namely 10%, 20%, 30%, 40%, 50%, 80% and finally 100%. At first, only three scaling factors 10%, 50% and 100% were used but it was not possible to make valid conclusions from the resulting buckling behavior. Therefore the other four scale factors were added in order to gain a better understanding of the influence of this factor. Figure 7-8 gives an overview of the displacement of the simulations in the second increment of the analyses. These figures show how the imperfection was increased and influenced the displacement, even in this early stage of the analyses.

Figure 7-9 shows the influence of the asymmetric displacement of the panel depending on the different scale factors. The three curves with the smallest scaling factor, the red (10%), the yellow (20%) and the green curve (30%) show very similar behavior to the nominal panel. The differences in axial stiffness up to global buckling are negligible. In the postbuckling region the results are also very similar, the only differences are the onset of collapse that was predicted slightly earlier for the models with imperfections.

When the scale factor was increased, the buckling behavior of the panel changed significantly. Although the stiffness of the models up to the onset of local buckling still was very similar, the stiffness of the models with the higher scale factors was reduced in comparison to the models with the smaller scale factor after local buckling occurred. Also the prediction of global buckling was changed. The model with a scale factor of 40% (pink curve) showed the highest deviations as shown in Figure 7-9. Therefore it is described in more detail in the following paragraph.

In this model, global buckling did not occur at approximately 1.01 mm but at approximately 1.24 mm. This represented a deviation of 18.5% in comparison to the nominal panel. After the onset of global buckling, the curve showed a declining progression, this means that the stiffness of the panel was predicted higher directly after global buckling and afterwards started to decrease. This was the first time in all simulations performed that the panel showed this kind of buckling behavior. In all other analyses, the curves showed approximately linear progression after global buckling.

The simulation with a scale factor of 40% showed the latest prediction of global buckling but also the highest stiffness in the postbuckling region. When the scale factor was increased, the curve was shifted towards smaller values of loading but kept their shape. The other main difference to the simulations with smaller scale factors was that all simulations with more than 30% imperfections did not predict a collapse point up to a shortening of 4 mm. There was no change in their buckling mode after global buckling.

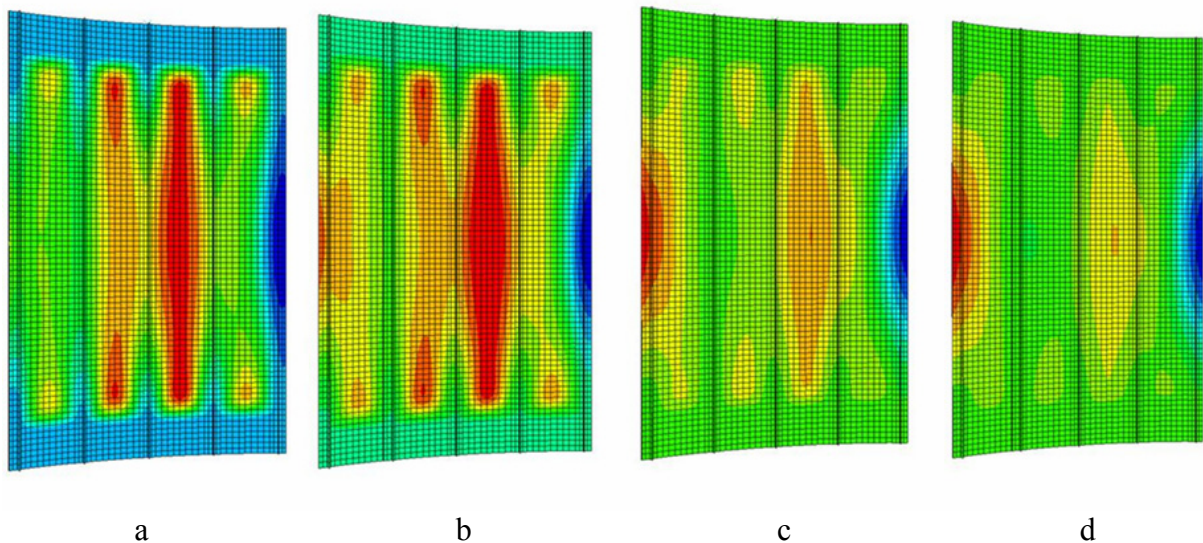


Figure 7-8 Buckling shapes of the second increment with introduced imperfection
 a. 10% imperfection b. 20% imperfection c. 50% imperfection
 d. 100% imperfection

When comparing the pink curve with the results of the experiment (green curve) it was concluded that the two curves progressed entirely differently. The experiment showed global buckling at a shortening of approximately 0.97 mm instead of 1.24 mm. Also the entire progression of the curves was different because the experiment showed two more changes of buckling mode after the onset of global buckling at approximately 1.71 mm and 2.7 mm while the simulated panel kept the same buckling shape up to the maximum displacement.

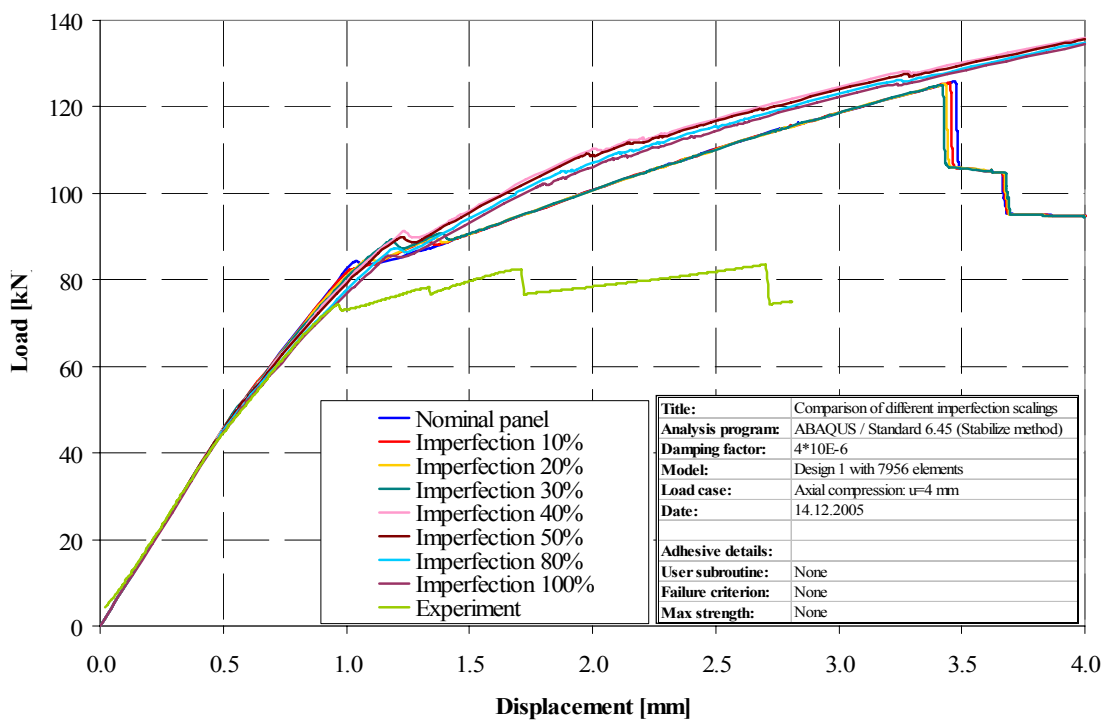


Figure 7-9 Load-shortening graph of different imperfection scale factors

From the load-shortening graph it was expected that the buckling shapes of the models with scale factors less than or equal to 30% were very similar to the buckling shapes of the nominal panel. This is supported by Figure 7-10 a, which shows the buckling shapes of the nominal

panel in comparison to the buckling shapes of the panel with different scale factors and the results of the experimental testing (Figure 7-10 d). Two scale factors were chosen to represent the two groups of buckling shapes, namely 10% (Figure 7-10 b) and 100% (Figure 7-10 c). Figures 7-10 a-c were taken from the simulation results at a shortening of 4 mm while the buckling shape of the experiment was the final shape at a displacement of 2.72 mm. These four buckling shapes are the final buckling shapes of the corresponding panels.

The buckling shapes of the Figure 7-10 a and b were very similar with the two characteristic global inward buckles. This was expected because of the similar progression of the load-shortening curves. In contrast to these buckling shapes, Figure 7-10 c showed a different shape. The panel showed the influence of the introduced imperfection even at a shortening of 4 mm. The left side was shifted outward while the right side was shifted inward the same way the imperfection was introduced in the second increment (Figure 7-7). In contrast to the previous analyses, the panel showed a strong inward buckle on the left side, located between the stringers 3 and 4 and a smaller outward buckle in the center of stringer 2.

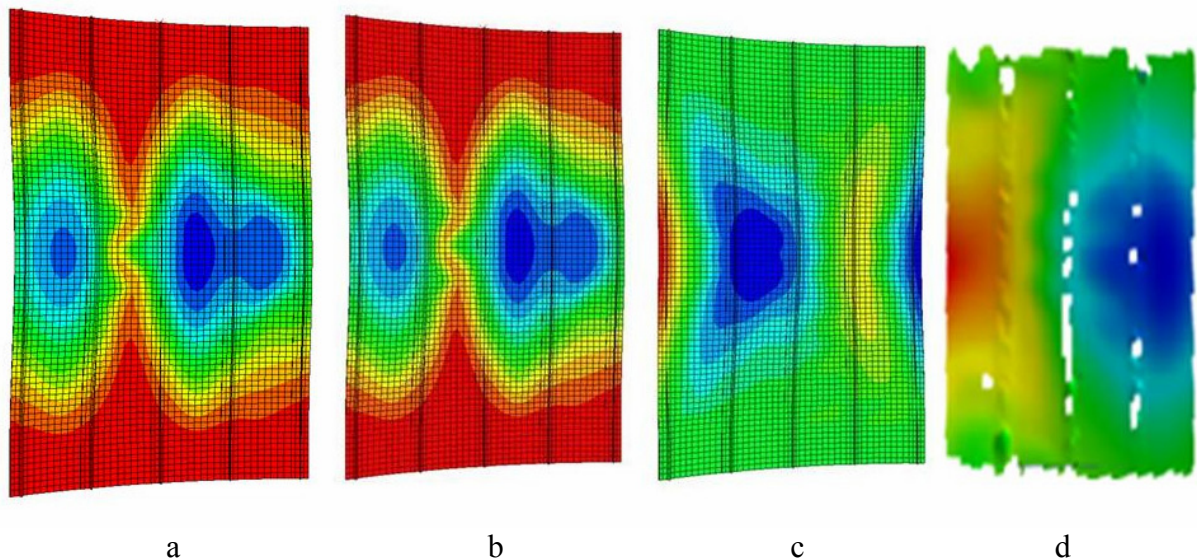


Figure 7-10 Buckling shapes of nominal panel, panels with different scaling factors and experiment
 a. Nominal panel b. Imperfection 10%
 c. Imperfection 100% d. Experiment

When comparing the buckling shapes to the experiment, Figure 7-10 a and b did not show similar behavior as was already discussed in previous sections. Also, the buckling shape of the third panel did not compare well with the experimental testing. Although asymmetric loading and as such asymmetric displacement was introduced in the form of a geometric imperfection, the panel did not show the asymmetric buckling that the experiment did.

In conclusion, the attempt to introduce geometrical imperfection due to asymmetric loading did not lead to the asymmetric buckling shape shown by the experiment. The entire postbuckling behavior of the panel changed but did not show any similarity to the experimental testing. It has to be mentioned that the idea of introducing concentrated forces only had theoretical background because during the experiment, there was no such loading introduced. However the strong differences in buckling behavior in the investigation of the panel behavior under this kind of imperfection lead to the conclusion that the panel was sensitive to this kind of imperfection, even if it was not possible to evoke the desired buckling shape.

7.4 Curved lateral edge

The next attempt to create an asymmetric buckling shape of the simulation panel was to add an imperfection in the form of a change in the shape of the lateral edge. The geometry was changed in such a way that the left lateral edge was more curved than the right edge. In this case the imperfection was introduced into the geometry of the model in Patran. Figure 7-11 shows the panel with the changed lateral edge. The imperfection was added in the form of a function on the first ten rows of nodes counting from the left edge of the panel. The function had to satisfy the following three prerequisites:

1. Its amplitude had to be zero at the upper edge of the panel ($s=0$ mm)
2. Its amplitude had to reach its maximum at the middle of the panel ($s=390$ mm)
3. Its amplitude had to be zero at the lower edge of the panel ($s=780$ mm)

In order to satisfy these three prerequisites the following sine-function was chosen:

$$f(s) = \sin\left(\frac{s}{l} \cdot \pi\right)$$

where s was the coordinate of the axial direction of the lateral edge with its origin on the bottom side of the panel and l represented the full length of the panel of 780 mm. This function was now added on the rows of nodes on the left side of the panel in such a way that the panel was curved more strongly in the outward direction. This was done to decrease the strength of the structure at this location and reduce the load-carrying capacity.

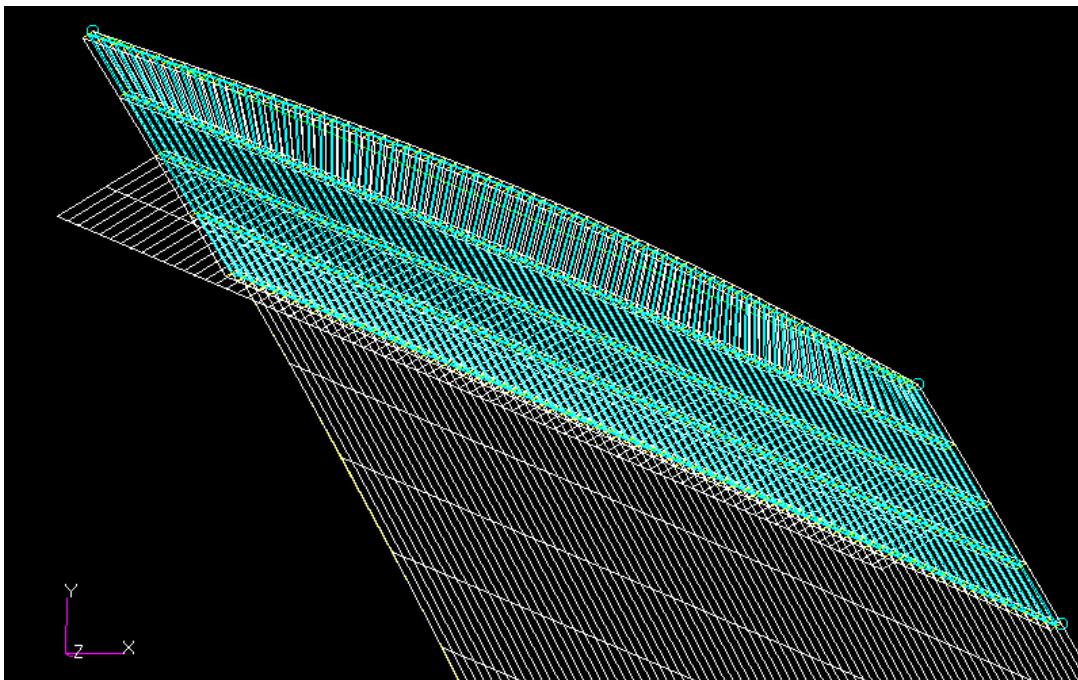


Figure 7-11 Panel with imperfection on left lateral edge

The idea was that if the structure of the panel was weaker on the left side and already curved more strongly in the direction it was supposed to buckle under loading, the panel would produce an asymmetric buckling shape. This attempt was supported by the manufacturing process because during the production when the panel was taken out of the autoclave it had a tendency to slightly warp. This was considered a possible reason why the structure was weaker on one side of the panel. This structural weakness was simulated by the addition of an imperfection of the lateral edge in form of the described function. Although the entire panel

showed the tendency to warp, the imperfection was only added on the left side of the panel because in the previous simulations the right side showed the inward buckle it was supposed to show in comparison to the experiment.

The maximum amplitude of the function was chosen for the outer row of node and was set to 1 mm at the r-coordinate of 390 mm. The same function was added to the next nine rows of nodes but the maximum amplitude in the middle of the panel was decreased by 0.1 mm for every row of nodes. The results of the analysis are shown in Figure 7-12.

The graph shows that the prediction of axial stiffness up to global buckling was very similar for the nominal panel (blue curve) and the panel with the imperfection on the lateral edges (red curve). In contrast to the nominal panel, the reduction of load-carrying capacity predicted by the modified model was not as strong, although it showed a reduced stiffness after global buckling. Another difference between the two models was that although both panels underwent two changes of buckling shape after global buckling, the modified panel did not predict a collapse point up to a shortening of 4 mm.

In comparison to the experiment the modified panel showed a higher stiffness after the onset of local buckling. As mentioned earlier, the simulation did not predict a proper onset of global buckling while the experiment showed the corresponding reduction in the load-carrying capacity at a shortening of 0.97 mm. Afterwards the progression of the curves looked similar with the results of the experimental tested panel located at a lower load, and both panels underwent two changes in buckling shape. In contrast to the modified panel, the tested panel experienced a sharp reduction of load-carrying capacity due to structural collapse and therefore changed buckling shape again.

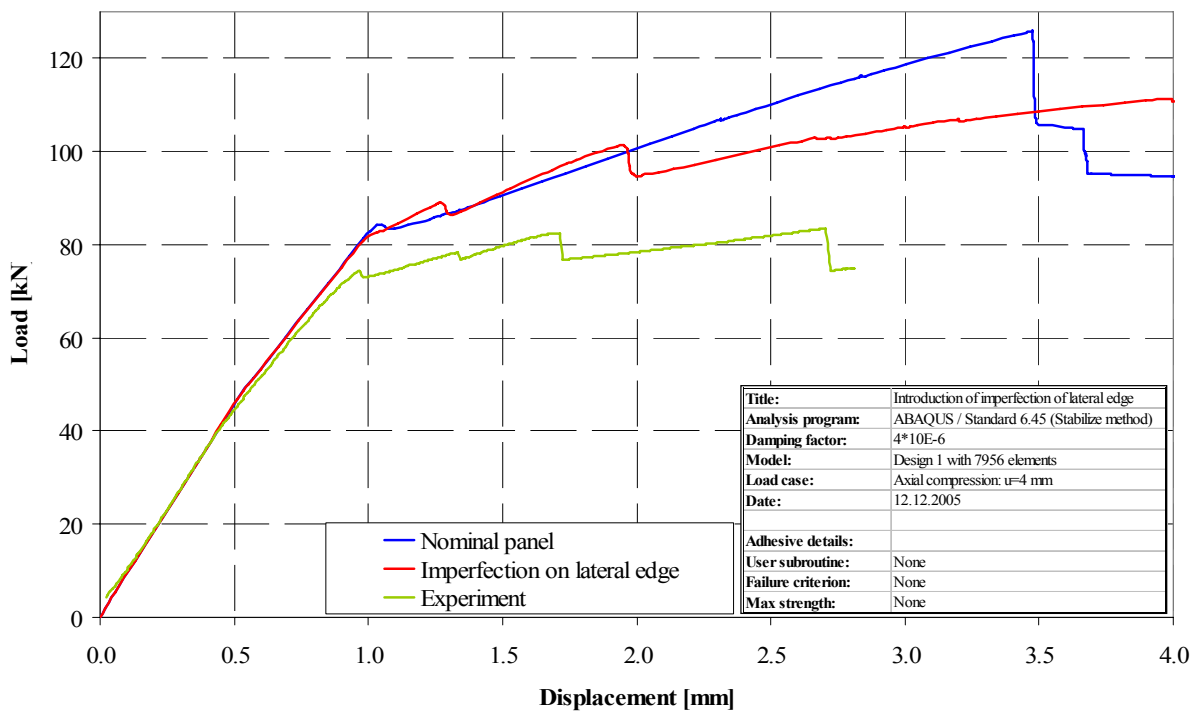


Figure 7-12 Load-shortening graph with imperfection introduced on lateral edge

Figure 7-13 shows the buckling shapes of the nominal panel (a), the modified panel (b) and the experimentally tested panel (c). Again the final buckling shapes were taken at a shortening

7.5 Evaluation of the strain gage data

As mentioned in Chapter 6, additionally to the Aramis measurement system, strain gages were positioned on the panel to measure the strain data during the experiment. In order to investigate possible reasons for the asymmetrical buckling behavior of the panel, the strains measured by the gages were compared to each other and to the numerical results. This was done because differences in the strains could be a hint that the panel was loaded asymmetrically.

The relevant strain gages for this investigation were the strain gages H0 to H3 and H22 to H25, which were all located on the skin side of the panel with the first four gages on the upper half, the last four gages on the lower half. The positions of all strain gages used in the experiment are shown in Figure 7-14.

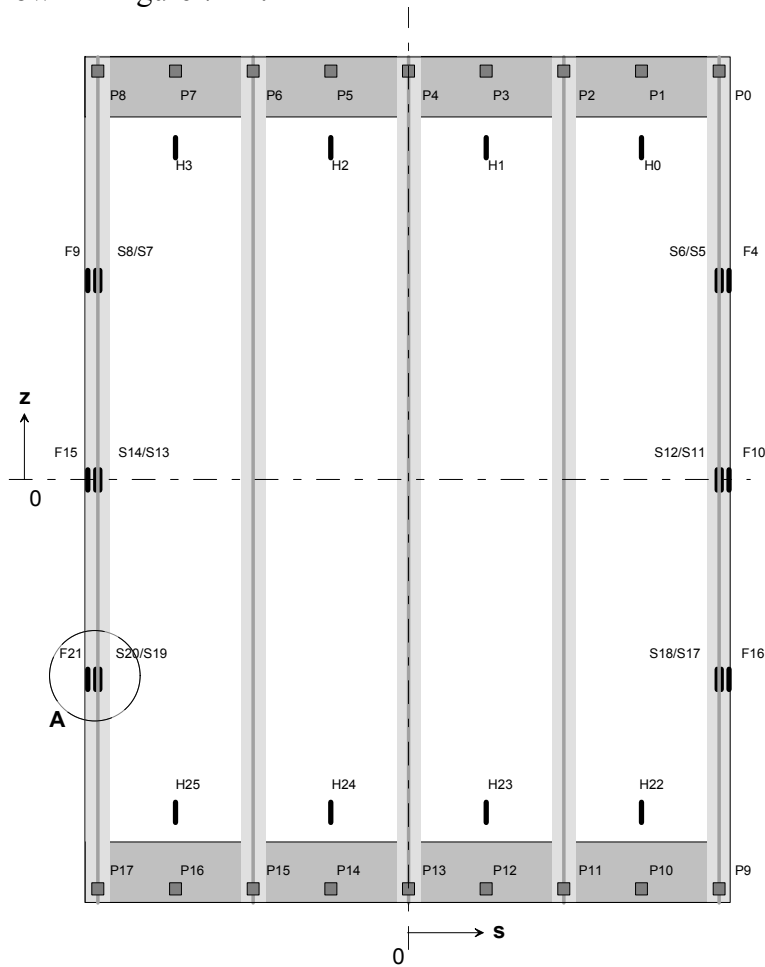


Figure 7-14 View of the strain gages from the skin side [14]

Table 7-1 gives the exact coordinates of the strain gages in reference to the z- and s-coordinate system.

The results of the comparison are given in Figure 7-15 for the strain gages on the upper half of the panel and in Figure 7-16 for the gages on the lower half of the panel. These figures show load-strain graphs. The strain gages predicted by ABAQUS are represented by the broken lines. It has to be mentioned that ABAQUS was not able to output the total strain data directly into the .odb-file for simulations including geometric nonlinearity. The output was only possible for logarithmic strain. Therefore the *ELPRINT function of ABAQUS was used to output the total strains “E” directly into the .dat-file. Since the strain gages had a two

dimensional expansion, the strain data of four elements of the simulation model that surrounded the coordinates of the strain gages was outputted and the average strain of these four values was calculated and taken as comparison value.

Name	Type	Arc length s [mm]	Height z [mm]	Distance to skin [mm]	Orientation [°]
H0	Skin	+198	+310	0	0
H1	Skin	+66	+310	0	0
H2	Skin	-66	+310	0	0
H3	Skin	-198	+310	0	0
H22	Skin	+198	-310	0	0
H23	Skin	+66	-310	0	0
H24	Skin	-66	-310	0	0
H25	Skin	-198	-310	0	0

Table 7-1 Position of the strain gages [14]

It could be seen that the strains predicted by ABAQUS were all very similar in the region up to local buckling. In general, the strains measured during the experiment were clearly higher than the ABAQUS strain but when comparing the strain data of the four gages to each other, the progression of the four curves was similar but the absolute strain values showed derivations. Especially the strains for the two outer strain gages H0 and H3 were almost identical up to a loading of 30 kN. The other strain gages H1 and H2 show the largest difference with a maximum at approximately 30 kN. The difference between the two was 17.9%.

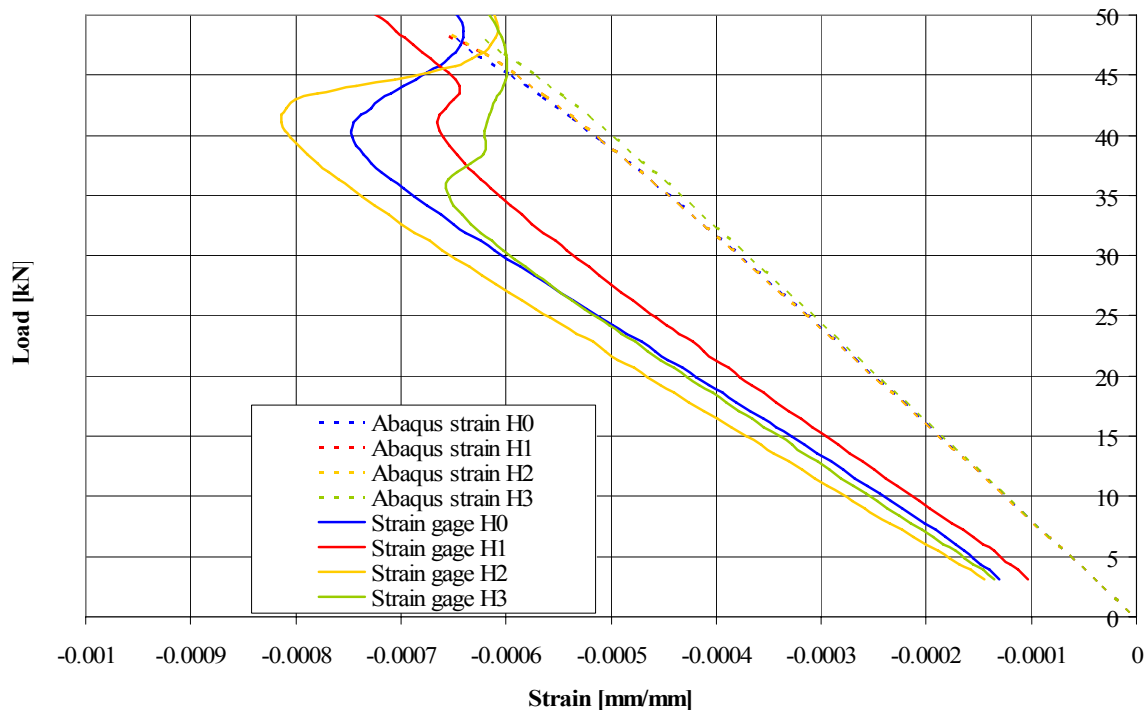


Figure 7-15 Strain gage and simulated strain data of H0 to H3

Although the strains measured by H2 were higher than the strains of the other gages, it was very unlikely that this difference was in any relation to the asymmetric buckling of the panel, especially because the progression of all curves was very similar and almost constant for all of

the strain gages for the area of small loading. None of the gages showed a stronger increase of strain as was expected if asymmetrical loading caused the asymmetric buckling behavior of the panel.

The next figure shows the load-strain graph for the gages on the lower side of the panel. Again the strains predicted by ABAQUS were similar at small loads although they differed more with increased loading. They were also again smaller than the strains measured by the gages H22 to H25.

The data of the strain gages themselves were very similar at small loading. Especially the results measured by H22 and H24 turned out to be similar even for higher loads. Even though the progression of the strain of H23 did not correspond very well with the other results, it was again judged unlikely that the differences in strain measured by the gages gave proof to the idea that asymmetrical loading lead to the asymmetrical buckling shape.

In conclusion, the evaluation of the results measured by the strain gages during the experiment did not give information about the possible reason for the asymmetrical buckling behavior of the panel. Although by the interpretation of the strain gage data it was judged not very likely that asymmetrical loading caused the asymmetrical buckling shape, further simulations investigating this approach were considered necessary, especially because no data were available at which strain asymmetric buckling occurred. In order to secure the results of the simulation, more experimental data from tested panels are required.

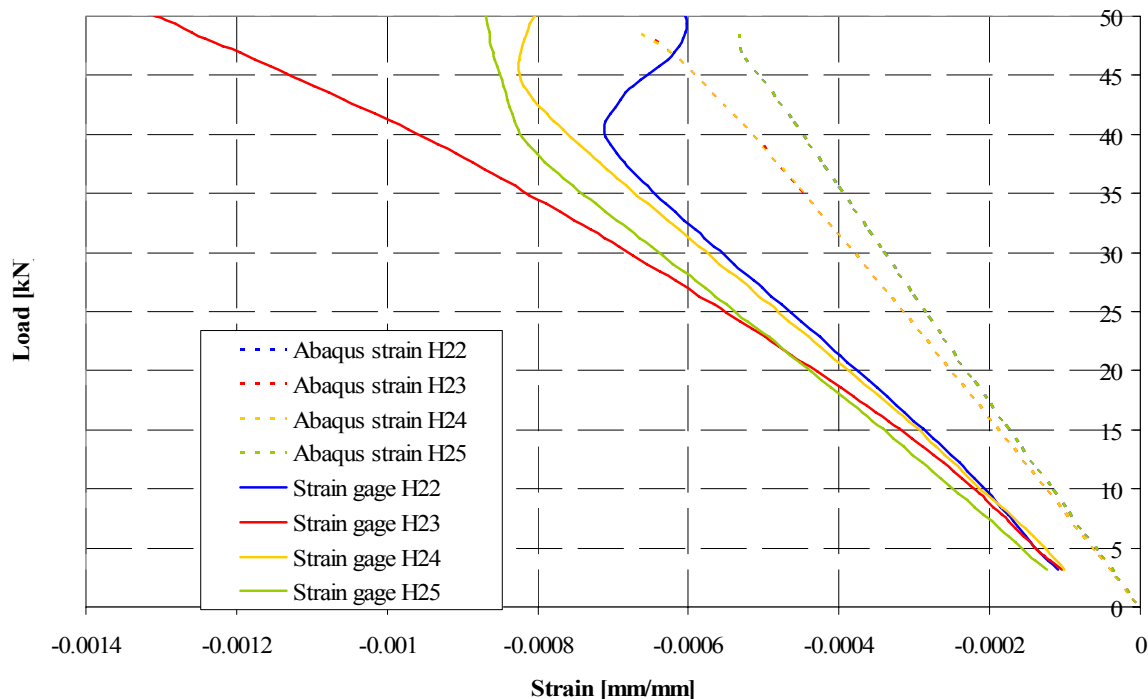


Figure 7-16 Strain gage and simulated strain data for H22 to H25

7.6 Comparison of different versions of the USDFLD

As mentioned earlier, the USDFLD was used as a means of modeling degradation in the skin-stringer interface. Figure 7-17 shows the load-shortening graph of different versions of the USDFLD in comparison with the experimental results. All models gave good prediction of the axial stiffness up to the point of local buckling. Afterwards, all simulation models showed a slightly stiffer buckling behavior than the experimentally tested model. The onset of global buckling was also predicted at a slightly smaller shortening.

The load-shortening curve of the original version of the USDFLD with a reduction of the Young's modulus to 0.1% when failure was experienced gave a very close prediction of the load-carrying capacity of the experimental results. The reduction value of the Young's modulus was chosen on the basis of a parametric study performed in [17] and the assumption that a value as close to zero as numerically possible was required in order to simulate the loss of load-carrying capacity by the adhesive. This good agreement is deceptive because this version of the USDFLD misrepresented the degree of damage in the adhesive layer and postbuckling mode shapes almost completely. As was described in Chapter 5 and shown in Figure 5-13, the USDFLD predicted a failure of almost all elements in the adhesive layer. This failure of the adhesive was not seen during the experimental testing. Debonding of the skin and the stringer flange was not experienced until the point of collapse and after collapse was only found in small locally restricted regions as shown in Figure 6-3b. Therefore the simulated model did not give a realistic prediction of failure.

This was also true for the USDFLD that took the principal stresses into account in the prediction of failure. The axial stiffness was only slightly higher than shown by the experimentally tested panel. Still, the subroutine predicted the failure of the entire adhesive layer. Therefore this version of the routine did not give a realistic prediction of failure.

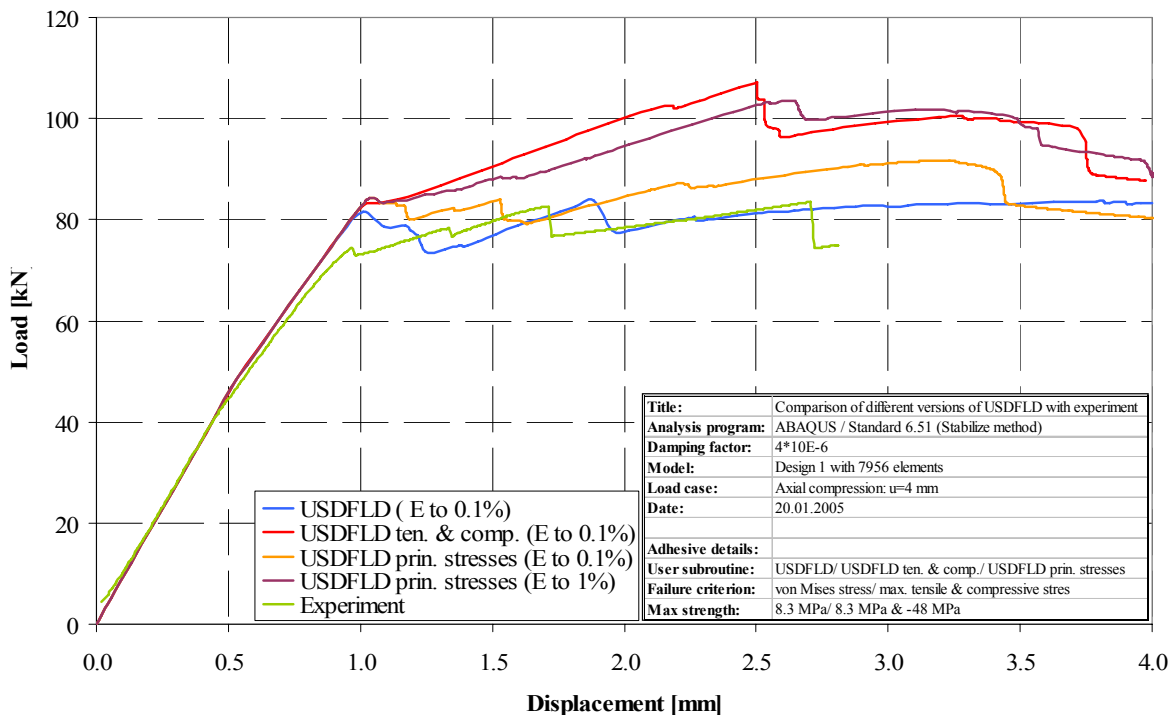


Figure 7-17 Load-shortening graph of different versions of the USDFLD in comparison to experimental results

There were also other factors that might have influence on the skin-stringer debonding for example the parameters that were used for the simulation of the adhesive and the composite were based on the material data provided by the producer of the adhesive, Hexcel. No experimental tests were performed to validate these data.

All other versions of the USDFLD predicted a much stiffer behavior of the panel, especially in the deep postbuckling region and therefore did not show good agreement with the experimental results.

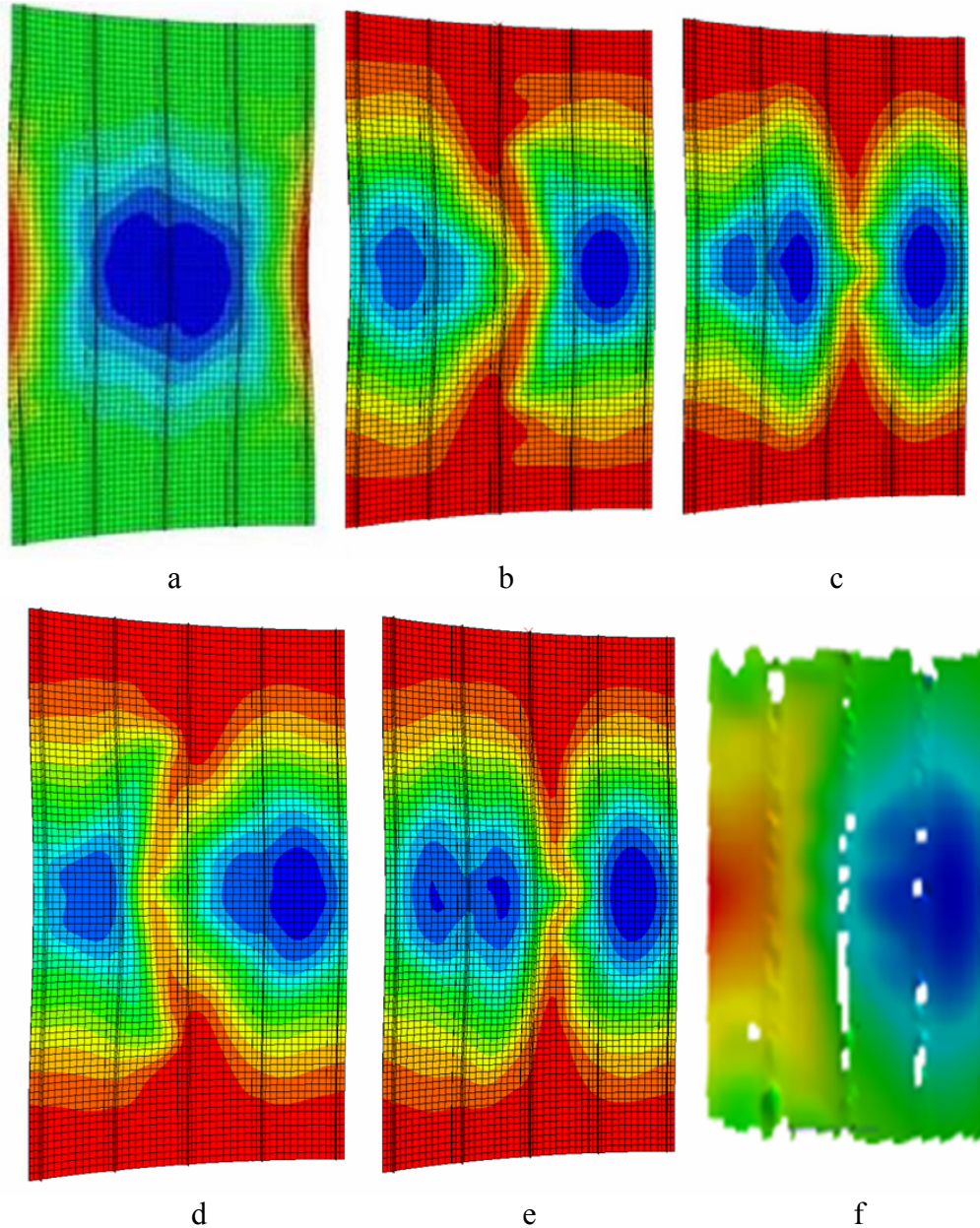


Figure 7-18 Final buckling shapes of different versions of USDFLD and experiment
 a. USDFLD (E to 0.1%)
 b. USDFLD Ten. & Comp. (E to 0.1%)
 c. USDFLD Ten. & Comp. (E to 1%)
 d. USDFLD Prin. Stresses (E to 1%)
 e. USDFLD Prin. Stresses (E to 1%)
 f. Experiment

The versions of the USDFLD Tension & Compression did however experience one change of the buckling mode and produced a proper collapse point in contrast to the original versions of the USDFLD. This was also observed for the principal stresses version of the USDFLD.

The fact that the USDFLD model gave closer predictions of the load-carrying capacity of the panel in comparison to the model without degradation signifies the importance of incorporating some form of degradation into the analysis for these types of panels. As has been noted in previous COCOMAT studies [13] numerical approaches that do not take degradation caused by composite damage into account, tend to overestimate the panel behavior, especially in the deep postbuckling region. Although the reduction in load-carrying capacity of the experimental tested panel was likely due to the asymmetric deformation causing mode shapes of lower structural stiffness, the USDFLD provided a mechanism to incorporate a reduction of load-carrying capacity into the analysis by the consideration of skin-stringer separation. Even though the USDFLD Principal Stresses was assumed to give a more realistic prediction of failure in terms of the number of failing elements than the original USDFLD and the USDFLD Tension & Compression, it failed to predict the asymmetric buckling shapes shown by the experiment. To determine the extent to which the different previously developed subroutines and subroutines developed in this work contributed to a more realistic prediction of the panel behavior and especially the separation of skin and stringer, further experimental results are required.

7.7 Summary of the numerical simulations and evaluation of additional aspects

In order to investigate the influence of different parameters on the buckling behavior of the panel, numerous numerical simulations were performed. These analyses aimed at evoking an asymmetrical buckling shape as was shown during the experimental testing of a panel similar to the COCOMAT panels.

The first imperfection that was added was a geometric imperfection of the skin. This was done to investigate the sensitivity of the panel to this kind of imperfection in general. Single and superimposed eigenmodes were introduced and scaled to a percentage of the skin thickness. From the results of the analyses it was concluded that the panel was stringer dominant, which meant that imperfections of the skin were not likely to have a great influence on the buckling behavior. Therefore skin imperfections were excluded as a reason for the asymmetrical buckling shape.

The next geometric imperfection that was added to the geometry of the panel was a variation of the stringer thickness. Layers of fiber were removed from and added to the different stringers in order to weaken and strengthen the structure of the panel to receive asymmetric buckling. Although it was possible to create a different buckling behavior of the panel, no asymmetric buckling mode shape was received. Also, the necessary changes in stringer lay up to evoke different buckling shapes were significant. Therefore imperfections of the stringer width were also very unlikely to be responsible for the asymmetric buckling behavior.

The third geometrical imperfection that was introduced to the geometry of the panel was produced by the introduction of concentrated forces on the lateral edges of the panel. The resulting displacements of these asymmetrical forces were superimposed with the geometry of the panel with different scale factors. When introducing imperfections with higher scale factors it was possible to change the buckling behavior of the panel. Although the buckling

shape was slightly asymmetric it did not show great similarity to the experimental results. It was concluded that although it was not possible to create the desired asymmetric buckling shape, the panel was sensitive to this kind of imperfection.

The last geometric imperfection that was used to create an asymmetrical buckling shape was an additional curving on one side of the panel. This was done to weaken the structure on one side and thereby evoke asymmetrical buckling. The curving was generated in the form of a sinusoidal function on the ten outer rows of nodes with decreasing magnitude going inward. Again it was possible to create a different buckling behavior of the panel but the new buckling shape was again not asymmetric. Therefore the structural weakness of one side of the panel as introduced in this work was not likely to be responsible for the asymmetric buckling shape, although the panel was sensitive to imperfection of the edges.

Asymmetrical loading was also considered as a possible reason for the asymmetric buckling behavior of the panel. In order to evaluate the influence of this kind of loading the data of the applied strain gages were analyzed. Concluding from the measurement data, there was no evidence that asymmetrical loading was introduced in such a way that caused asymmetrical buckling of the panel. Still, the data were not very entirely significant, the conclusions made should be verified.

Although the performed investigations show that the different imperfections alone were not enough to cause the asymmetry, it could not be excluded that a combination of these factors was a principal reason for the buckling behavior of the panel.

Finally, the modified versions of the user subroutine USDFLD were compared to the experimental data. The results of the subroutine did not agree well with the experimental results in terms of load-carrying capacity, buckling behavior and especially damage behavior as the extend of skin-stringer debonding was completely misrepresented. As for the model without any degradation, the buckling shapes predicted by all versions of the subroutine did not show asymmetric buckling. Still, the incorporation of a degradation model, namely the separation of skin and stringer caused by adhesive failure in the form of the user subroutine reduced the load-carrying capacity in the postbuckling region and therefore a more realistic buckling behavior was created. This was the reason why further improvement of the subroutines was recommended.

In conclusion, although it was possible to create different buckling shapes by adding different geometric imperfections, this work was not successful in the evoking asymmetrical buckling behavior shown by the experimentally tested panel. Still, conclusions were made about the sensitivity of the buckling behavior of the panel to different geometric imperfections and some factors were judged unlikely as possible reasons for asymmetric buckling.

In order to gain a better understanding of influences on the buckling behavior of the panel, further investigations are considered necessary. Useful parameters might include:

- Investigation of the influence of changes of the stringer width over the panel length
- Investigation of the influence of asymmetrical loading due to not parallel potting edges
- Investigation of the influence of longitudinal edge restraints
- Improved version of the user subroutines as described in Section 5.5
- Experimental testing of additional panels to be able to evaluate if asymmetric buckling occurs frequently or only occasionally for this type of panels

8. Summary and conclusions

This degree dissertation thesis focuses on two main topics. The first focus was the modification of user subroutines for the FE tool ABAQUS/Standard for the prediction of failure by the implementation of different failure criteria in the simulation, so degradation in the adhesive layer, which connects skin and stringer of stiffened composite panels, was integrated in the simulation. This was done by changing previously developed user subroutines that introduced degradation through a reduction of the material properties of the adhesive. Simple stress based failure criteria as the von Mises stress, normal and shear stresses and principal stresses were implemented to predict failure. However, this work did not aim at the implementation of the most realistic failure criterion, more at the evaluation of the different failure criteria.

The second main focus was put on the investigation of various influences on the buckling behavior of the panel used in the COCOMAT project. This was done particularly with regard to the asymmetric buckling behavior shown by a similar experimentally tested panel.

Firstly, a literature review was given on the main topics relevant for the work. The first section (Section 2.1) described the basic principals of fiber-reinforced composite materials and classical laminate theory. Additionally, a review of adhesive joints was given to provide background on the adhesive layer connecting the skin and the stringer of the panel. The review included the basic theory of Volkersen (Section 2.2). Still, another literature review was considered necessary in order to investigate and define the most realistic failure criterion for the simulation of an adhesive. Finally, the finite element method was explained on the basis of the minimum of potential energy and the displacement method was introduced. Also the concept of nonlinear FE analysis was explained as used by the commercial FE tool ABAQUS and a brief overview was given on the usage and application of both ABAQUS and FE tools in general (Section 2.3).

In Chapter 3, an overview was given on the previously developed user subroutines and explanations of the basic data flow of these routines. In Chapter 4 a brief description of the model that was used for all simulations in this work, including the geometry and the modeling was given. In order to investigate the sensitivity of the subroutines, parametric studies were performed in Section 5.1 and 5.2. The studied parameters included changes in the subroutine code and modifications of the simulation model, which included the number of elements and physical dimensions of elements. Generally, the results of the different simulations were very similar. Still, in some cases the more simple model was used for the following simulations although the more complex model predicted an earlier onset of global buckling or a reduced axial stiffness. The choice of model was therefore not conservative. This should be taken into consideration in future simulations.

Based on the previously developed user subroutines two new versions of the USDFLD were developed. The main goal of this part of the work was to implement typical failure criteria into the routines to receive a first impression of the influence of the integration of degradation into the simulations. It did not yet aim at the implementation of the failure criterion that seemed the most suitable for the simulation of the adhesive. Within the first new version of the USDFLD (Section 5.3) it was possible to assign different maximum allowable stresses for the three normal directions and the shear stress. Also, the routine was able to distinguish between failure due to tension or compression. Because the use of normal stresses depended on the chosen coordinate system, which did not have a physical context, another typical failure criterion was implemented into the USDFLD. The version using the normal stresses

was mainly included in this work because it represented a major step in the chronological development of the task. The next version of the USDFLD, as described in Section 5.4, was based on the principal stresses as the relevant stresses for the prediction of failure. Due to this change in the concept, the prediction of failure no longer depended on the choice of a coordinate system. The different versions of the subroutine were compared to each other and conclusions on failure prediction, time assumption and accuracy were made. The USDFLD Tension & Compression was only based on a theoretical background, therefore it was concluded that this version did not give a realistic prediction of failure. For the USDFLD Principal Stresses it was assumed that the prediction of failure was more realistic although it was not possible to decide which criterion, the principal stresses or the von Mises stress was more suitable for the adhesive. The time consumption of the USDFLD Principal Stresses was generally higher than for the original version but several ways to reduce the time consumption by a simplification of the programming code were found (Section 5.4). The code also included some weaknesses in the programming of the second field variable (Appendix A), which could be improved in future works.

Generally, it should be noted that the programming code of all included subroutines (Appendix A) was not looked at as optimal in all aspects. Therefore a final assurance of quality was considered necessary before further investigation and modification of the routines.

In the seventh chapter of the work the focus was the comparison of simulation data and the measurement data collected during the experimental testing of a panel similar to the panels used in the COCOMAT project. Firstly, the experiment and the applied measurement technique were described. Conclusions were made about the buckling behavior of the panel in comparison to the previously performed simulations. Based on these conclusions, several numerical simulations were executed. These analyses investigated the influence of different parameters on the buckling behavior of the panel. These parameters included imperfections of the skin, the stringers and the lateral edges. The simulations aimed at creating an asymmetric buckling shape as observed by the experimental tested panel. Although the panel showed sensitivity to several introduced imperfections, especially on the lateral edges, all of the modified models were unable to capture the asymmetrical buckling shape. Also, the data of the strain gages that was collected during the experiment was evaluated and indicated that the asymmetric buckling shape was not likely to have occurred due to an asymmetric application of the compression load. Still, the introduction of asymmetric loading could not be excluded entirely as possible reason for the asymmetric buckling behavior of the panel. Further experimental results were assumed necessary to secure this conclusion. At last, the experiment was compared to the new versions of the USDFLD. It was concluded that the new versions of the subroutine gave a more realistic prediction of failure than the model without any degradation involved. Still, a higher axial stiffness of the panel was predicted in comparison to the experiment. It should be noted that all subroutines predicted a higher extend of adhesive failure than shown by the tested panel. Based on the experimental and simulation data, it was not possible to make a decision whether the implementation of the principal stresses in comparison to the von Mises stress gave a more realistic prediction of adhesive failure.

Finally, a set of recommendations was formulated for the two major topics of this work and included the improvement of the user subroutines as means of a more realistic prediction of failure and the investigation of possible influences that lead to the asymmetric buckling shape shown in the experiment.

For the development of the user subroutines the following recommendations were considered most important:

- Literature review to decide which failure criterion is the most realistic criterion for adhesives in general
- Implementation of this criterion in the routine and performance of simulations with the new criterion
- Reduction of the code of the USDFLD Principal Stress to decrease the time consumption
- Extension of the subroutine code to improve the post processing possibilities concerning exceeded failure criteria and the number of failing elements

For the investigation of possible influences as reasons for asymmetric buckling:

- Investigation of the influence of asymmetric loading due to not parallel potting edges
- Investigation of the influence of longitudinal edge restraints
- Experimental testing of a number of similar panels in order to be able to evaluate the effect of asymmetric buckling occurs frequently or only occasionally

9. References

- [1] ABAQUS Analyses Users Manual
ABAQUS Inc.
2003
- [2] Altenbach H., Altenbach J., Rikards R.,
Einführung in die Mechanik der Laminat- und Sandwichtragwerke,
Deutscher Verlag für Grundstoffindustrie Stuttgart, 1996
- [3] ARAMIS User's Manual
GOM, Optical Measurement Technique
2005
- [4] Beitz W., Grote K.-H.,
Dubbel Taschenbuch für den Maschinenbauer
Springer 1997
- [5] Internet URL: www.cocomat.de
- [6] Gross D., Hauger W., Schnell W., Wriggers P.
Technische Mechanik Band 4
Springer, 2004
- [7] Harder J.,
Technische Mechanik 1 und 2,
Department of Aerospace Technology, Aachen University of Applied
Sciences, 2002/2003
- [8] Hexel Composites.–Product Data, www.hexcel.com, 2005
- [9] Hyer M.,
Stress analysis of fiber-reinforced composite materials
WCB/McGraw-Hill, 1998
- [10] Kling A., Degenhardt R.,
Design and Analysis of Undamaged Panels (Technical Report)
Institute of Composite Structures and Adaptive Systems, DLR,
Braunschweig, August 2005
- [11] Nonhoff G., Harder J., Dahmann P.,
Faserverbundwerkstoffe und –bauweisen
Department of Aerospace Technology, Aachen University of Applied
Sciences, 2005
- [12] Niu M. D. Y.,
Composite Airframe Structures, Conmilit Press LTD. Hong Kong, 1992
- [13] Orifici A. C., Thomson R. S., Degenhardt R., Kling A., Rohwer K.
Bayandor J.
Degradation investigation in a postbuckling composite stiffened fuselage
panel, Nov. 2005
- [14] P 23 (resume)
Institute of Composite Structures and Adaptive Systems, DLR
Braunschweig, Nov. 15th 2005
- [15] Puck A.,
Festigkeitsanalyse von Faser–Matrix–Laminaten
Hanser, 1995
- [16] Rao S. S.,
The finite element method in engineering
Butterworth-Heinemann, 1999
- [17] Reinsch A., Degenhardt R.,
Numerical Finite-Element-Analysis of degradation in stiffened CFRP

- panels, IB131-2005/34
Institute of Composite Structures and Adaptive Systems, DLR,
Braunschweig, August 2005
- [18] Rolfes R., Hühne C., Kling A., Temmen H., Geier B., Klein H., Teßmer J.,
Zimmermann R.
Advances in computational stability analysis of thin-walled aerospace
structures regarding postbuckling, robust design and dynamic loading
Institute of Structural Mechanics, DLR, Braunschweig, Germany
- [19] Roloff, Mattek
Maschinenelemente
Vieweg, Juni 2005
- [20] Römelt P., Kling A., Degenhardt R.,
Entwicklung axial gedrückter, versteifter CFK-Paneele unter
Schädigungsaspekten, IB 131-2005/26
Institute of Composite Structures and Adaptive Systems, DLR
Braunschweig, August 2005
- [21] Schnell W., Gross D., Hauger W.
Technische Mechanik Band 2 Elastostatik
Springer, 1998
- [22] Schürman H.,
Konstruieren mit Faser -Kunststoff -Verbunden
VDI/ Springer 2005
- [23] Schuster K., Degenhardt R., Kling A.,
Nichtlineare Tragwerksanalyse axial gedrückter versteifter CFK-Paneele,
IB 131-2005/32
Institute of Composite Structures and Adaptive Systems, DLR,
Braunschweig, August 2005
- [24] Tsai Y. M., Oplinger D. W., Morton J.
Improved theoretical solutions for adhesive lap joints, Elsevier: Solid
Structures Vol. 35, No. 12, pp 1163-1185, 1998
- [25] Wahle M.,
Leichtbaustrukturen und Strukturdynamik,
Department of Aerospace Technology, Aachen University of Applied
Sciences, 2005
- [26] Wehnes H.,
Fortran 77- Strukturiertes Programmieren mit Fortran 77
Hanser, 1992

Appendix A: Subroutine codes

USDFLD original

Code:

<pre> subroutine usdfd(field,statev,pnewdt,direct,t,celent,time,dtime, 1 cmname,orname,nfield,nstatv,noel,npt,layer,kspt,kstep,kinc, 2 ndi,nshr,coord,jmac,jmatyp,matlayo,laccfla) C include 'aba_param.inc' character*80 cmname,orname character*8 flgray(15) dimension field(nfield),statev(nstatv),direct(3,3),t(3,3),time(2), * coord(*),jmac(*),jmatyp(*) dimension array(15),jarray(15) DATA index/0/ SAVE index </pre>	A1
<pre> C STRENGTH PARAMETERS PARAMETER(SMaxS11=8.D0,SMaxS13=38.D0,SMaxDruck=48.D0) </pre>	A2
<pre> C Path of the result file, has to be checked before analysis start OPEN(100,FILE='C:\Task141\P1.3.6\abaqus\work2\output.txt') </pre>	A3
<pre> C Get stress from previous increment. call getvrm('S',array,jarray,flgray,jrcd, \$ jmac, jmatyp, matlayo, laccfla) S11 = array(1) S13 = ABS (array(5)) </pre>	A4
<pre> C Get Mises stress from previous increment. call getvrm('SINV',array,jarray,flgray,jrcd, \$ jmac, jmatyp, matlayo, laccfla) SMises = ABS (array(1)) </pre>	A5
<pre> C Maximum value of stress up to this point in time: CALL GETVRM('SDV',ARRAY,JARRAY,FLGRAY,JRCD,JMAC,JMATYP, \$ MATLAYO,LACCFLA) S11MAX = ARRAY(1) S13MAX = ARRAY(2) SMisesMax = ARRAY(3) </pre>	A6
<pre> C Use the maximum stress as a Damage variable </pre>	A7

Appendix A: Subroutine codes

<pre> Damage1 = MAX(S11 , S11MAX) Damage2 = MAX(S13 , S13MAX) Damage3 = Max(SMises, SMisesMax) ratio=(Damage3/SMaxDruck) </pre>	
<pre> C write information out to the output file output.txt IF (index.EQ.0) THEN WRITE(100,(18A14)) 'NOEL','KINC','NPT','DTIME', 1 'ratio','SMises', 'SMisesMax','Damage3' index=1 ENDIF IF (ratio.GT.1.D0.AND.FIELD(3).EQ.0.D0) THEN WRITE(100,(14G14.3)) NOEL,KINC,NPT,DTIME, 1 ratio,SMises, SMisesMax,Damage3 ENDIF </pre>	A8
<pre> C UPDATE FIELD VARIABLES FIELD(1) = 0.D0 FIELD(2) = 0.D0 FIELD(3) = 0.D0 IF (Damage1 .GE. SMaxS11) FIELD(1) = 1.D0 IF (Damage2 .GE. SMaxS13) FIELD(2) = 1.D0 IF ((Damage3/SMaxDruck) .GE. 1.D0) FIELD(3) = 1.D0 </pre>	A9
<pre> C Store the maximum stress as a solution dependent state variable STATEV(1) = Damage1 STATEV(2) = Damage2 STATEV(3) = Damage3 </pre>	A10
<pre> C If error, write comment to .DAT file: IF(JRCD.NE.0)THEN WRITE(6,*) 'REQUEST ERROR IN USDFLD FOR ELEMENT NUMBER ', 1 NOEL,'INTEGRATION POINT NUMBER ',NPT ENDIF C RETURN END </pre>	A11

Documentation:

A1:

Interface between the user subroutine and ABAQUS. In the interface the subroutine calls on the different arrays for example for the field variables and solution- dependent state variables (FIELD, STATEV). It also gets information about the process of the iteration for example the time increment DTIME. The declaration of variables is also part of this part.

A2:

Definition of the parameters of the adhesive, namely the maximal allowable stresses. These are the only material parameters that are defined in the subroutine. All other material data is defined in the input file.

A3:

Appendix A: Subroutine codes

The path of the result file has to be checked before the analysis starts

A4:

Get the stresses from the last increment. In the stress array, the single component of the stresses are stored. The components are ordered as follows:

S₁₁= array(1) S₂₂= array(2) S₃₃= array(3)
 S₁₂= array(4) S₁₃= array(5) S₂₃= array(6)

The different components of the field are assigned to the different variables of the stresses for example “S11” for the normal stress in the one direction.

A5:

Get the Von Mises stresses “SINV” from the previous increment and assign it to the variable SMises.

A6:

Call the solution- dependent state variables in which the maximum stresses up to this increment were stored. This variable is named “S11MAX” for the 1 direction.

A7:

Comparison of the current stress in the increment and the max. stresses up to this increment. The maximum value is stored in the variable” Damage1”. This prevents a healing mechanism because the Young’s modulus stays reduced for the upcoming increments.

A8:

Output requests. If the index is zero or the defined stress ratio Damage3/SMAXDruck exceeds one and Field(3)=0 the subroutine writes several data to the text file “output.txt”.

A9:

The field variables are set to zero which is the normal position. Afterwards the new maximum stresses up to this increment (“Damage”) is compared to the maximum allowable stresses (“SMAXS”). If the Damage stresses is greater than the SMAX value, failure occurs and the field variable (“FIELD”) is set to one. If there is no failure, the FV remain zero.

A10:

The maximum stresses are stored as solution dependent state variable in the SDV array.

A11:

If an error occurs, a warning will be written into the data file, including the element number and the integration point number where the error occurred.

USDFLD Tension & Compression

Code:

<pre> subroutine usdfld(field,statev,pnewdt,direct,t,celent,time,dtime, 1 cmname,orname,nfield,nstatv,noel,npt,layer,kspt,kstep,kinc, 2 ndi,nshr,coord,jmac,jmatyp,matlayo,laccfla) c include 'aba_param.inc' c character*80 cmname,orname character*8 flgray(15) dimension field(nfield),statev(nstatv),direct(3,3),t(3,3),time(2), * coord(*),jmac(*),jmatyp(*) dimension array(15),jarray(15) DATA index/0/ SAVE index </pre>	A1
<pre> factor=ABS(SMaxS11/SMaxDruck) </pre>	A2

Appendix A: Subroutine codes

<p>C STRENGTH PARAMETERS PARAMETER(SMaxS11=8.3D0,SMaxS22=8.3D0,SMaxS33=8.3D0, 1SMaxShear=38.D0,SMaxDruck=-48.D0)</p>	A3
<p>OPEN(100,FILE='E:\A.Winzen\Work\Test.txt')</p>	A4
<p>C Get stress from previous increment. call getvrm('S',array,jarray,flgray,jrcd, \$ jmac, jmatyp, matlayo, laccfla) S11 = array(1) S22 = array(2) S33 = array(3) S12 = ABS (array(4)) S13 = ABS (array(5)) S23 = ABS (array(6)) SShear = MAX (S12, S13, S23)</p>	A5
<p>C Maximum value of stress up to this point in time: CALL GETVRM('SDV',ARRAY,JARRAY,FLGRAY,JRCD,JMAC,JMATYP, \$ MATLAYO,LACCFLA) S11MAX = ARRAY(1) S22MAX = ARRAY(2) S33MAX = ARRAY(3) SShearMAX = ARRAY(4)</p>	A6
<p>C Use the maximum stress as a Damage variable IF(S11.GT.0.D0.AND.S11MAX.GE.0.D0)THEN Damage1 = MAX(S11 , S11MAX) ENDIF</p>	A7
<p>IF(S11.GT.0.D0.AND.S11MAX.LE.0.D0)THEN IF(S11.GT.(ABS(S11MAX)*factor)) Damage1=S11 ENDIF</p>	A8
<p>IF(S11.GT.0.D0.AND.S11MAX.LE.0.D0)THEN IF(S11.LT.(ABS(S11MAX)*factor)) Damage1=S11MAX ENDIF</p>	A9
<p>IF(S11.LT.0.D0.AND.S11MAX.GE.0.D0)THEN IF(S11MAX.GT.(ABS(S11)*factor)) Damage1=S11MAX ENDIF</p>	A10
<p>IF(S11.LT.0.D0.AND.S11MAX.GE.0.D0)THEN IF(S11MAX.LT.(ABS(S11)*factor)) Damage1=S11 ENDIF</p>	A11
<p>IF(S11.LT.0.D0.AND.S11MAX.LE.0.D0)THEN Damage1 = MIN(S11, S11MAX) ENDIF</p>	A12

Appendix A: Subroutine codes

<pre> IF(S22.GT.0.D0.AND.S22MAX.GE.0.D0)THEN Damage2 = MAX(S22 , S22MAX) ENDIF C IF(S22.GT.0.D0.AND.S22MAX.LE.0.D0)THEN IF(S22.GT.(ABS(S22MAX)*factor)) Damage2=S22 ENDIF C IF(S22.GT.0.D0.AND.S22MAX.LE.0.D0)THEN IF(S22.LT.(ABS(S22MAX)*factor)) Damage2=S22MAX ENDIF C IF(S22.LT.0.D0.AND.S22MAX.GE.0.D0)THEN IF(S22MAX.GT.(ABS(S22)*factor)) Damage2=S22MAX ENDIF C IF(S22.LT.0.D0.AND.S22MAX.GE.0.D0)THEN IF(S22MAX.LT.(ABS(S22)*factor)) Damage2=S22 ENDIF C C IF(S22.LT.0.D0.AND.S22MAX.LE.0.D0)THEN Damage2 = MIN(S22, S22MAX) ENDIF </pre>	A13
<pre> IF(S33.GT.0.D0.AND.S33MAX.GE.0.D0)THEN Damage3 = MAX(S33 , S33MAX) ENDIF C IF(S33.GT.0.D0.AND.S33MAX.LE.0.D0)THEN IF(S33.GT.(ABS(S33MAX)*factor)) Damage3=S33 ENDIF C IF(S33.GT.0.D0.AND.S33MAX.LE.0.D0)THEN IF(S33.LT.(ABS(S33MAX)*factor)) Damage3=S33MAX ENDIF C C IF(S33.LT.0.D0.AND.S33MAX.GE.0.D0)THEN IF(S33MAX.GT.(ABS(S33)*factor)) Damage3=S33MAX ENDIF C IF(S33.LT.0.D0.AND.S33MAX.GE.0.D0)THEN IF(S33MAX.LT.(ABS(S33)*factor)) Damage3=S33 ENDIF C IF(S33.LT.0.D0.AND.S33MAX.LE.0.D0)THEN Damage3 = MIN(S33, S33MAX) ENDIF C </pre>	A14
<pre> Damage4=MAX(SShear,SShearMAX) </pre>	A15
<pre> C UPDATE FIELD VARIABLES FIELD(1) = 0.D0 FIELD(2) = 0.D0 FIELD(3) = 0.D0 </pre>	A16

Appendix A: Subroutine codes

FIELD(4) = 0.D0	
<pre> IF (Damage1.GT.0.D0) THEN IF (Damage1.GE.SMaxS11) FIELD(1) = 1.D0 ratio1 = (Damage1/SMaxS11) ELSE IF (Damage1.LE.SMaxDruck) FIELD(1) = 1.D0 ratio1 = (Damage1/SMaxDruck) ENDIF </pre>	A17
<pre> IF (Damage2.GT.0.D0) THEN IF (Damage2.GE.SMaxS22) FIELD(2) = 1.D0 ratio2 = (Damage2/SMaxS22) ELSE IF (Damage2.LE.SMaxDruck) FIELD(2) = 1.D0 ratio2 = (Damage2/SMaxDruck) ENDIF </pre>	A18
<pre> IF (Damage3.GT.0.D0) THEN IF (Damage3.GE.SMaxS33) FIELD(3) = 1.D0 ratio3 = (Damage3/SMaxS33) ELSE IF (Damage3.LE.SMaxDruck) FIELD(3) = 1.D0 ratio3 = (Damage3/SMaxDruck) ENDIF </pre>	A19
<pre> IF (Damage4.GE.SMaxShear) FIELD(4) = 1.D0 </pre>	A20
<pre> C Store the maximum stress as a solution dependent state variable STATEV(1) = Damage1 STATEV(2) = Damage2 STATEV(3) = Damage3 STATEV(4) = Damage4 </pre>	A21
<pre> C write information out to the output file output.txt IF (index.EQ.0) THEN WRITE(100,'(25A12)') 'NOEL','KINC','NPT','DTIME', 1 'factor','S11','S22','S33','SShear','S11MAX','S22MAX', 2 'S33MAX','SShearMAX','Damage1','Damage2','Damage3', 3 'Damage4','Field1','Field2','Field3','Field4' index=1 ENDIF C IF ((index.EQ.1.AND.NOEL.EQ.290)) THEN WRITE(100,'(25G12.3)') NOEL,KINC,NPT,DTIME,factor,S11,S22, 1 S33,SShear,S11MAX, S22MAX, S33MAX, SShearMAX,Damage1,Damage2, 2 Damage3,Damage4,FIELD(1),FIELD(2),FIELD(3),FIELD(4) ENDIF </pre>	A22
<pre> C If error, write comment to .DAT file: IF(JRCD.NE.0)THEN WRITE(6,*) 'REQUEST ERROR IN USDFLD FOR ELEMENT NUMBER ', 1 NOEL,'INTEGRATION POINT NUMBER ',NPT </pre>	A23

Appendix A: Subroutine codes

ENDIF C C RETURN END	
----------------------------------	--

Documentation:

A1:

Interface between the user subroutine and Abaqus. In the interface the subroutine calls on the different arrays for example for the field variables and solution dependent state variables (FIELD, STATEV). The subroutine also gets information about the process of the integration for example the time increment DTIME. The declaration of variables is also part of this part.

A2:

The variable “factor” is defined as the ratio of the maximum allowable tension stress SmaxS11 to the maximum allowable compressive stress SmaxDruck. In this case, the factor is the same for all directions because the maximum allowable stresses are the same in all directions.

A3:

Definition of the parameters of the adhesive, namely the maximal allowable stresses. These parameters are the only material parameters that are defined in the subroutine. All other material data is defined in the input file.

A4:

The path of the result file has to be checked before the analysis.

A5:

Get stresses from the previous increment. In the stress array, the single components of the stresses are stored. The components are ordered as follows:

Normal stress components:

$S_{11}=\text{array}(1)$ $S_{22}=\text{array}(2)$ $S_{33}=\text{array}(3)$

Shear stress components:

$S_{12}=\text{array}(4)$ $S_{13}=\text{array}(4)$ $S_{23}=\text{array}(5)$

It is possible to take the maximum value of the three stresses because they are all compared to the same maximum shear stress defined in A3 and because only the absolute values are of interest.

A6:

Call maximum stresses (SMAX) up to this increment that are stored in the SDVarray.

A7-A15:

Use the maximum values of the stresses as Damage variable. Six different options have to be checked to detect the correct value that has to be stored in the damage variable. The focus is put on the fact that the relevant stress, the stress that will lead to failure, is chosen as the critical value.

A7:

If the current stress and the stress up to this increment are both positive, it is possible to take the maximum of these stresses as the damage variable.

A8:

If the current stress is positive and the maximum stress up to this increment is negative, it is necessary to compare the absolute values of the stresses because it is possible when only taking the maximum or minimum of these stresses into consideration, that an element, which has failed earlier might be “repaired” due to the choice of stress as the damage value. Since the maximum compressive stress is higher than the maximum tensile stress, it is necessary to use the factor calculated in A2 in order to define the right value as damage value. As described earlier the factor is the ratio of the maximum tensile stress to the maximum compressive stress is taken. Therefore the positive stress value S is the relevant stress value as long as the negative stress is greater than -48MPa.

A9:

This can be seen as the “ELSE”-case to A8. If the negative stress SMax becomes less than -48MPa, this means that the absolute value becomes greater than 48MPa, and it is stored as damage value.

Appendix A: Subroutine codes

A10:

Here the damage value is defined if the current stress S is negative and the maximum stress up to the increment S_{Max} is positive. This specification is made for the same reason as described under A8, to prevent the “healing” of elements. Again, the stress ratio is used to define the damage value. The absolute values of the stresses are compared. If the maximum stress is higher than the product of the stress ratio and the current stress, the maximum stress is stored as the damage value.

A11:

Again, this is the “ELSE”-case of A10. If the maximum stress S_{Max} is less than the current stress S multiplied with the factor, the negative stress is taken into consideration.

A12:

If both the maximum stress up to the increment and the current stress are negative, the smaller value is stored in the damage variable.

A13:

Definition of the damage value for the stresses in 2-direction (analogous A7-A12)

A14:

Definition of the damage value for the stresses in 3-direction (analogous A7-A12)

A15:

Comparison of the maximum shear stress up to this increment to the current shear stress and storage of this value as damage variable.

A16:

All field variables (FV) are set to zero. This indicates that no failure has occurred yet. This is the initial situation.

A17-A19:

Comparison of Damage stress to maximum allowable stress

A17:

The function checks if the Damage1 stress up to this point is positive. When this is the case, the normal stresses are compared to the maximum allowable tensile stress of the adhesive and the FV is set to one if this failure criterion is exceeded. If the Damage1 stress is negative, it is compared to the maximum allowable compression stress and the corresponding FV is also changed to one. Furthermore ratio 1 is calculated in both cases.

A18:

Comparison of Damage2 stress to maximum allowable stress in 2-direction (analogous A17)

A19:

Comparison of Damage3 stress to maximum allowable stress in 3-direction (analogous A17)

A20:

Comparison of Damage4 stress to maximum allowable shear stress; FV is set to one if failure criterion is exceeded.

A21:

The maximum stress (Damage) is stored in the solution dependent state variables. The SDVs are updated only once per increment.

A22:

Output request. Several data for example all stresses, the element number (NOEL) and the number of integration point (NPT) are written out to a txt-file for the example of element 290.

A23:

If an error occurs, a warning will be written out into the data file, including the element number and the integration point number where the error occurred.

USDFLD Principal Stresses**Code:**

<pre> subroutine usdfld(field,statev,pnewdt,direct,t,celent,time,dtime, 1 cmname,orname,nfield,nstatv,noel,npt,layer,kspt,kstep,kinc, 2 ndi,nshr,coord,jmac,jmatyp,matlayo,laccfla) c include 'aba_param.inc' c character*80 cmname,orname character*8 flgray(15) dimension field(nfield),statev(nstatv),direct(3,3),t(3,3),time(2), * coord(*),jmac(*),jmatyp(*) dimension array(15),jarray(15) DATA index/0/ SAVE index REAL factor </pre>	A1
<pre> C STRENGTH PARAMETERS PARAMETER(SMaxSP1=8.3D0,SMaxSP2=8.3D0,SMaxSP3=8.3D0, 1SMaxShear=38.D0,SMaxDruck=-48.D0) </pre>	A2
<pre> factor=ABS(SMaxSP1/SMaxDruck) </pre>	A3
<pre> OPEN(100,FILE='E:\A.Winzen\Work\principal_stresses.txt') </pre>	A4
<pre> C Get principal stress from previous increment. call getvrm('SP',array,jarray,flgray,jrcd, \$ jmac, jmatyp, matlayo, laccfla) SP1 = array(1) SP3 = array(3) </pre>	A5
<pre> C Get stress from previous increment. call getvrm('S',array,jarray,flgray,jrcd, \$ jmac, jmatyp, matlayo, laccfla) S12 = ABS (array(4)) S13 = ABS (array(5)) S23 = ABS (array(6)) SShear = MAX (S12, S13, S23) </pre>	A6
<pre> C Maximum value of stress up to this point in time: CALL GETVRM('SDV',ARRAY,JARRAY,FLGRAY,JRCD,JMAC,JMATYP, \$ MATLAYO,LACCFLA) SP1MAX = ARRAY(1) SP3MAX = ARRAY(3) SShearMAX= ARRAY(4) </pre>	A7
<pre> C Use the maximum stress as a Damage variable IF(SP1.GT.0.D0.AND.SP1MAX.GE.0.D0)THEN Damage1 = MAX(SP1 , SP1MAX) ENDIF </pre>	A8

Appendix A: Subroutine codes

<pre>IF(SP1.GT.0.D0.AND.SP1MAX.LE.0.D0)THEN IF(SP1.GT.(ABS(SP1MAX)*factor)) Damage1=SP1 ENDIF</pre>	A9
<pre>IF(SP1.GT.0.D0.AND.SP1MAX.LE.0.D0)THEN IF(SP1.LT.(ABS(SP1MAX)*factor)) Damage1=SP1MAX ENDIF</pre>	A10
<pre>IF(SP1.LT.0.D0.AND.SP1MAX.GE.0.D0)THEN IF(SP1MAX.GT.(ABS(SP1)*factor)) Damage1=SP1MAX ENDIF</pre>	A11
<pre>IF(SP1.LT.0.D0.AND.SP1MAX.GE.0.D0)THEN IF(SP1MAX.LT.(ABS(SP1)*factor)) Damage1=SP1 ENDIF</pre>	A12
<pre>IF(SP1.LT.0.D0.AND.SP1MAX.LE.0.D0)THEN Damage1 = MIN(SP1, SP1MAX) ENDIF</pre>	A13
<pre>IF(SP3.GT.0.D0.AND.SP3MAX.GE.0.D0)THEN Damage3 = MAX(SP3 , SP3MAX) ENDIF C IF(SP3.GT.0.D0.AND.SP3MAX.LE.0.D0)THEN IF(SP3.GT.(ABS(SP3MAX)*factor)) Damage3=SP3 ENDIF C IF(SP3.GT.0.D0.AND.SP3MAX.LE.0.D0)THEN IF(SP3.LT.(ABS(SP3MAX)*factor)) Damage3=SP3MAX ENDIF C C IF(SP3.LT.0.D0.AND.SP3MAX.GE.0.D0)THEN IF(SP3MAX.GT.(ABS(SP3)*factor)) Damage3=SP3MAX ENDIF C IF(SP3.LT.0.D0.AND.SP3MAX.GE.0.D0)THEN IF(SP3MAX.LT.(ABS(SP3)*factor)) Damage3=SP3 ENDIF C IF(SP3.LT.0.D0.AND.SP3MAX.LE.0.D0)THEN Damage3 = MIN(SP3, SP3MAX) ENDIF</pre>	A14
<pre>Damage4=MAX(SShear,SShearMAX)</pre>	A15
<pre>C UPDATE FIELD VARIABLES FIELD(1) = 0.D0 FIELD(3) = 0.D0 FIELD(4) = 0.D0</pre>	A16

Appendix A: Subroutine codes

<pre> IF (Damage1.GT.0.D0) THEN IF (Damage1.GE.SMaxSP1) FIELD(1) = 1.D0 ratio1 = (Damage1/SMaxSP1) ELSE IF (Damage1.LE.SMaxDruck) FIELD(1) = 1.D0 ratio1 = (Damage1/SMaxDruck) ENDIF </pre>	A17
<pre> IF (Damage3.GT.0.D0) THEN IF (Damage3.GE.SMaxSP3) FIELD(3) = 1.D0 ratio3 = (Damage3/SMaxSP3) ELSE IF (Damage3.LE.SMaxDruck) FIELD(3) = 1.D0 ratio3 = (Damage3/SMaxDruck) ENDIF </pre>	A18
<pre> IF (Damage4.GE.SMaxShear) FIELD(4) = 1.D0 </pre>	A19
<pre> C Store the maximum stress as a solution dependent state variable STATEV(1) = Damage1 STATEV(3) = Damage3 STATEV(4) = Damage4 </pre>	A20
<pre> C write information out to the output file output.txt IF (index.EQ.0) THEN WRITE(100,'(25A12)') 'NOEL','KINC','NPT','DTIME', 1 'factor','SP1', 'SP3','SShear', 'SP1MAX', 2 'SP3MAX', 'SShearMAX', 'Damage1','Damage3','Damage4','Field1', 3 'Field3','Field4' index=1 ENDIF C IF ((index.EQ.1.AND.NOEL.EQ.7872.AND.KINC.GT.100)) THEN WRITE(100,'(25G12.3)') NOEL,KINC,NPT,DTIME,factor,SP1, 1 SP3,SShear,SP1MAX, SP3MAX,SShearMAX,Damage1, 2 Damage3,Damage4,FIELD(1),FIELD(3),FIELD(4) ENDIF </pre>	A21
<pre> C If error, write comment to .DAT file: IF(JRCD.NE.0)THEN WRITE(6,*) 'REQUEST ERROR IN USDFLD FOR ELEMENT NUMBER ', 1 NOEL,'INTEGRATION POINT NUMBER ',NPT ENDIF C C RETURN END </pre>	A22

Appendix A: Subroutine codes

Documentation:

A1:

Interface between the user subroutine and Abaqus. In the interface the subroutine calls on the different arrays for example for the field variables and solution dependent state variables (FIELD, STATEV). The subroutine gets information about the process of the integration for example the time increment DTIME. The declaration of variables is also part of this part.

A2:

Definition of the parameters of the adhesive, namely the maximal allowable stresses. These parameters are the only material parameters that are defined in the subroutine. All other material data is defined in the input file.

A3:

The variable “factor” is defined as the ratio of the maximum allowable tension stress SmaxS11 to the maximum allowable compressive stress SmaxDruck. In this case, the factor is the same for all directions because the maximum allowable stresses are the same in all directions.

A4:

The path of the result file has to be checked before the analysis.

A5:

Get principal stresses from the previous increment. In the stress array, the single components of the stresses are stored. The components are ordered as follows:

SP₁=array(1) SP₂=array(2) SP₃=array(3)

In Abaqus, SP₃ is the maximum principal stress, SP₂ the middle principal stress and SP₁ is the minimum principal stress. The middle principal stress is not used in the subroutine.

A6:

Get stresses from the previous increment. In the stress array, the single components of the stresses are stored. The components are ordered as follows:

Shear stress components:

S₁₂=array(4) S₁₃=array(4) S₂₃=array(5)

It is possible to take the maximum value of the three stresses because they are all compared to the same maximum shear stress defined in A2 and because only the absolute values are of interest.

The maximum shear stress chosen by the routine still depends on the coordinate system. Therefore in future versions of the routine it is considered useful to use the principal shear stress which is calculated by:

$$\tau_{\max} = \frac{\sigma_3 - \sigma_1}{2} \text{ respectively } \tau_{\max} = \frac{SP3 - SP1}{2}$$

A7:

Call maximum stresses (SMAX) up to this increment that are stored in the SDVarray. In this array the two maximum principal stresses and the maximum shear stress is stored.

A8-A14:

Use the maximum values of the stresses as Damage variable. Six different options have to be checked for the principal stresses to detect the correct value that has to be stored in the damage variable. The focus is put on the fact that the relevant stress, the stress that will lead to failure, is chosen as the critical value.

A8:

If the current stress and the stress up to this increment are both positive, it is possible to take the maximum of these stresses as the damage variable.

A9:

If the current stress is positive and the maximum stress up to this increment is negative, it is necessary to compare the absolute values of the stresses because it is possible when only taking the maximum or minimum of these stresses into consideration, that an element, which has failed earlier might be “repaired” due to the choice of stress as the damage value. Since the maximum compressive stress is higher than the maximum tensile stress, it is necessary to use the factor calculated in A3 in order to define the right value as damage value. As described earlier the factor is the ratio of the maximum tensile stress to the maximum compressive stress is taken. Therefore the positive stress value S is the relevant stress value as long as the negative stress is greater than -48MPa.

Appendix A: Subroutine codes

A10:

This can be seen as the “ELSE”-case to A8. If the negative stress S_{Max} becomes less than -48 MPa, this means that the absolute value becomes greater than 48 MPa, it is stored as damage value.

A11:

Here the damage value is defined if the current stress S is negative and the maximum stress up to the increment S_{Max} is positive. This specification is made for the same reason as described under A8, to prevent the “healing” of elements. Again, the stress ratio is used to define the damage value. The absolute values of the stresses are compared. If the maximum stress is higher than the product of the stress ratio and the current stress, the maximum stress is stored as damage value.

A12:

Again, this is the „ELSE” case of A10. If the maximum stress S_{Max} is less than the current stress S multiplied with the factor, the negative stress is taken into consideration.

A13:

If both the maximum stress up to the increment and the current stress are negative, the smaller value is stored in the damage variable.

A14:

Definition of the damage value for the maximum principal stresses SP_3 (analogous A8-A13)

A15:

Comparison of the maximum shear stress up to this increment to the current shear stress and storage of this value as damage variable.

A16:

All field variables (FV) are set to zero. This indicates that no failure has occurred yet. This is the initial situation.

A17-A19:

Comparison of Damage stress to maximum allowable stress

A17:

The function checks if the maximum stress (Damage) SP_1 up to this point is positive. When this is the case, the normal stresses are compared to the maximum allowable tensile stress of the adhesive and the FV is set to one if this failure criterion is exceeded. If the Damage stresses are negative, they are compared to the maximum allowable compression stress and the corresponding FV is also changed to one.

A18:

Comparison of Damage stress to maximum allowable stress (analogous A17)

A19:

Comparison of Damage stress to maximum allowable shear stress

A20:

The maximum stress (Damage) is stored in the solution dependent state variables. The SDVs are updated only once per increment, more precisely at the end of the increment.

A21:

Output request. Several data for example all stresses, the element number (NOEL) and the number of integration point (NPT) are written out to a txt-file.

A22:

If an error occurs, a warning will be written out into the data file, including the element number and the integration point number where the error occurred.

Appendix A: Subroutine codes

UMAT explicit

Code:

<pre> SUBROUTINE UMAT(STRESS,STATEV,DDSDDE,SSE,SPD,SCD, 1 RPL,DDSDDT,DRPLDE,DRPLDT,STRAN,DSTRAN, 2 TIME,DTIME,TEMP,DTEMP,PREDEF,DPRED,MATERL,NDI,NSHR,NTENS, 3 NSTATV,PROPS,NPROPS,COORDS,DROT,PNEWDT,CELENT, 4 DFGRD0,DFGRD1,NOEL,NPT,KSLAY,KSPT,KSTEP,KINC) C INCLUDE 'ABA_PARAM.INC' CHARACTER*80 MATERL DIMENSION STRESS(NTENS),STATEV(NSTATV), 1 DDSDDT(NTENS,NTENS),DDSDDT(NTENS),DRPLDE(NTENS), 2 STRAN(NTENS),DSTRAN(NTENS),TIME(2),PREDEF(1),DPRED(1), 3 PROPS(NPROPS),COORDS(3),DROT(3,3), 4 DFGRD0(3,3),DFGRD1(3,3) C C DIMENSION EELAS(6),EPLAS(6),FLOW(6) PARAMETER (ZERO=0.0D0,ONE=1.0D0,TWO=2.0D0,THREE=3.0D0,SIX=6.0D0) DATA NEWTON,TOLER/10,1.D-6/ DATA index/0/ SAVE index </pre>	<p>A1</p>
<pre> C Path of the result file, has to be checked before analysis start IF (index.EQ.0) THEN OPEN(100,FILE='C:\Task141\P1.3.6\abaqus\work2\output.txt') WRITE(100,'(8A14)') 'NOEL','KINC','NPT','DTIME', 1 'ratio','SMises', 'SMisesMax','Damage3' index=1 ENDIF C IF (NDI.NE.3) THEN WRITE(6,1) 1 FORMAT(/,30X,'***ERROR - THIS UMAT MAY ONLY BE USED FOR ', 1 'ELEMENTS WITH THREE DIRECT STRESS COMPONENTS') CALL EXIT ENDIF </pre>	<p>A2</p>
<pre> S11= STRESS(1) S13= DABS(STRESS(5)) </pre>	<p>A3</p>
<pre> SMISES=(STRESS(1)-STRESS(2))*(STRESS(1)-STRESS(2)) + 1 (STRESS(2)-STRESS(3))*(STRESS(2)-STRESS(3)) + 1 (STRESS(3)-STRESS(1))*(STRESS(3)-STRESS(1)) DO K1=NDI+1,NTENS SMISES=SMISES+SIX*STRESS(K1)*STRESS(K1) </pre>	<p>A4</p>

Appendix A: Subroutine codes

<pre> END DO SMISES=SQRT(SMISES/TWO) </pre>	
<pre> S11MAX = STATEV(1) S13MAX = STATEV(2) SMisesMax = STATEV(3) </pre>	A5
<pre> SMaxS11=PROPS(7) SMaxS13=PROPS(8) SMaxDruck=PROPS(9) EMOD=PROPS(1) ENU =PROPS(6) </pre>	A6
<pre> IDF1=0 IDF2=0 IDF3=0 Damage1 = MAX(S11 , S11MAX) Damage2 = MAX(S13 , S13MAX) Damage3 = Max(SMises, SMisesMax) ratio=(Damage3/SMaxDruck) </pre>	A7
<pre> C write information out to the output file output.txt IF (ratio.GT.1.0.AND.STATEV(6).EQ.0) THEN WRITE(100,'(8G14.3)') NOEL,KINC,NPT,DTIME,ratio, 1 SMises, SMisesMax,Damage3 ENDIF </pre>	A8
<pre> IF (Damage1 .GE. SMaxS11) IDF1 = 1 IF (Damage2 .GE. SMaxS13) IDF2 = 1 IF ((Damage3/SMaxDruck) .GE. 1.D0) IDF3 = 1 </pre>	A9
<pre> STATEV(1) = Damage1 STATEV(2) = Damage2 STATEV(3) = Damage3 STATEV(4) = IDF1 STATEV(5) = IDF2 STATEV(6) = IDF3 </pre>	A10
<pre> IF(IDF3.EQ.0) THEN IF(IDF2.EQ.0) THEN IF(IDF1.EQ.1) EMOD=PROPS(2) ELSE EMOD=PROPS(3) END IF ELSE EMOD=PROPS(5) IF(IDF1.EQ.0.or.IDF2.EQ.0) EMOD=PROPS(4) END IF </pre>	A11

Appendix A: Subroutine codes

STATEV(7) = EMOD	
<pre> IF(ENU.GT.0.4999.AND.ENU.LT.0.5001) ENU=0.499 EBULK3=EMOD/(ONE-TWO*ENU) EG2=EMOD/(ONE+ENU) EG=EG2/TWO EG3=THREE*EG ELAM=(EBULK3-EG2)/THREE </pre>	A12
<pre> C ELASTIC STIFFNESS C DO K1=1,NTENS DO K2=1,NTENS DDSDE(K2,K1)=0.0 END DO END DO </pre>	A13
<pre> DO K1=1,NDI DO K2=1,NDI DDSDE(K2,K1)=ELAM END DO DDSDE(K1,K1)=EG2+ELAM END DO DO K1=NDI+1,NTENS DDSDE(K1,K1)=EG END DO </pre>	A14
<pre> DO K1=1,NTENS STRESS(K1)=ZERO END DO </pre>	A15
<pre> DO K1=1,NTENS DO K2=1,NTENS STRESS(K2)=STRESS(K2)+ 1 DDSDE(K2,K1)*(STRAN(K1)+DSTRAN(K1)) END DO END DO C RETURN END </pre>	A16

Documentation:

A1:

This is the interface between the subroutine and ABAQUS. The call of this subroutine provides different information for the analysis such as analysis time, step time and increment number. The declaration of variables is also part of this part.

A2:

Appendix A: Subroutine codes

Output requests. The path of the result file has to be checked before the analysis starts. When the index is zero, there are several values as the element number and the stress ratio that are written into the output file. If elements are used that do not have got exactly three direct stress components, an error warning is written and the analysis is stopped.

A3:

Get the stresses of the last increment. The form of the stress array is the same as in the USDFLD.

A4:

Calculation of the Von Mises stress from the normal and shear stress components. The stresses are taken from the last increment.

A5:

Call for the SDVs that store the maximum stresses of the material point up to this increment.

A6:

Here the maximum allowable stresses (“SMAXS”) and some material data (“EMOD”, “ENU”) are defined. For this purpose, the PROPS array is used.

A7:

The failure identifiers (IDFs) are set to zero. This is the normal position as long as no failure occurs. Afterward the current stresses of the increment (“S”) are compared to the maximum stresses up to this increment (“SMAX”) and assigned to the Damage1/2/3 variables.

A8:

Output request if the defined ratio of the maximum Von Mises stress (“Damage”) and the maximum allowable compression stress (“SMAXDruck”) is greater than one or the current Von Mises stress is greater than SMAXDruck.

A9:

The maximum allowable stresses (“SMAXS”) are compared to the maximum stresses up to this increment (“Damage”). If the criterion is exceeded the failure identifiers are set to one.

A10:

The maximum stresses up to this increment are stored in the SDVs STATEV 1-3 while the failure identifiers are saved in the SDVs STATEV 6.

A11:

Here is checked which of the failure criteria are exceeded and the Young’s modulus is set to the corresponding value stored in the PROPS array.

A12:

In this section the new Young’s modulus is used to calculate a variety of Young’s moduli in order to calculate the new Jacobian matrix. The Young’s moduli derived only simplify the calculation of the matrix.

A13:

All elements of the Jacobian matrix are set to zero.

A14:

Here the Jacobian matrix is filled with the different Young’s moduli that apply to the different elements of the matrix. The first part fills all elements of the 3×3 matrix on the upper left hand side with the value “ELAM”. Afterwards the diagonal of the same matrix is set to “EG2+ELAM” and finally the diagonal of the lower right hand 3×3 matrix is set to the shear modulus “EG”. In this subroutine K1 stands for the number of columns and K2 stands for the number of rows.

A15:

The stress array is set to zero. This is important so that the entire stress at the end of the increment will be calculated.

A16:

Appendix A: Subroutine codes

In this section the stresses are calculated with an elastic material behavior. The Jacobian matrix $DDSDDE(K2,K1)$ was calculated in A14 and the total strain is given by ABAQUS. Therefore it is possible to calculate the stresses with the equation $\sigma_j = D_{ij} * (\varepsilon_i + \Delta\varepsilon_i)$ where

σ_j is STRESS(K2),

D_{ij} is DDSDDDE(K2,K1),

ε_i is replaced by the array STRAN(K1) in which the total strains at the beginning of the increment are stored

$\Delta\varepsilon_i$ is the array of strain increments.

UMAT implicit

<pre> SUBROUTINE UMAT(STRESS,STATEV,DDSDDE,SSE,SPD,SCD, 1 RPL,DDSDDT,DRPLDE,DRPLDT,STRAN,DSTRAN, 2 TIME,DTIME,TEMP,DTEMP,PRED,DPRED,MATERL,NDI,NSHR,NTENS, 3 NSTATV,PROPS,NPROPS,COORDS,DROT,PNEWDT,CELENT, 4 DFGRD0,DFGRD1,NOEL,NPT,KSLAY,KSPT,KSTEP,KINC) C INCLUDE 'ABA_PARAM.INC' C CHARACTER*80 MATERL DIMENSION STRESS(NTENS),STATEV(NSTATV), 1 DDSDDE(NTENS,NTENS),DDSDDT(NTENS),DRPLDE(NTENS), 2 STRAN(NTENS),DSTRAN(NTENS),TIME(2),PRED(1),DPRED(1), 3 PROPS(NPROPS),COORDS(3),DROT(3,3), 4 DFGRD0(3,3),DFGRD1(3,3) C DIMENSION EELAS(6),EPLAS(6),FLOW(6) PARAMETER (ZERO=0.0D0,ONE=1.0D0,TWO=2.0D0,THREE=3.0D0,SIX=6.0D0) C COMMON/COUNT/idummy1, idummy2, kiter C save ifirst, ifelem, icall, ifail, iiter, incold save index, irestart, itype DATA index/0/, ifail/0/, itype/0/ </pre>	A1
<pre> C Path of the result file, has to be checked before analysis start c if this is the first ever call to the routine then first C element:ifelem C set flag saying first call has been made IF (index.EQ.0) THEN OPEN(100,FILE='C:\Task141\P1.3.6\abaqus\work2\output_1%.txt') WRITE(100,'(8A14)') 'NOEL','KINC','NPT','DTIME', 1 'ratio','SMises','SMisesMax','Damage3' IF (NDI.NE.3) THEN WRITE(6,1) 1 FORMAT(//,30X,'***ERROR - THIS UMAT MAY ONLY BE USED FOR ', 1 'ELEMENTS WITH THREE DIRECT STRESS COMPONENTS') CALL XIT ENDIF </pre>	A2

Appendix A: Subroutine codes

<pre> write(100,*)'First ever call to UMAT' ifelem = NOEL ifirst = 1 icall = 2 incold = 100 irestart = 0 istart = 0 write(100,*)'Starting at first element = ', NOEL index=1 ENDIF </pre>	
<pre> istart = 1 failmax = 1.1 </pre>	A3
<pre> c Identify first or second call at new increment start by flag ICALL c ICALL is 1 for first call and 2 for second call and subsequent C iterations c check for ifail value in case increment is restarted c (same increment number, but ifail larger 2) c Iteration number needs to be increased during UMAT calls but not C during the c first two calls IF (IFELEM.EQ.NOEL.AND.NPT.EQ.1.AND.ICALL.EQ.2.AND. 1 KINC.NE.INCOLD.AND.KINC.NE.0) THEN C ICALL = 1 IFAIL = 0 IITER = 1 </pre>	A4
<pre> ELSE IF (IFELEM.EQ.NOEL.AND.NPT.EQ.1.AND.ICALL.EQ.2.AND. 1 KINC.EQ.INCOLD.AND.KINC.NE.0.AND.IFAIL.GE.2) THEN C WRITE(100,*) 'Increment is restarted - 2 elements failed' ICALL = 1 IFAIL = 0 IITER = 1 IRESTART = 0 INCOLD = KINC - 1 </pre>	A5
<pre> ELSE IF (IFELEM.EQ.NOEL.AND.NPT.EQ.1.AND.ICALL.EQ.2.AND. 1 KINC.EQ.INCOLD.AND.KINC.NE.0.AND.IRESTART.EQ.1) THEN C WRITE(100,*) 'Increment is restarted - failmax exceeded' ICALL = 1 IFAIL = 0 IITER = 1 </pre>	A6

Appendix A: Subroutine codes

<pre>IRESTART = 0 INCOLD = KINC - 1</pre>	
<pre>ELSE IF (IFELEM.EQ.NOEL.AND.NPT.EQ.1.AND.ICALL.EQ.1.AND. 1 KINC.NE.INCOLD.AND.KINC.NE.0) THEN C ICALL = 2 INCOLD = KINC</pre>	A7
<pre>ELSE IF (IFELEM.EQ.NOEL.AND.NPT.EQ.1.AND.ICALL.EQ.2.AND. 1 KINC.EQ.INCOLD.AND.KINC.NE.0) THEN C IITER = IITER + 1 C END IF</pre>	A8
<pre>c Message file output IF (NOEL.eq.ifelem.and.NPT.eq.1) THEN write(100,*)'New loop call to UMAT-----' write(100,*)'Increment number ',KINC write(100,*)'Iteration number ',IITER IF (icall.eq.2.and.IITER.eq.1) THEN write(100,*)'Second UMAT call in new increment!' write(100,*)'Check for PNEWDT' END IF END IF</pre>	A9
<pre>EMOD=PROPS(1) IF(KSTEP.NE.1.or.KINC.NE.1) EMOD=STATEV(7) ENU =PROPS(6) IF(ENU.GT.0.4999.AND.ENU.LT.0.5001) ENU=0.499 EBULK3=EMOD/(ONE-TWO*ENU) EG2=EMOD/(ONE+ENU) EG=EG2/TWO EG3=THREE*EG ELAM=(EBULK3-EG2)/THREE</pre>	A10
<pre>C ELASTIC STIFFNESS C DO K1=1,NTENS DO K2=1,NTENS DDSDE(K2,K1)=0.0 END DO END DO</pre>	A11
<pre>DO K1=1,NDI</pre>	A12

Appendix A: Subroutine codes

<pre> DO K2=1,NDI DDSDE(K2,K1)=ELAM END DO DDSDE(K1,K1)=EG2+ELAM END DO DO K1=NDI+1,NTENS DDSDE(K1,K1)=EG END DO </pre>	
<pre> DO K1=1,NTENS STRESS(K1)=ZERO END DO </pre>	A13
<pre> DO K1=1,NTENS DO K2=1,NTENS STRESS(K2)=STRESS(K2) + 1 DDSDE(K2,K1)*(STRAN(K1)+DSTRAN(K1)) END DO END DO </pre>	A14
<pre> C Starting evaluation of failure criteria C (does not have to be done for first call) IF (ICALL.EQ.2) THEN C S11= STRESS(1) S13= DABS(STRESS(5)) </pre>	A15
<pre> SMISES=(STRESS(1)-STRESS(2))*(STRESS(1)-STRESS(2)) + 1 (STRESS(2)-STRESS(3))*(STRESS(2)-STRESS(3)) + 1 (STRESS(3)-STRESS(1))*(STRESS(3)-STRESS(1)) DO K1=NDI+1,NTENS SMISES=SMISES+SIX*STRESS(K1)*STRESS(K1) END DO SMISES=SQRT(SMISES/TWO) </pre>	A16
<pre> S11MAX = STATEV(1) S13MAX = STATEV(2) SMisesMax = STATEV(3) </pre>	A17
<pre> SMaxS11=PROPS(7) SMaxS13=PROPS(8) SMaxDruck=PROPS(9) </pre>	A18
<pre> IDF1=0 IDF2=0 </pre>	A19

Appendix A: Subroutine codes

<pre>IDF3=0 Damage1 = MAX(S11 , S11MAX) Damage2 = MAX(S13 , S13MAX) Damage3 = Max(SMises, SMisesMax) ratio=(Damage3/SMaxDruck)</pre>	
<pre>C write information out to the output file output.txt IF (ratio.gt.1.0.AND.STATEV(6).EQ.0) THEN WRITE(100,'(8G14.3)') NOEL,KINC,NPT,DTIME,ratio, 1 SMises, SMisesMax,Damage3 ENDIF</pre>	A20
<pre>C reduce the increment size if failmax exceeded IF ((ratio).GT.failmax.AND.STATEV(6).EQ.0.AND.IITER.EQ.1) THEN PNEWDT=0.85 IRESTART = 1 ENDIF</pre>	A21
<pre>C reduce the increment size if more than one element is failing in first C iteration c istart = 1 we count element failure c istart = 0 element failure not considered IF (istart.eq.1) THEN IF (ratio.GE.1.0.AND.STATEV(6).EQ.0.AND.IITER.EQ.1) THEN C c Restart criterion IF (IFAIL.EQ.0) THEN C ifail = 1 NELFAIL = NOEL GO TO 200 C END IF C IF (NOEL.NE.NELFAIL) THEN C ifail = ifail + 1 NELFAIL = NOEL C ELSE C write(100,*)'Failure in same element' C END IF C IF (IFAIL.GE.2) THEN write(100,*)'Restart - at least two failures' PNEWDT = 0.85 END IF</pre>	A22

Appendix A: Subroutine codes

<pre>C END IF END IF 200 CONTINUE</pre>	
<pre>IF (Damage1 .GE. SMaxS11) IDF1 = 1 IF (Damage2 .GE. SMaxS13) IDF2 = 1 IF ((Damage3/SMaxDruck) .GE. 1.D0) IDF3 = 1</pre>	A23
<pre>STATEV(1) = Damage1 STATEV(2) = Damage2 STATEV(3) = Damage3 STATEV(4) = IDF1 STATEV(5) = IDF2 STATEV(6) = IDF3</pre>	A24
<pre>IF(IDF3.EQ.0) THEN IF(IDF2.EQ.0) THEN IF(IDF1.EQ.1) EMOD=PROPS(2) ELSE EMOD=PROPS(3) END IF ELSE EMOD=PROPS(5) IF(IDF1.EQ.0.or.IDF2.EQ.0) EMOD=PROPS(4) END IF STATEV(7) = EMOD</pre>	A25
<pre>EBULK3=EMOD/(ONE-TWO*ENU) EG2=EMOD/(ONE+ENU) EG=EG2/TWO EG3=THREE*EG ELAM=(EBULK3-EG2)/THREE</pre>	A26
<pre>C NEW ELASTIC STIFFNESS C DO K1=1,NTENS DO K2=1,NTENS DDSDE(K2,K1)=0.0 END DO END DO</pre>	A27
<pre>DO K1=1,NDI DO K2=1,NDI DDSDE(K2,K1)=ELAM END DO</pre>	A28

Appendix A: Subroutine codes

<pre> DDSDDE(K1,K1)=EG2+ELAM END DO DO K1=NDI+1,NTENS DDSDDE(K1,K1)=EG END DO </pre>	
<pre> DO K1=1,NTENS STRESS(K1)=ZERO END DO </pre>	A29
<pre> DO K1=1,NTENS DO K2=1,NTENS STRESS(K2)=STRESS(K2)+ 1 DDSDDE(K2,K1)*(STRAN(K1)+DSTRAN(K1)) END DO END DO C END IF C RETURN END </pre>	A30

Appendix B: Input files

Design 1 (for use with UMAT implicit advanced):

```

*HEADING
ABAQUS job created on 18-Mar-05 at 14:23:59
**
*NODE
    1,    1000.,    0.,    780.
    2,    999.967,    8.07206,    780.
...
**
*MPC
    BEAM,    9954,    6635
    BEAM,    9953,    1
...
**
*ELEMENT, TYPE=S4R , ELSET=ALL_SKIN
    1,    1,    2,    7,    6
    2,    2,    3,    8,    7
...

*ELEMENT, TYPE=C3D8, ELSET=ADHESIVE
    6397,    9165,    9166,    9168,    9167,    9175,    9176,
    9178,    9177
...
**
** skin
**
*NSET, NSET=SKIN, GENERATE
    1,    395,    1
    397,    404,    1
...
**
** skin
**
*ELSET, ELSET=SKIN, GENERATE
    1,    4056,    1
**
** stringer_web
**
*NSET, NSET=STRINGER_WEB, GENERATE
    4820,    6004,    1
**
** stringer_web
**
*ELSET, ELSET=STRINGER_WEB, GENERATE
    4057,    4836,    1

```

Appendix B: Input files

```
**
** stringer_flange
**
*NSET, NSET=STRINGER_FLANGE
  4820, 4823, 4826, 4829, 4832, 4835, 4838, 4841,
  4844, 4847, 4850, 4853, 4856, 4859, 4862, 4865,
...
**
** stringer_flange
**
*ELSET, ELSET=STRINGER_FLANGE, GENERATE
  4837, 6396, 1
**
** ADHESIVE
**
*NSET, NSET=ADHESIVE, GENERATE
  9165, 13114, 1
**
** ADHESIVE
**
*ELSET, ELSET=ADHESIVE, GENERATE
  6397, 7956, 1
**
**
** clamp
**
*NSET, NSET=CLAMP, GENERATE
  391, 395, 1
  1099, 1106, 1
...
**
** load_edge
**
*NSET, NSET=LOAD_EDGE, GENERATE
  1, 5, 1
  397, 404, 1
...
**
** potting
**
*NSET, NSET=POTTING, GENERATE
  6, 35, 1
  361, 390, 1
...
**
** global
**
```

Appendix B: Input files

```

*NODE, NSET=GLOBAL
 100000, 961.055, 276.359, 780.
**
*****ORIENTATIONS*****
**
** SKIN + STRINGER_FLANGE (ANGLE 90 TURNED)
**
*ORIENTATION, SYSTEM=C, NAME=plus45
0, 0, 0, 0, 0, 1
1, -45.
*ORIENTATION, SYSTEM=C, NAME=minus45
0, 0, 0, 0, 0, 1
1, 45.
*ORIENTATION, SYSTEM=C, NAME=null
0, 0, 0, 0, 0, 1
1, 90.
*ORIENTATION, SYSTEM=C, NAME=h_90
0, 0, 0, 0, 0, 1
1, 0.
**
** STRINGER_WEB (ANGLE ok)
**
*ORIENTATION, SYSTEM=C, NAME=strplus45
0, 0, 0, 0, 0, 1
2, 45.
*ORIENTATION, SYSTEM=C, NAME=strminus45
0, 0, 0, 0, 0, 1
2, -45.
*ORIENTATION, SYSTEM=C, NAME=strnull
0, 0, 0, 0, 0, 1
2, 0.
**
*****Properties*****
**
***[N/mm2]
*MATERIAL, NAME=cfrp
*ELASTIC, TYPE=lamina
147.0E3, 11.8E3, 0.34, 6.0E3, 6.0E3, 4.0E3
**
**FAIL STRESS
**2.715E3, -1.4E3, 0.056E3, -0.25E3, 0.101E3, 0,
**
**
*material, name=MAT_ADHESIVE
*User material, Constants=9
3.0E3, 3.0E3, 3.0E3, 30.00, 30.00 , 0.4 ,8.00 ,38.00,
48.00
*DEPVAR
7,
**
**

```


Appendix B: Input files

```

0.125, 3, cfrp, null
0.125, 3, cfrp, null
**
*** ADHESIVE
*SOLID SECTION, ELSET=ADHESIVE, MATERIAL=MAT_ADHESIVE
**
*****constraints*****
**
*BOUNDARY
**
CLAMP          , 1, 6
**
POTTING        , 1, 2
POTTING        , 4, 6
**
GLOBAL         , 1, 2
GLOBAL         , 4, 6
**
**
*RIGID BODY, REF NODE=GLOBAL, TIE NSET=LOAD_EDGE
**
**
*STEP, NLGEOM, INC=2000
*STATIC, STABILIZE=4E-6
0.0025, 1.0,1E-7 , 0.005
**
*CONTROLS, PARAMETERS=TIME INCREMENTATION
70, 70, 70, 70, 10, 4, 25, 25, 6
**
*****Load*****
**
**displacement controlled
**
*BOUNDARY
GLOBAL, 3, 3, -4.0
**
*****odb output*****
**
*EL PRINT, FREQ=0
**
*EL FILE, FREQ=0
**
*NODE FILE, FREQ=0
**
** ODB Output: FIELD
**
*OUTPUT, FIELD, FREQ=2
**
*ELEMENT OUTPUT, ELSET=SKIN
1, 2, 5, 8, 11, 14, 17, 20, 23, 24
S, CFAILURE

```

Appendix B: Input files

```
**  
*ELEMENT OUTPUT, ELSET=STRINGER_FLANGE  
1, 2, 5, 8, 11, 14, 17, 20, 21  
S, CFAILURE  
**  
*ELEMENT OUTPUT, ELSET=STRINGER_WEB  
1, 2, 5, 8, 11, 14, 17, 20, 23, 26, 29, 32, 35, 38, 39  
S, CFAILURE  
**  
*ELEMENT OUTPUT, ELSET=ADHESIVE  
S, SDV  
**  
*NODE OUTPUT  
U, RF  
**  
** ODB Output: HISTORY  
**  
*OUTPUT, HISTORY, FREQ=2  
**  
*NODE OUTPUT, NSET=GLOBAL  
U, RF  
**  
*ENERGY OUTPUT, VAR=ALL  
**  
*MONITOR, NODE=100000, DOF=3  
**  
*RESTART, WRITE, OVERLAY  
**  
*END STEP
```

Erklärung

Ich versichere hiermit, dass ich die vorliegende Arbeit selbständig verfasst und keine anderen als die im Literaturverzeichnis angegebenen Quellen benutzt habe.

Stellen, die wörtlich oder sinngemäß aus veröffentlichten oder noch nicht veröffentlichten Quellen entnommen sind, sind als solche kenntlich gemacht.

Die Zeichnungen oder Abbildungen in dieser Arbeit sind von mir selbst erstellt worden oder mit einem entsprechenden Quellennachweis versehen.

Diese Arbeit ist in gleicher oder ähnlicher Form noch bei keiner anderen Prüfungsbehörde eingereicht worden.

Aachen, im März 2006

Geheimhaltung

Diese Diplomarbeit darf weder vollständig noch auszugsweise ohne schriftliche Zustimmung des Autors, des betreuenden Referenten bzw. des Deutschen Zentrums für Luft- und Raumfahrt (DLR) vervielfältigt, veröffentlicht oder Dritten zugänglich gemacht werden.

Declaration

I declare that this dissertation comprises only my own work compiled without the assistance of others and with the use only of the acknowledged sources and aids. Due acknowledgment has been made to all other material used.

.....
Date

.....
Signature